AN INVESTIGATION INTO THE FLOW IN CANDU FAN NOZZLES

AN INVESTIGATION INTO THE FLOW IN CANDU FAN NOZZLES

By TRAVIS SHEASGREEN, B.Sc.E

A Thesis

Submitted to the School of Graduate Studies

In partial Fulfillment of the Requirements for the Degree

Master of Applied Science

McMaster University

© Travis Sheasgreen, September 2017

MASTER OF APPLIED SCIENCE (2017)   MCMASTER UNIVERSITY

(Engineering Physics)   Hamilton, Ontario, Canada

Title: An Investigation Into The Flow In Candu Fan Nozzles

Author: Travis Michael James Sheasgreen, BScE (UNB)

Supervisor: Dr. D.R. Novog

Number of Pages: xx, 146

Lay Abstract

In order to create accurate simulations moderator flow in a calandria vessel, simulations of smaller components must first be verified. The moderator inlet fan nozzle found in the Pickering CANDU calandria vessel has complicated geometry which can be difficult to model using CFD. Simulations were performed on a scaled down version of the nozzle and physical experiments were performed on a constructed model.

The results found that the simulations predicted similar velocity distributions, but generally with higher peak velocity values than the physical experiments. However additional measurement locations would be needed to give a more comprehensive comparison. Going forward with the larger simulations, to better determine the best model to use for the nozzle, a larger version should be used with different turbulence models and measurement locations.

Abstract

The moderator within the CANDU calandria vessel is an important element of the reactor serving various operational and safety functions. A validated computational fluid dynamics model to simulate the fluid within the calandria vessel is required to predict how it would behave in different situations. Given is high level of complexity (flow from complicated inlets inlet, outlet, volumetric heating, flows around fuel channels, etc…) validation typically proceeds from separate effect studies for each component as well as integral validation where all complex phenomena are included. This work is focused on the separate effect studies aimed at phenomena relevant to the inlets of Pickering A.

A scaled down model of the Pickering CANDU moderator inlet nozzle was constructed and used to verify simulations done on the same nozzle. Physical measurements were taken using a PIV laser system on the scaled down nozzle. Seven measurements planes were taken on two of the outlets of the nozzle at two different flowrates (0.2 kg/s and 0.1 kg/s). Given a single PIV measurement plane contains approximately 1000 velocity points this represents approximately 28000 new velocity measurements for CFD validation. A CAD model of the nozzle was imported into STAR-CCM+ CFD software to perform the simulations. The simulations used the k-ω SST turbulence model and were performed using the same

iv

flowrates as in the experiments. The k-ε model was also used as a comparison for the k-ω SST model. The same locations were used in calculations for the seven measurement planes so that the same areas could be compared for the models employed.

The CFD results were found to agree qualitatively with the measured ones but no quantitative comparisons should be made with care. Additional investigation is required for a more comprehensive comparison. While both, measured and calculated results, showed similar velocity distributions, the velocities values differed by varying degrees. In particular, the simulations did not show the same jet expansion as the physical measurements indicated. There is not enough data from the measurement planes to determine if the flow in the physical experiments are more diffuse and the velocity field gradients are lower than obtained in the current study. With large portions of the nozzle unobserved by the measurement planes, it cannot be concluded that there are no other peaks or large velocity gradient regions in between the planes. For future work it would be beneficial to have a larger model of the nozzle for better gradient resolution, as well as using a measuring system that allows for more precise data collection. Different turbulence models and measurements further away from the nozzle should also be used to determine which would be best in a larger simulation.

Acknowledgements

First and foremost, I would like to thank my supervisor Dr. David Novog for the support, guidance and great amount of patience he has provided. This would not be possible without him. I would also like to thank Dr. Alex Rashkovan who has given much of his time in helping me.

Thanks to James Strack, David Joyal, Garik Patterson, Kendall Boniface and Chris Hollingshead, who have helped me on numerous occasions with the experiment and simulations. Finally, I would like to thank all of my friends and family who have supported me along the way.

Contents

List of Figures

List of Tables

List of Symbols

a	Superellipse main axis
b	Superellipse minor axis
C_1	Dimensionless constant
C_2	Dimensionless constant
C_{ij}	Transport of Reynolds stress by convection
C_{b2}	Dimensionless constant used with Spalart-Allmaras equation
C_{b1}	Dimensionless constant used with Spalart-Allmaras equation
C_{w1}	Dimensionless constant used with Spalart-Allmaras equation
$C_{1\varepsilon}$	Dimensionless constant in k-ε equations
$C_{2\varepsilon}$	Dimensionless constant in k-ε equations
C_μ	Dimensionless constant
CFD	Computational fluid dynamics
D_{ij}	Transport of Reynolds stress by diffusion
e_{ikm}	Alternating symbol
e_{jkm}	Alternating symbol
f_w	Wall damping function
k	Turbulent Kinetic Energy
LDV	Laser dopler velocimetry

P	Pressure
P_{ij}	Production of Reynolds stress
P_k	Rate of production of turbulent kinetic energy
PIV	Particle image velocimetry
R_{ij}	Reynolds stress
R_{im}	Reynolds stress
R_{jm}	Reynolds stress
r	Superellipse curve
S_{ij}	Mean rate of deformation
t	Time
U	Mean velocity in x direction
U	Total mean velocity
u	Velocity in x direction
u'	Fluctuating velocity in x direction
U_i	Total mean velocity in specified direction
U_j	Total mean velocity in specified direction
U_k	Total mean velocity in specified direction
u'_i	Fluctuating velocity in specified direction
u'_j	Fluctuating velocity in specified direction
u'_m	Fluctuating velocity in specified direction
V	Mean velocity in y direction
v	Velocity in y direction

v'	Fluctuating velocity in y direction
W	Mean velocity in z direction
w	Velocity in z direction
w'	Fluctuating velocity in z direction
x_j	Distance in specified direction
x_m	Distance in specified direction
β^*	Dimensionless constant
β_1	Dimensionless constant in k-ω equations
β_2	Dimensionless constant in SST equations
γ_1	Dimensionless constant in k-ω equations
γ_2	Dimensionless constant in SST equations
δ_{ij}	Kronecker delta
ε	Turbulence dissipation
ε_{ij}	Dissipation rate of Reynolds stress
μ	Viscosity
μ_t	Eddy viscosity
π_{ij}	Transport of Reynolds stress by pressure-strain
ρ	Density
σ_k	Dimensionless constant
σ_ε	Dimensionless constant in k-ε equations
σ_ω	Dimensionless constant in k-ω equations
$\sigma_{\omega,1}$	Dimensionless constant in SST equations

$\sigma_{\omega,2}$	Dimensionless constant in SST equations
$\hat{v}$	Viscosity parameter
σ_v	Dimensionless constant used with Spalart-Allmaras equation
v	Kinematic viscosity
v_t	Constant in Reynolds stress equations
κ_y	Length scale
Ω	Mean vorticity
$\hat{\Omega}$	Local mean vorticity
Ω_{ij}	Transport of Reynolds stress by rotation
ω	Turbulence frequency
ω_k	Rotation vector

Declaration of Academics Achievement

I, Travis Sheasgreen, declare this thesis to be my own work. I am the sole author of this document. No part of this work has been published or submitted for publication or for a higher degree at another institution.

To the best of my knowledge, the content of this document does not infringe on anyone's copyright.

My supervisor, Dr. Novog, and Dr. Rashkovan have provided guidance and support at all stages of this project. I completed all of the research work.

1. INTRODUCTION

1.1. Moderator flow in CANDU reactors

The CANDU is a Canadian designed pressurized heavy water reactor (PHWR). A typical nuclear reactor works by creating a sustained nuclear fission reaction of Uranium 235. A fission reaction occurs when following neutron absorption, an atom's nucleus is too energetic and splits into two smaller elements and free neutrons (Lamarsh, 1975). The reaction is sustained by using the neutrons released during fission to induce fission other nuclei at a controlled rate. When the neutrons are first released by the fission reaction they are very energetic and will have a small absorption cross section in the fissile material. The moderator in a reactor is used to reduce the energy of neutrons in the reactor by colliding with the moderator molecules. Every neutron collision reduces the energy of the neutrons so that they become less energetic and more likely to be absorbed by the Uranium 235 and induce fission. The CANDU type reactor uses heavy water as a coolant and a moderator, instead of light water as it is less absorbent of neutrons. The high neutron economy (low absorbing coolant and moderator, lattice pitch etc…) gives the CANDU the unique ability to use natural Uranium fuels. Given the low excess reactivity in the CANDU core which results from natural Uranium fuel, CANDUs utilize on power refueling wherein approximately 0.1% of the fuel is replaced daily.

Approximately 20 fuel pellets (Uranium oxide, UO_2) are placed in sheaths to form a fuel element. The elements are connected in concentric rings to form fuel bundles that are approximately 50cm in length and 12 fuel bundles are placed inside the horizontal pressure tubes. The pressure tubes are thermally isolated from the calandria tubes using CO_2 filling the gap between the two. While the fission reaction is taking place in the core, thermal energy is transferred from the fuel rods to the coolant flowing through the pressure tubes. Not all the heat is convected by the coolant, some portion is transported to the low pressure low temperature moderator fluid via gamma rays and neutrons. During the neutron interactions with the heavy water molecules, as the neutrons collide with the deuterium via inelastic collision the heavy water will heat up as energy is transferred to the water molecules. Gamma rays emitted by the nuclear reactions occurring in the core are also partly absorbed by the heavy water and contribute to moderator volumetric heat up. The vast majority of the heat transferred to the moderator is through the neutron and gamma ray interactions since conduction from the pressure tube to calandria tube is limited by the annulus CO2 gas. Since the energy deposited in the moderator via radiation is significant, the moderator fluid is circulated in its own low pressure circulation loop. This loop consists of heat exchangers, pumps and an inventory control system to ensure the moderator fluid remains below its design temperature. Each CANDU station uses a set of inlet moderator nozzles to pass the fluid back to the calandria and the design and layout of these nozzles is selected to ensure adequate circulation and cooling within the large calandria vessel. In the

Pickering design the moderator inlet nozzles are a fan based design where approximately 60% of the flow enters the calandria vessel. There are a total of 12 fan-nozzles with 6 on each side of the vessel. The remainder of the flow enters from a large number of spray nozzles located in the top of the calandria and these sprays being unique to Pickering A.

1.2. Calandria flow pattern during LOCA

Under normal operating conditions the moderator fluid is heated volumetrically by the incident neutron and gamma radiation. Under some accident scenarios the mode of heat transfer may change and the heat may be rejected from the calandria tube via conduction as described below. The heat transfer efficiency from the calandria tubes to the moderator in this circumstance is controlled by the flow pattern and the temperature of the heavy water inside the calandria vessel. As the nominal heat fluxes to be rejected from the calandria tubes are low, high moderator flow velocities are not required. As a consequence the flow field in a calandria vessel involves a mixture of inertia and buoyancy driven flows.

In the course of an accident, such as a Loss Of Coolant Accident (LOCA) with a failure of Emergency Core Cooling (ECC), after reactor trip fuel cooling is impaired and the residual heat is transferred directly to the pressure tube mostly by conduction and radiation instead of being convected to the coolant. This will result in larger than nominal pressure tube temperatures. As a result of this heat up the pressure tubes undergo plastic deformation and can balloon or sag and come into

contact with the calandria tube. This creates a conduction pathway for the stored energy in the fuel and pressure tube to flow to the low temperature moderator which is in contact with the calandria tube. Provided the moderator fluid remains in contact with the calandria (i.e., there is sufficient moderator inventory to cover the calandria tubes and the extent of Post Dryout conditions on the calandria tubes is limited). The flow field in calandria vessel is controlled by the superposition of the forced flow originating from the fan nozzles and sprays, and the free convection flow resulting from the density variation throughout the moderator. Depending on the relative magnitude of the forced and natural convection, the flow regime inside the vessel can vary from being fully forced circulation through mixed to natural convection - see Kim et al (2006). To a large extent the integrity of the fuel channels will depend on the Critical Heat Flux (CHF) on the calandria outer wall which is in turn dependent on the local subcooling in the moderator. Safety analysis of post-LOCA conditions therefore aims to predict the evolution of the moderator temperature field in order to ensure that the fuel channel assembly remains intact. A key element of these predictions is the validation of the computer codes applied to moderator circulation phenomena.

A number experiments have been performed in scaled down facilities examining the flow and temperature fields inside a calandria type vessel. Koroyannakis et al (1983) experimentally investigated the flow phenomena generated by the inlet jet and internal heating of a fluid in a calandria-like cylindrical vessel of SPEL (Sheridan Park Engineering Laboratory). These experimental results demonstrated

the relationship between the moderator circulation pattern and the inlet flow rate and heat load. Huget et al (1989, 1990) conducted 2-dimensional moderator circulation tests at a 1/4-scaled facility. From these studies, three clearly distinct flow patterns were observed according to certain operating ranges which loosely corresponded to inertially driven conditions, a buoyancy dominated regime and a mixed regime. Khartabil et al (2000) conducted three-dimensional moderator circulation tests in the Moderator Test Facility (MTF) in the Chalk River Laboratories of Atomic Energy of Canada Limited (AECL). MTF is a 1/4 scale of CANDU calandria, with 480 heaters that simulate 480 fuel channels. MTF is designed to study moderator circulation at scaled conditions that are representative of CANDU reactors. The real time data recording at various locations inside the MTF tank have shown some level of fluctuations in the moderator.   The experimental data provided from the MTF tests has formed an integral part of the validation basis for CFD codes used in the nuclear industry for moderator temperature predictions.

To predict the local temperature in the calandria, KAERI started experimental research on moderator circulation as one of a national R&D research programs from 2012. This research program includes the construction of the Moderator Circulation Test (MCT) facility (Kim et al 2013a).

Validation data is planned to be obtained for self-reliant CFD tools, and

development of an optical measurement system using Particle Image Velocimetry (PIV) (Wereley et al 2000) and Laser Induced Fluorescence (LIF) techniques. Small-scale 1/40 (Kim et al 2013c) and 1/8 (Kim et al 2013b) small-scale model tests were performed prior to installation of the main MCT facility to identify the potential problems of the flow visualization and measurement expected in the 1/4 scale MCT facility. It has to be noted that no PIV measurements are reported for non-isothermal case where the rods are electrically heated.

In addition to the scaled experiments, several tests have been done for in-reactor conditions. Austman et al (1985) measured the moderator temperature by inserting thermocouples through a shut-off rod (SOR) guide tube in operating CANDU reactors. Sion, (1983) measured the temperature profile of the D2O moderator inside a CANDU reactor, within the calandria vessel, by means of a specially instrumented probe introduced within the core. Measurements were made under steady and transient reactor conditions using two different sensors, resistance temperature detectors (RTDs) and thermocouples. The results established the feasibility of in-core moderator temperature measurement and indicated that the thermocouples used were relatively not affected by the intense radiation.

Given the importance of CFD analysis to safety predictions in the CANDU moderator, a large amount of effort has been put into validating these tools for the conditions and phenomena relevant in a CANDU reactor. Hohne et al (2009) studied the influence of density differences on the mixing of a pressurized water

reactor. They presented matrix experiments in which water with the same or higher density was injected into a cold tank leg of the reactor with already established natural circulation conditions at different low mass flow rates. Sensors measuring the concentration of a tracer in the injected water were installed in the tank. A transition matrix from momentum to buoyancy-driven flow experiments was selected for validation of the computational fluid dynamics software ANSYS CFX. The results of the experiments and of the numerical calculations show that mixing strongly depends on buoyancy effects: At higher mass flow rates the injected slug propagates in the circumferential direction around the core barrel. Buoyancy effects reduce this circumferential propagation with lower mass flow rates and/or higher density differences.

Yoon et al. (2004) used a computational fluid dynamics model for predicting moderator circulation inside the CANDU reactor vessel. It was to estimate the local sub-cooling of the moderator in the vicinity of the calandria tubes. The buoyancy effect induced by the internal heating was accounted for by the Boussinesq approximation. The standard k–ε turbulence model with logarithmic wall treatment was applied to predict the turbulent jet flows from the inlet nozzles. The matrix of the calandria tubes in the core region was simplified to a porous media. The governing equations were solved by CFX 4. They did a parametric analysis and since their simulation was steady state, it was a base for future transient simulations. In their next paper, Yoon and Park (2008) developed another computational fluid dynamics model by using a coupled solver. They did the simulation for Wolsong

Units 2/3/4. A steady-state moderator circulation under operating conditions and the local moderator sub-cooling were evaluated using the CFD tool. When compared to the former study in the Final Safety Analysis Reports, the current analysis provided well-matched trends and reasonable results. This new CFD model based on a coupled solver shows a dramatic increase in the computing speed, when compared to that based on a segregated solver. In addition, there have been several CFD models for predicting the thermal hydraulics of the CANDU moderator. Yoon et al. (2006) used the CFX-4 code (ANSYS Inc.) to develop a CFD model with a porous media approach for the core region in order to predict the CANDU moderator sub-cooling under normal operating conditions, while Yu et al. (2005) used the FLUENT code to model all the calandria tubes as heating pipes without any approximation for the core region. The analytic model based on CFX-4 has strength in the modeling of hydraulic resistances in the core region and in the treatment of a heat source term in the energy equations, but it faces convergence issues and a slow computing speed. It occurs because CFX-4 code uses a segregated solver to resolve the moderator circulation.

As was shown above, the flow pattern in the Pickering A calandria vessel is controlled by the heat flux to the fan nozzles flow rate ratio. Hence, correct prediction of the flow field inside the fan nozzles is essential for the simulation of flow and temperature fields inside the calandria vessel in the course of LOCA. This work deals with numerical and experimental characteristics of the flow inside the Pickering A type scaled down fan nozzle. PIV flow field measurements are

8

performed in the immediate vicinity of the nozzle outlet. The experimentally obtained flow field is compared with the numerical predictions using a number of turbulence models. Star-CCM+ commercial CFD software was used for the numerical calculations.

2. FLOW FIELD MEASUREMENTS - A SURVEY

The flow field in the present study will be measured outside the nozzle in the free jet region. There exist several techniques to measure the velocity of a fluid flow. Each has benefits and negatives which need to be weighed to determine the one best suited for a specific experiment. This section will present a survey of the today's most widely used flow field measurement techniques.

2.1. Hot-wire anemometry

This is an established intrusive technique for flow velocity measurements. Hot-wire anemometry uses small heated wires to measure fluid velocities. As the fluid passes the small wire, heat will be removed from the electrically heated probe. The technique depends on the convective heat loss to the surrounding fluid from an electrically heated sensing element or probe and on the dependency of the resistance of the wire on its temperature. If only the fluid velocity varies, then the heat loss can be interpreted as a measure of that variable. Hot-wire anemometers have been used for many years in the study of laminar, transitional and turbulent boundary layer flows and much of our current understanding of the physics of boundary layer transition has come solely from hot-wire measurements. Until the advent of laser anemometry or rotating frame instrumentation, this was the only available technique for the acquisition of rotating frame data. Data obtained using hot-wire

anemometers are pointwise data. Hence, to get a plane view of the velocity field numerous measurements are required. The main drawback of hot wire methods stem from their intrusive nature which may cause flow disturbances in the region of interest.

2.2. Laser Doppler Velocimetry - LDV

Laser Doppler Velocimetery (LDV) is a technique used to measure the local velocity of a flow field. This technique, unlike hot-wire anemometry is non-intrusive and can measure all the three velocity components simultaneously. The laser Doppler velocimeter sends a two monochromatic laser beams toward the target region with each beam being at a slightly different phase. When these beams intersect at the measurement location the light undergoes constructive and destructive interference patterns. At the constructive interference locations there is bright light and in the destructive regions there is darkness with the spacing of light being very small and in a single direction. This region of light and dark is referred to as the fringe spacing. As reflective particles within the flow pass through this region they will create a series of light pulses which are received by a photodetector. Since a particle may pass through several of these fringes it will create a series of slight signals with the frequency of these signals providing information of the speed of the reflective particle (seed) in the direction of the fringe spacing. The flow is seeded with small, neutrally buoyant particles that scatter light such their velocity is indicative of the fluid velocity at that location. Multiple light beams of different

frequencies coming from differing directions (and thus with fringe patterns orientated in differing directions from one another) can be focused at the same measurement location to provide simultaneous measurement in 3 directions. Like hot-wire anemometer, LDV measures a point value of the flow velocity.

2.3. Particle Image Velocimetry - PIV

Particle Image Velocimetry (PIV) is a whole-flow-field technique providing instantaneous velocity vector measurements in a cross-section of a flow. Two velocity components are measured, but use of a stereoscopic approach the method may permit all three velocity components to be recorded, resulting in instantaneous 3D velocity vectors for the whole area. The use of modern digital cameras and dedicated computing hardware, results in real-time velocity maps.

In PIV, the flow is illuminated in the target area with a laser sheet. Once a seed particle passes through a lit area it generates a pulse of reflected light which is recorded by a CCD camera. Once a sequence of two light pulses is recorded in two successive planes, the images are divided into small subsections called interrogation areas (IA). The interrogation areas from each image frame, I1 and I2, are cross-correlated with each other, pixel by pixel. The correlation produces a signal peak, identifying the common particle displacement. An accurate measure of the displacement - and thus also the velocity - is achieved with sub-pixel interpolation. A velocity vector map over the whole target area is obtained by repeating the cross-correlation for each interrogation area in the frame.

As the results obtained employing the PIV technique are similar in form to those

obtained with the use of computational fluid dynamics and real-time velocity maps

are an invaluable tool for fluid dynamics researchers. This technique was chosen to

be applied in the present study due to its ability to provide results in a form

convenient to compare to CFD predictions. This way computational tools, including

numerical and physical models, can be validate

3. RANS MODELLING OF TURBULENT FLOWS

Computation Fluid Dynamics is a method for modeling fluid behaviour numerically within a given geometry with specified fluid properties and boundary/initial conditions. It is used to simulate the fluid flow field on a much more precise scale than the 1-dimensional thermal hydraulic codes usually employed for nuclear reactors safety assessment, and there is increasing interest in using CFD to assist in, or to perform, safety analysis. The basic principle of CFD is that the domain of interest is split into a large number of small cells (finite volumes) with simple geometries such as tetrahedrons or hexahedrons. The discretized equations of conservation of mass, momentum and energy are solved to predict the flows, pressure and temperature between each cell. Such simulations require iterative numerical methods due to the non-linear second order coupled partial differential equations involved. The simulations can be calculated as a steady state or as a time dependent system with the time being also discretized for the latter.

Single phase fluid flow can be categorized into two different types: laminar and turbulent. Laminar flow occurs at lower Reynolds numbers which is the simpler of the two types of flow. The Reynolds number, Re, is a measure of flow inertia to viscous forces within a flow field. The higher the Re number the more turbulent, or unsteady, the local flow field. Turbulent flow occurs at higher Reynolds numbers general above 4000 for internal flows. This type of flow is more complex than

T.M.J. Sheasgreen
M.A.Sc. Thesis

Chapter 3
RANS Modeling of Turbulent Flow

McMaster University
Engineering Physics

laminar flows since turbulent fluctuations are superimposed on the mean or average velocity. Solving the complete set of conservation equations numerically for high Re numbers is impractical. In most engineering applications, Reynolds averaged equations are solved instead. All the flow variables are being decomposed into time averaged and fluctuative parts. The Navier-Stokes equations momentum conservation equations in their Reynolds averaged (RANS) are presented in equations (1-3) - see e.g. Versteeg and Malalasekera, 2007.

$$\frac{\partial U}{\partial t} + div(\boldsymbol{U}U)$$

$$= -\frac{1}{\rho}\frac{\partial P}{\partial x} + vdiv(grad(U))$$

$$+ \frac{1}{\rho}\left[\frac{\partial\left(-\rho\overline{u'u'}\right)}{\partial x} + \frac{\partial\left(-\rho\overline{u'v'}\right)}{\partial y} + \frac{\partial\left(-\rho\overline{u'w'}\right)}{\partial z}\right]$$

(1)

$$\frac{\partial U}{\partial t} + div(\mathrm{V}U) = -\frac{1}{\rho}\frac{\partial P}{\partial y} + vdiv(grad(U))$$

$$+ \frac{1}{\rho}\left[\frac{\partial\left(-\rho\overline{u'v'}\right)}{\partial x} + \frac{\partial\left(-\rho\overline{v'v'}\right)}{\partial y} + \frac{\partial\left(-\rho\overline{v'w'}\right)}{\partial z}\right]$$

(2)

$$\frac{\partial U}{\partial t} + div(WU)$$

$$= -\frac{1}{\rho}\frac{\partial P}{\partial z} + vdiv(grad(U))$$

$$+ \frac{1}{\rho}\left[\frac{\partial\left(-\rho\overline{u'w'}\right)}{\partial x} + \frac{\partial\left(-\rho\overline{v'w'}\right)}{\partial y} + \frac{\partial\left(-\rho\overline{w'w'}\right)}{\partial z}\right]$$

(3)

Different turbulence models are used to represent the so called Reynolds stresses (the tag terms on the RHS of equations 1-3). Some of the most used engineering turbulent models including the k-ε, k-ω, Reynolds Stress Models (RSM) and Spalart-Allmaras, will be discussed in the following sections. Each of these models work better in different situations and must be chosen accordingly. The k-ε model and the RSM are primarily valid for turbulent core flows (i.e., the flow in the regions somewhat far from walls). The Spalart-Allmaras and k-ω models were designed to be applied throughout the boundary layer, provided that the near-wall mesh resolution is sufficient. For isothermal incompressible flows, all RANS based turbulence models solve equations (1-3), mass conservation equation and additional equations to solve for the Reynolds stresses.

3.1. k-ε model

The k-ε model is one of the most widely used turbulence model for flow in various scenarios and is known as a two equation variable eddy-viscosity model. The two

16

variables that it uses are turbulent kinetic energy (k) and the turbulent dissipation

(ε). Standard k-ε is a linear and isotropic viscosity model, and it will generally fail

to predict secondary velocities to great accuracies – see Sotiropoulos (2007). In

order to calculate the Reynold stresses the Boussinesq hypothesis is used, which

relates the stresses to the mean rates of deformation.

$$\frac{\partial(\rho k)}{\partial t} + div(\rho k U) = div\left[\frac{\mu_t}{\sigma_k} grad(k)\right] + 2\mu_t \cdot S_{ij} \cdot S_{ij} - \rho\varepsilon$$

(4)

$$\frac{\partial(\rho\varepsilon)}{\partial t} + div(\rho\varepsilon U) = div\left[\frac{\mu_t}{\sigma_\varepsilon} grad(\varepsilon)\right] + C_{1\varepsilon}\frac{\varepsilon}{k} 2\mu_t \cdot S_{ij} \cdot S_{ij} - C_{2\varepsilon}\rho\frac{\varepsilon^2}{k}$$

(5)

These two equations describe the total rate of change of ε and k in a finite volume.

The terms from left to right represent: rate of change, transport by convection, and

transport by diffusion, rate of production and rate of destruction. It should be noted

that while equation for turbulent kinetic energy is rigorously derivable from the

RANS equations, the equation for ε is derived based on intuition and cannot be

rigorously derived to the presented form. This model is applicable in most situations

with complex recirculation areas in flow. More information can be found in

Launder and Spalding (1974).

3.2. k-ω model

The k-ω model is also two equation turbulence model based on the RANS

equations. The two transported variables are turbulent kinetic energy and turbulence frequency. The conservation equation for ω is based on principles similar to that of ε equations. As with k-ε, the standard k-ω is a linear model meaning it will be generally unable to predict to great accuracy secondary velocities. There are non-linear (anisotropic) versions of the k-ω model that would allow for more accurate prediction of secondary motion (Sotiropoulos, 2000).

$$\frac{\partial(\rho k)}{\partial t} + div(\rho k U) = div[(\mu + \mu_t \sigma_k)grad(k)] + P_k - \beta^* \rho k \omega$$

(6)

$$\frac{\partial(\rho \omega)}{\partial t} + div(\rho \omega U)$$

$$= div[(\mu + \mu_t \sigma_\omega)grad(\omega)] + \gamma_1 \left(2\rho \cdot S_{ij} \cdot S_{ij} - \frac{2}{3}\rho \omega \frac{\partial U_i}{\partial x_j}\delta_{ij} \right)$$

$$- \beta_1 \rho \omega^2$$

(7)

Another version of this model is Shear Stress Transport (SST) model which combines k-ε and k-ω. The transport equation for k is the same but the ε transport equations changes into:

$$\frac{\partial(\rho \omega)}{\partial t} + div(\rho \omega U)$$

$$= div\left[\left(\mu + \frac{\mu_t}{\sigma_{\omega,1}} \right) grad(\omega) \right]$$

$$+ \gamma_2 \left(2\rho \cdot S_{ij} \cdot S_{ij} - \frac{2}{3}\rho \omega \frac{\partial U_i}{\partial x_j}\delta_{ij} \right) - \beta_2 \rho \omega^2 + 2\frac{\rho}{\sigma_{\omega,2}\omega}\frac{\partial k}{\partial x_k}\frac{\partial \omega}{\partial x_k}$$

(8)

The model uses the k-ω model for near wall areas and the k-ε model for fully turbulent areas in the core region of the flow field. SST is also better suited for adverse pressure gradients. More information can be found in Wilcox (1988) and Menter (1992).

3.3. Reynolds Stress Model - RSM

The Reynolds stress model is one of the most complex turbulence models based on RANS approximations. It uses six partial differential transport equations to describe the six Reynolds stresses (six and not nine because of the symmetry of the turbulent stress tensor), instead of modelling them based on e.g. Boussinesq hypothesis. Usually, a transport equation for ε is also used and each stress is attributed its own equation, which allows RSM to predict anisotropic flows much better than k-ε or k-ω. This model is used for flows that contain significant secondary flows and or high levels of anisotropic turbulence. As it uses more equations than k-ε or k-ω the calculation time is significantly higher for this turbulence model and satisfactory convergence may be more difficult to achieve. For more information see Launder et al. (1975).

$$\frac{DR_{ij}}{Dt} = \frac{\partial R_{ij}}{\partial t} + C_{ij} = P_{ij} + D_{ij} - \varepsilon_{ij} + \pi_{ij} + \Omega_{ij}$$

(9)

The terms in the equation correspond to

1. Rate of change of R

2. Transport of R by convection

3. Rate of production of R

4. Transport of R by diffusion

5. Rate of dissipation of R

6. Transport of R due to turbulent pressure-strain interactions

7. Transport of R due to rotation

$$C_{ij} = \frac{\partial(\rho U_k u'_i u'_j)}{\partial x_k} = div(\rho u'_i u'_j U)$$

(10)

$$P_{ij} = -\left(R_{im}\frac{\partial U_j}{\partial x_m} + R_{jm}\frac{\partial U_i}{\partial x_m}\right)$$

(11)

$$\Omega_{ij} = -2\omega_k(u'_j u'_m e_{ikm} + u'_i u'_m e_{jkm})$$

(12)

$$D_{ij} = \frac{\partial}{\partial x_m}\left(\frac{v_t}{\sigma_k}\frac{\partial R_{ij}}{\partial x_m}\right) = div\left(\frac{v_t}{\sigma_k}grad(R_{ij})\right)$$

(13)

Where $v_t = C_\mu \frac{k^2}{\varepsilon}$, $C_\mu = 0.09$ and $\sigma_k = 1.0$

$$\varepsilon_{ij} = \frac{2}{3}\varepsilon\delta_{ij}$$

(14)

$$\Pi_{ij} = -C_1\frac{\varepsilon}{k}\left(R_{ij} - \frac{2}{3}k\delta_{ij}\right) - C_2\left(P_{ij} - \frac{2}{3}P\delta_{ij}\right)$$

(15)

Where $C_1 = 1.8$ and $C_2 = 0.6$

$$\frac{D\varepsilon}{Dt} = div\left(\frac{v_t}{\sigma_\varepsilon}grad(\varepsilon)\right) + C_{1\varepsilon}\frac{\varepsilon}{k}2v_t S_{ij} \cdot S_{ij} - C_{2\varepsilon}\frac{\varepsilon^2}{k}$$

(16)

Where the terms of the equation correspond to (left to right):

1. Rate of change of ε

2. Transport of ε by convection

3. Transport of ε by diffusion

4. Rate of production of ε

5. Rate of destruction of ε

3.4. Spalart-Allmaras model

This model involves a transport equation for the kinematic eddy viscosity parameter $\hat{v}$, using one equation. Spalart-Allmaras is best used in flow conditions that have little to no flow separation.

$$\frac{\partial(\rho v)}{\partial t} + div(\rho v U)$$

$$= \frac{1}{\sigma_v} div\left[(\mu + \rho v)grad(v) + C_{b2}\rho\frac{\partial v}{\partial x_k}\frac{\partial v}{\partial x_k}\right] + C_{b1}\rho v\hat{\Omega}$$

$$- C_{w1}\rho(\frac{v}{\kappa_y})^2 f_w$$

(17)

Where the terms of the equation correspond to (left to right):

1. Rate of change of viscosity parameter

2. Transport of v by convection

3. Transport of v by turbulent diffusion

4. Rate of production of v

5. Rate of dissipation of v

The eddy viscosity parameter is further used to calculate the turbulent viscosity and, employing the Boussinesq approximation, the Reynolds stresses are calculated. For more information see Spalart and Allmaras (1992).

3.5. Wall models

Turbulent flows are significantly affected by the presence of walls. Close to the wall both the tangential and normal velocity and their fluctuations decrease to zero due to the no-slip condition. Toward the outer part of the near-wall region, however, the turbulence is rapidly augmented by the production of turbulence kinetic energy due to the large gradients in mean velocity.

The wall modeling significantly impacts the flow field since a large amount of turbulence is generated in the buffer layer between this near wall region and the core of the flow. Furthermore it is typically the region of highest gradients and hence is the most difficult to resolve numerically. Therefore, accurate representation of the flow in the near-wall region determines successful predictions of wall-bounded turbulent flows that are the subject of the present study - flow inside the fan nozzle.

Numerous experiments have shown that the near-wall region can be largely subdivided into three layers. In the innermost layer, called the "viscous sublayer", the flow is almost laminar, and the (molecular) viscosity plays a dominant role in momentum and heat or mass transfer. In the outer layer, called the fully-turbulent layer, turbulence plays a major role. Finally, there is a buffer layer region between the viscous sublayer and the fully turbulent layer where the effects of molecular viscosity and turbulence are equally important.

There are two approaches to modeling the near-wall region. In one approach, the viscosity-affected inner region (viscous sublayer and buffer layer) is not resolved. Instead, semi-empirical formulas called "wall functions" are used to bridge the viscosity-affected region between the wall and the fully-turbulent region. The use of wall functions obviates the need to modify the turbulence models to account for the presence of the wall. In another approach, the turbulence models are modified to enable the viscosity-affected regions to be resolved with a mesh all the way to

the wall, including the viscous sublayer.

Three types of wall treatment are provided in STAR-CCM+, although all three might not always be available, depending on the turbulence model (see STAR-CCM+ user manual):

• The high-y+ wall treatment implies the wall-function-type approach in which it is assumed that the near-wall cell lies within the logarithmic region of the boundary layer.

• The low-y+ wall treatment is suitable only for low-Reynolds number turbulence models in which it is assumed that the viscous sublayer is properly resolved.

• The all-y+ wall treatment is a hybrid treatment that attempts to emulate the high-y+ wall treatment for coarse meshes and the low-y+ wall treatment for fine meshes. It is also formulated with the desirable characteristic of producing reasonable answers for meshes of intermediate resolution (that is, when the wall-cell centroid falls within the buffer region of the boundary layer)

4. SEPARATE EFFECT STUDY

The design of the fan nozzle employed for the moderator flow inlets in some CANDU reactors is complicated. The flow area transitions from circular to rectangular cross section prior to flow division into four streams through an expanding flow area. The conduit area transition flows are highly three dimensional and involves flow boundary layer separation and reattachment, streamline curvature, and recirculating internal flows. Another feature of the flow in the fan nozzle employed in Bruce A reactor is flow through the bended pipe. This flow is characterized by a strong shear and boundary layer separation in the vicinity of the bend. The correct prediction of these flow features is imperative for the flow modelling through the fan nozzle of the CANDU reactors.

While the turbulent flow through a circular duct is relatively simple, the flow through compound channels where the spanwise average velocity and streamwise vortices arise is complicated and presents a challenge to CFD modelling. The flow through the rectangular channel is known to have corner vortices as was reported by e.g. Melling and Whitelaw (1976) who conducted an experimental study. These vortices are not being captured by the turbulent models based on linear turbulent viscosity assumptions - see discussion in Demuren and Rodi (1984).

Experiments reported by Miau et al (1996) show that a transition duct will cause

swirling effects to become present. The fluid motion caused by the transition results in non-uniform pressure distribution across the flow (Miau et al, 1996). In the circular to rectangular transition duct experimentally studied by Davis and Gessner (1992), the curvature of the walls in the transition part of the duct induces pressure-gradients in the crossflow plane, driving relatively strong secondary flows that develop into two contra-rotating vortex pairs. These vortices formed close to the wall and cause flow disturbances both upstream and downstream of their location. The cross-sectional area of the duct varies in the divergent-convergent transition part of the duct, and this further complicates the flow.

4.1. Experiments by Davis and Gessner (1992) on transition duct

Experiments on the flow through transition duct of various geometries are being reported since the 1930's – see Davis (1991) for a review. One of the latest and mostly cited studies on the topic was that of Davis and Gessner (1992). As the flow through the transition duct comprises part of the flow features characteristics of the CANDU fan nozzle, the experiments performed by Davis and Gessner will serve as a separate effect study.

The tabulated experimental data is readily available in the ERCOFTAC internet data base. The geometry of the transition duct employed by Davis and Gessner (1992) is presented in Figure 1.
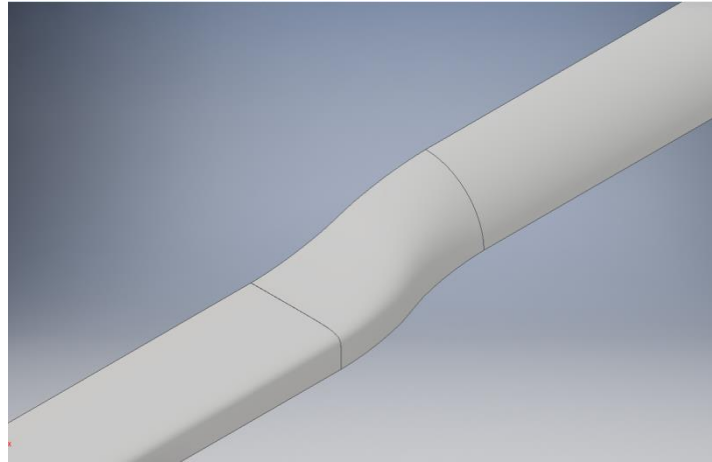
Figure 1: Transition duct

The duct cross sections can be defined by a super-ellipse throughout the entire length.

$$\left|\frac{x}{a}\right|^r + \left|\frac{y}{b}\right|^r = 1$$

(18)

The cross section areas of the circular and rectangular sections are the same, i.e. the cross sectional average velocity was the same throughout the duct.

The experiment was performed with air flowing through the duct at different speeds and measurement being taken at various locations along the duct. Two different Reynolds numbers were chosen for the experiment, 88000 and 390000. The bulk velocity of the air at a Reynolds number of 390000 was 29.95 m/s. Wall static pressures have been measured through 0.508 mm wall pressure taps. Wall shear stresses have been measured using Preston tubes with different diameters ranging from 1.067 mm to 3.073 mm. Hot-wire measurements were taken at six locations

along the duct.

The transition duct studied by Davis and Gessner (1992) was calculated with RANS based turbulence models by Sotiropoulos and Patel (1995) using the k-ε model. It did not accurately predict the vortices that are formed close to the duct walls. Little secondary motion was calculated by this model and there was very little flow disruption. As with the axial velocity the underprediction of the vortices meant that the turbulent kinetic energy was more continuous and showed much smoother contours. k-ε was not able to compute the complex motions of the vortices formed in the duct as it is based on the Boussinesq approximation of turbulent stresses, as mentioned by Sotiropoulos (2000).

A version of RSM was also used by Sotiropoulos and Patel (1995) in the analysis of the transition duct. This used the equations of Gibson and Launder (GL), and was compared to the closure model of Launder and Shima (LSH). The GL model was not accurate in depicting the velocity profile of the duct and had results similar to those by k-ε model. The LSH model was much more accurate in predicting the vortices in the duct with the velocity and vorticity contours much closer to the experimental values than those obtained with other turbulence models used (Sotiropoulos and Patel, 1995). Sotiropoulos and Patel did other analysis with RSM (1994). As was stated in (Sotiropoulos, 2000), RSM are the appropriate choice as they are well suited for calculating secondary flows.

Additional numerical analysis of the transition duct using RSM are reported by

Sugiyama, Akiyama and Hitomi (1999). The employed turbulence model was able to recreate the secondary motion and vortices that were observed in the experiment. Comparing the axial velocity and vorticity contours the RSM shows much closer results than what was attainable with the k-ε or k-ω models. The predicted size and location of the vortices was much closer to the experimental values. Axial velocity contours were very similar to those of the experiment. Gerolymos and Vallet (2016) also simulated the transition duct using RSM and had close agreeing with several variables as well.

4.2. Bended pipe flow

Given the flow redirection in CANDU fan-nozzle, separate effect tests were also considered for flows passing through 90-degree bends. Measurements and predictions using the k-ω model in a 90° bent rectangular duct were performed by Kim and Patel (1994). Measurements were taken at various location including the inlet, within the bend radius, and at the outlet. Comparing the results of the k-ω model and the experiments showed that it was not capable of accurately predicting the secondary velocities present in the duct. A report by Sotiropoulous (2000) showed that Kim and Patel also used a k-ε model which, similar to the k-ω model, failed to accurately describe the vortices and secondary motions that were observed.

Patel also used two different nonlinear variants of the k-ω model and both much more accurate than the isotropic viscosity models. Both were able to predict the vortices to some degree, with some discrepancy of the location of the vortex core.

The comparison between the nonlinear and linear models shows the ability of anisotropic models to better predict complex secondary motion such as vortices (Sotiropoulos, 2000) within pipe bends.

5. MODELING TRANSITION DUCT - PRESENT STUDY

Numerical computation of the transition duct experimentally studied by Davis and Gessner (1992) was performed as a preliminary step towards the final simulation of flow through Pickering nozzle.

5.1. Meshing

Dimensions of the transition duct were taken from the PhD thesis of Davis (1991) and used to prepare a 3D CAD model. Figure 2 shows the duct geometry as imported into STAR-CCM+. A quarter section of the duct was used in the simulation as symmetry in the x and y axis was assumed, and this is supported through examination of the experimental results which showed a high-degree of symmetry. A STAR CCM+ trimmed mesh was used as the flow within the duct is mainly aligned with the global coordinate system Z-axis direction. Using a trimmed mesh allows for a decrease in computing time relative to an unstructured grid which would require significantly more computational cells. Since the imported geometry only consisted of the transition portion of the duct, an extruded mesh was used to extend the mesh upstream and downstream to cover the entire domain of interest. Figure 3 shows a longitudinal cross section of the initial mesh close up of the transition, with an extrusion of the inlet and outlet.
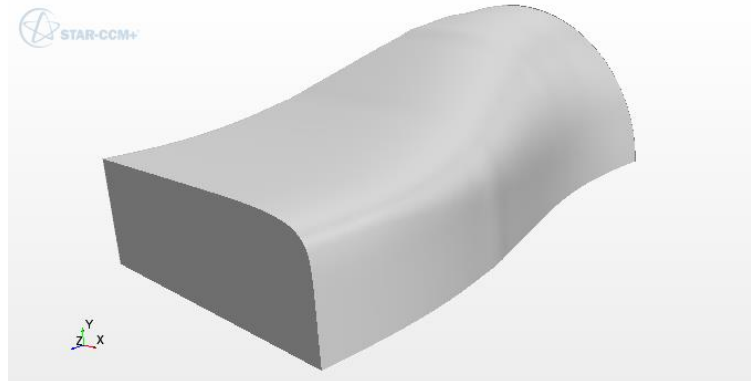
Figure 2. Transitional duct geometry (Quarter section)
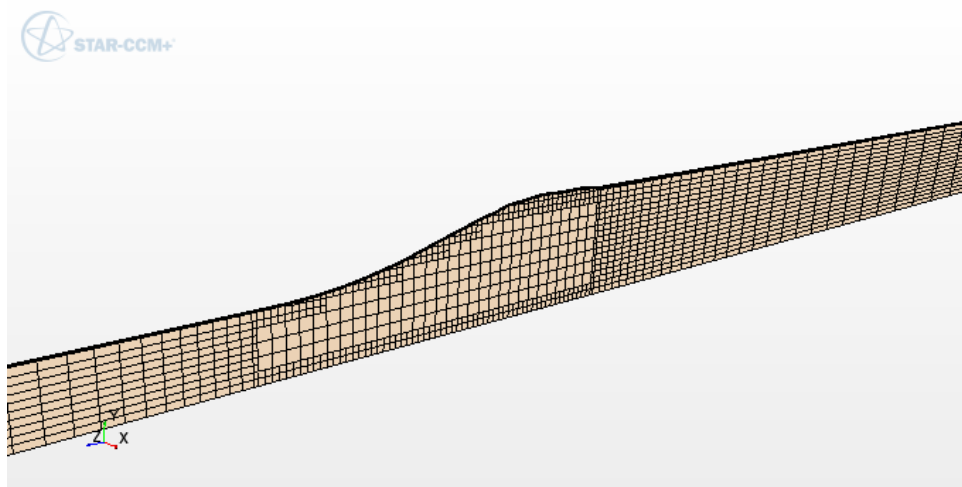
Figure 3. Computational grid - streamwise section view

The inlet and outlet extrusions both have increasing cell lengths as they both extend over relatively large distances where streamwise flow field gradients are assumed to be small. For the initial simulations the computing time was kept to a minimum as the wall grid was coarse enough to assure wall Y+ value of approximately 100.

For theses initial simulations the realizable version of k-ε turbulence model was used. This model was chosen as it is a model that is applicable to a larger range of flow conditions. Data was taken from six different sections along the duct (Table 1 shows the plane locations). Station 2 is located at the beginning of the transition section from the circular end of the duct.

Table 1. Measurement locations along the transition duct – Davis (1991)

Station	Location (x/r)
1	-2
2	0
3	1.2
4	1.8
5	3
6	7

5.2. Simulation results of transition duct

Using an initially coarse mesh (see Figure 3) and abbreviated inlet development length, the results were compared to the data from Davis (1992). Figure 4 shows the axial velocity contours at stations 6 (see Table 1) of the simulation compared to

the experiment. The top portion shows the data from the simulation and the bottom

shows the experimental results.
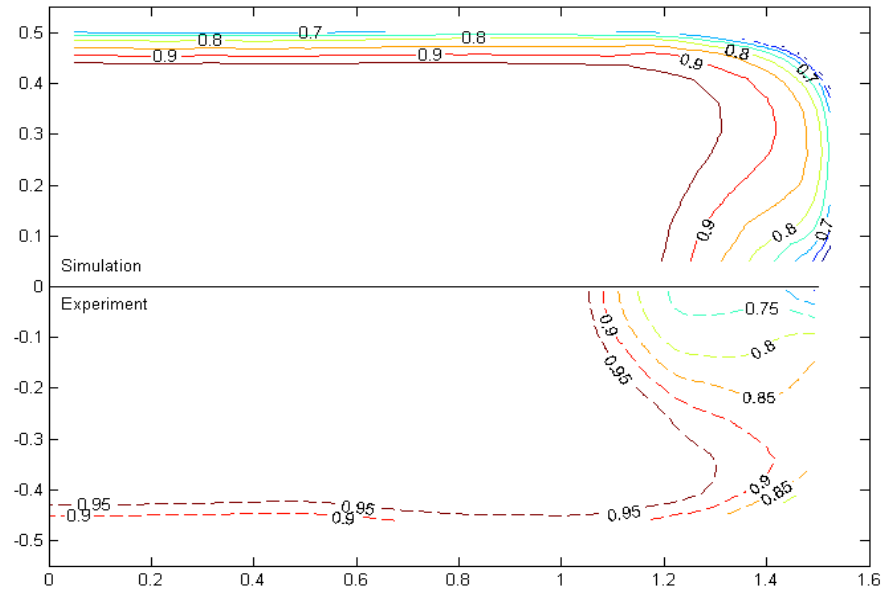
Figure 4. Axial velocity of simulation (top) and experiment (bottom) at

station 6.

The contours shown (both experimental and calculated) are normalized by the bulk

axial flow (29.95 m/s). The x and y coordinates are normalized by the inlet radius

(10.214 cm). The computed velocity contours are qualitatively similar to those

obtained experimentally, however the simulations show much larger gradients in

the wall region as compared to the experiment.

5.3. Sensitivity Analyses

After comparing axial velocity, transverse velocity, pressure and turbulent kinetic

energy, additional simulations were performed to determine the sensitivity to inlet

conditions. The initial simulation used an inlet circular pipe length of 20 diameters.

To determine the effects of the inlet conditions several simulations were run with

an increasing inlet development length. Each simulation was run with an additional

20 diameters of inlet length. As the inlet development length was increased the

simulations showed smaller gradients and hence improved agreement with the

experiments, although such gradients were still over predicted. Figure 5 shows the

axial velocity of the simulation with an 80 diameter inlet length compared to the

experimental results.
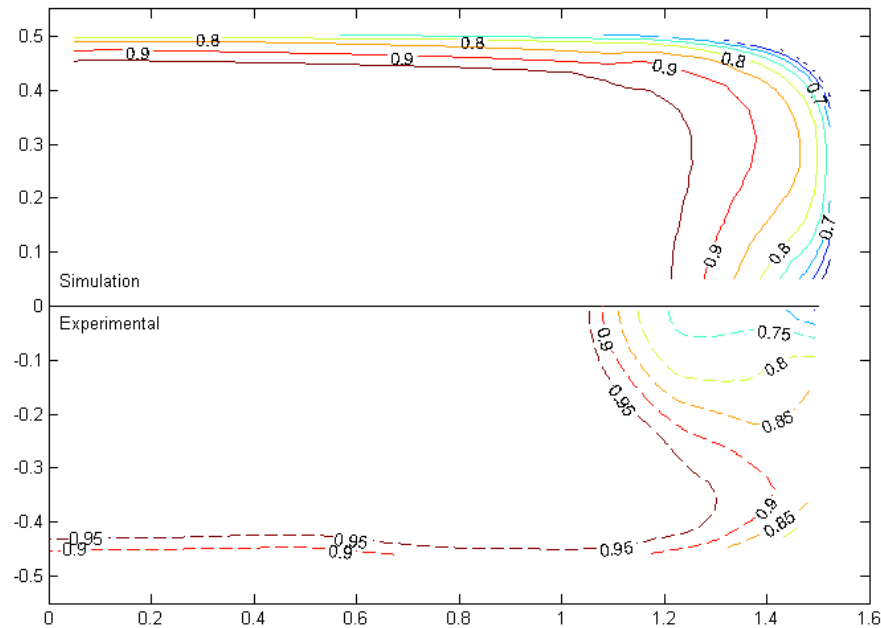
Figure 5. Axial velocity of simulation (top) with 80 diameter inlet and

experiment (bottom)

The inlet development length was further increased from 80 to 120 diameters with little to no change in the calculated results.

To determine the mesh sensitivity additional simulations with more nodes and a refined mesh topology were used. The initial simulation used approximately 50000 nodes. The number of nodes was increased throughout the domain including the near wall region, thus decreasing the wall Y+. Using finer meshes gave better results when comparing the velocity profiles to those of the experiments. The number of nodes was increased to 750000 and a boundary layer mesh was employed to assure Y+ of the order of unity. Figure 6 shows the impact of grid refinement on axial velocity profile.
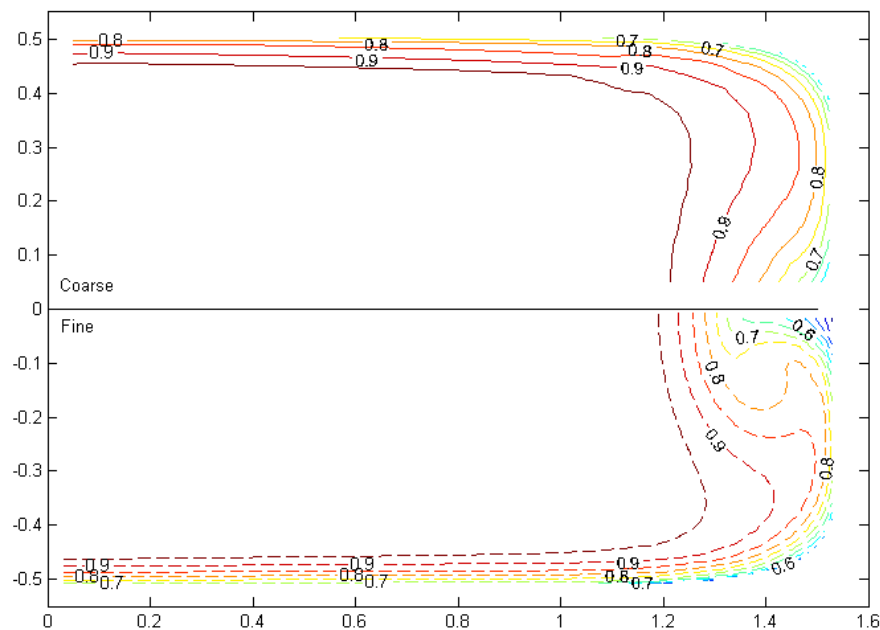
Figure 6. Fine and coarse mesh comparison (axial velocity)

After comparing the meshes the coarser meshes may not have been properly converged compared to the finer meshes. As other comparisons used the coarser mesh it may be that the other simulations may have proper mesh convergence.

After the inlet and mesh sensitivities were analyzed the turbulence model was then changed to k-ω sst. The same geometry was used but to decrease computational time, the mesh was changed to a coarser version. The simulation of the k-ω turbulence model used an inlet length of 80 diameters, with approximately 500000 nodes and a y+ of 40. Figure 7 shows the axial velocity contours of the k-ε and k-ω simulations. The results with the k-ω model were similar to those of k-ε.
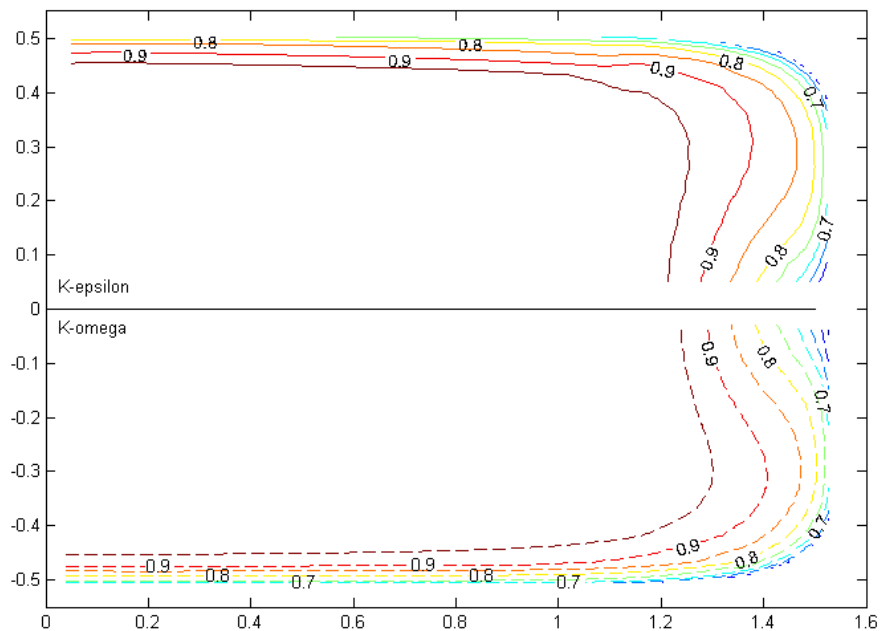
Figure 7. Axial velocity: k-ω vs k-ε

Finally, an RSM turbulence model was used with the coarser mesh. While the simulation would not converge when using linear two-layer pressure strain formulation, it would converge using elliptical blending. In the linear two-layer pressure strain formulation, the pressure strain is calculated in two different sections: the first is a near wall area where the turbulence dissipation rate and turbulence viscosity are functions of wall distance. The next layer uses a blending function with the values from the general turbulence model calculations. The elliptical method uses a higher order calculation to determine pressure strain, and blends the sub layer with the log layer. Figure 8 shows the RSM and experimental results. The results from RSM were very similar to those of k-ω and k-ε models. As no significant improvement of the results was achieved using the RSM model, it will not be employed for the final nozzle calculation being computationally much more demanding than two-equation models.
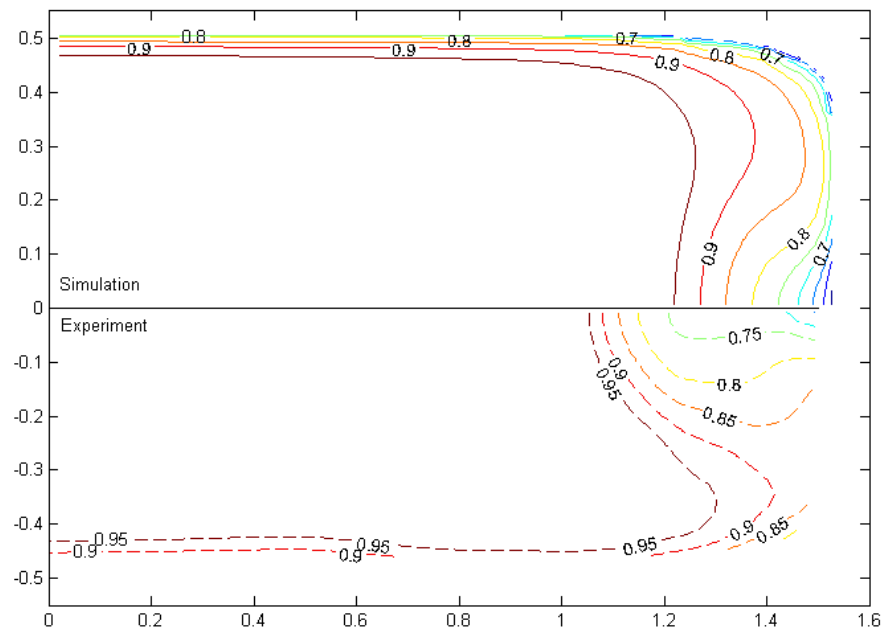
Figure 8. RSM vs experimental axial velocity

Using a different mesh on the simulations used for comparison may give different
predictions and the conclusions from this section may change on which turbulence
model should be used for the final simulation. As well as any instabilities would be
difficult to model with a symmetrical simulation.

6. FAN NOZZLE - EXPERIMENTAL AND CFD SET-UPS

In this section, the method of setup of PIV laser experiments and CFD simulations description will be presented.

6.1. PIV setup

Figure 9 presents the side (left), the front (middle) and the bottom (right) views of the experimental fan-nozzle used in the present study. Water was circulated from a storage tank and flow was measured using a calibrated MHD flow meter. Water from the nozzle was injected into a tank of water and PIV measurements were obtained at various locations and orientations at the exit of the fan.
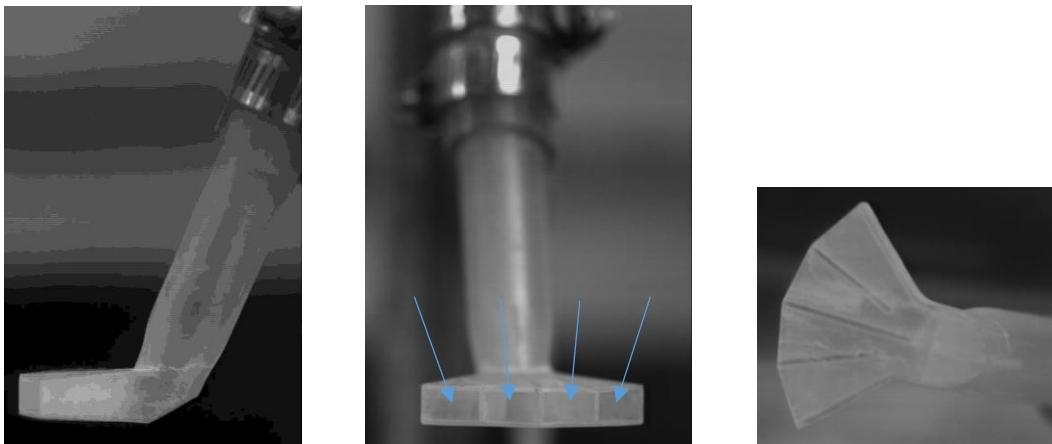
Figure 9. Experimental fan nozzle.

Seven measurement planes were taken on each of the four outlets (see arrows in

Figure 9 middle) at two different flowrates. The PIV laser measurement system allows for a plane view of fluid velocities to be measured, while predictions on these specific planes can be extracted from the CFD simulation for comparison. The PIV laser was fitted with a light arm attachment which allows the laser to be set up in different directions using mirrors placed in the arm, which has several sections that allows it to be orientated at a desired orientation. This allows the beam to be placed in different locations without having to move the laser itself. The end of the light arm, where the laser is emitted towards the nozzle, was mounted on a rail so that it could be moved to take measurements on different planes, parallel to each other, without having to move the nozzle and to ensure that the laser positions was repeatable. The end of the light arm was secured to the rail with a small platform that holds it steady. The nozzle was mounted in a glass tank at different orientations so that different planes can be measured and for all measurements the tank walls were a considerable distance from the nozzle exits. Planes were measured as follows:

● vertical planes, the nozzle was placed with the outlet facing the light arm, located at the far end of the tank (see Figure 9, left). Three planes were measured with one in the middle and two 3mm to either side (see Figure 11).

● direct planes, the nozzle was moved to the side of the tank with the outlet facing the camera so that the laser sheet would shine across the face at the edge of the nozzle (see Figure 9, center). One plane was measured on the outlet face (see Figure 12).

● horizontal planes, a different connecting pipe was used which was shorter so that it could fit in the tank while laid lengthwise. The nozzle is placed so that the outlet that is being studied would face the light arm with the sides level with the bottom of the tank (see Figure 9 (right)). Three planes were measured, one in the middle and two 2 mm on top and bottom (see Figure 13).

In order to accurately determine the laser position and orientation a wedge was designed to be placed in the outlets of the nozzle that was used for the laser alignment. The tapered end of the wedge is designed to fit snuggly into each of the fan-nozzle openings. Figure 10 shows the shape of the wedge. The pin on the face of the wedge allows for level measurements with reference to the camera for each face. Once the laser illuminates on the nozzle, the pin on the wedge will indicate if the nozzle is placed at the desired angle, in which case a shadow would appear and the alignment procedure would be resumed.
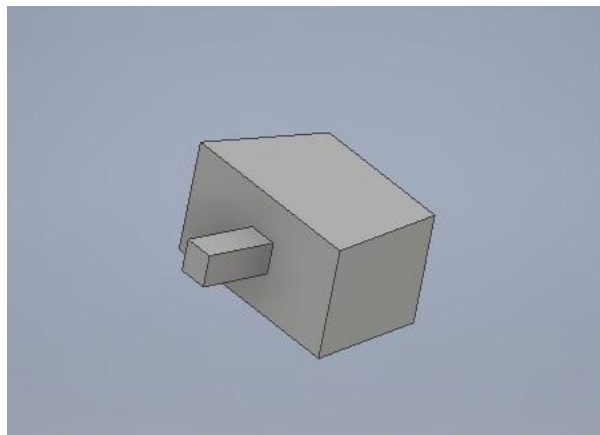
Figure 10. Wedge used for laser alignment

To achieve the best results the camera and emitted laser sheet should be perpendicular to each other. This would ensure that the image of the flow field would not be distorted and one side of the image will not be closer to the camera than the other. The angle of the laser in the tank was checked using a ruler to determine if it was square with the tank. The ruler was placed in the tank with one end being square against the tank wall. The laser sheet was pointed at the ruler so that it could be seen down its length, and could be determined if it was straight. The rail was kept in place by a bar that was secured to the countertop and was used to move the rail while keeping the angle of the laser constant. A level was used to determine if the camera was level to keep the images in the correct orientation. To check the placement of the laser sheet on the nozzle the wedges were inserted into the outlets (see Figure 10). The pin on the wedge placed in the outlet of interest was used to aid the placement of the laser sheet on the desired location. The pin also gave a focusing point when measuring the middle planes. After measurements were taken at the middle planes the rail was moved to the appropriate distance to the planes parallel to its original location. These planes were used for a reference mark placed on the rail, the laser could be moved to the desired distance using the secured bar preventing the need for laser realignment. The pin on the wedge would cast a shadow in the laser light if the nozzle were placed at an angle. Figure 11, Figure 12 and Figure 13 show the locations of the measurement planes on the nozzle for vertical, direct and horizontal orientations respectively.
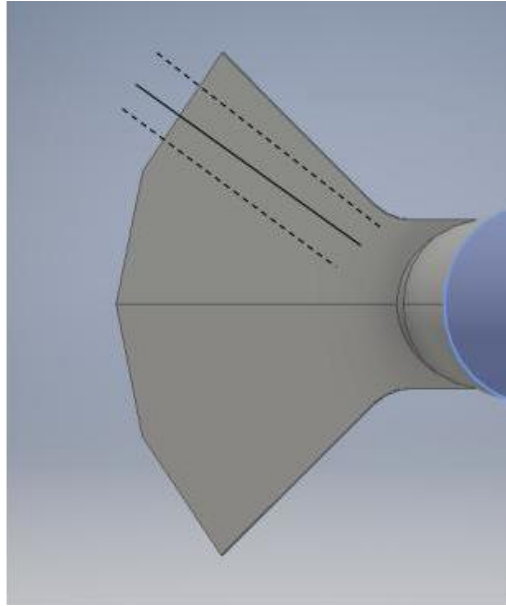
Figure 11. Vertical planes placement on face 1
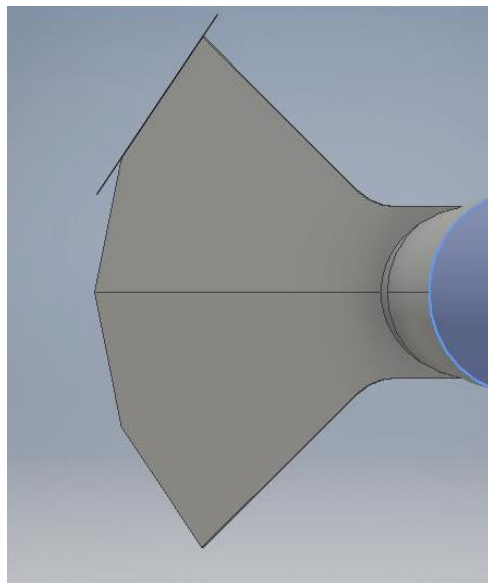
Figure 12. Direct plane placement on face 1
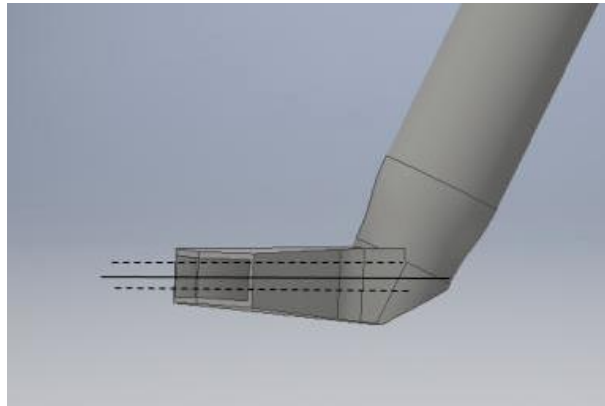
Figure 13. Horizontal plane placement

In order for the flow to be analyzed, tracers (small seed particles following the flow) are injected into the flow so that they will reflect the laser light and appear in the images captured by the camera. Seed particles are placed in the glass tank and in the holding tank, to ensure that the desired seed density for the velocity field being studied. The camera (Photron Fastcam SA5) was focused on the seed particles in the tank as the only particles present in the laser sheet will be visible to the camera. With the camera in focus, the pump was turned on and set to the desired flowrate. The pump (Ebara CDU200) is operated by a potentiometer, and the flow is measured by a magnetic flowmeter (Rosemount magnetic flow tube) and displayed by a digital readout. The flowmeter is accurate to ±0.5% of flowrate from 1 to 10m/s. A synchronizer (TSI Laser Pulse) was used to regulate the timing of the camera and laser pulses. To ensure the system is working properly a pair of images were captured and processed. Then the vector statistics were analyzed, the percentage of acceptable measurements being ideally above 95%. This means that

95% of the velocity vectors calculated by the software are determined to be valid. Next the change in position of the individual particles is checked to determine if the software can properly calculate the velocities. The software shows how many pixels each particle moves in between the two consecutive images captured. Ideally, the region of interest should have particles that move between 3 and 6 pixels. This was assured for all the experiments performed in the present study.

After the images are captured they are reviewed for seed levels. A series of continuous images with appropriate seed levels are chosen and then processed. Processed images are then brought into Tecplot graphing software and averaged so that they may be compared to steady or time-averaged CFD results. Timing was changed on different runs of the PIV to determine the best settings for experiments. Time between images was within the range of 100 to 300 μs.

To verify that the measurements taken with the PIV laser were accurate a professional consultant from TSI did an independent measurement and it was compared to one of the measurement previously taken. Figure 14 shows the middle vertical plane at 0.1 kg/s that was measured with the help of a consultant from TSI with Figure 15 showing the same plane during present study measurements. The two results are similar suggesting that the measurements presented throughout the present study are taken with the equipment properly functioning.
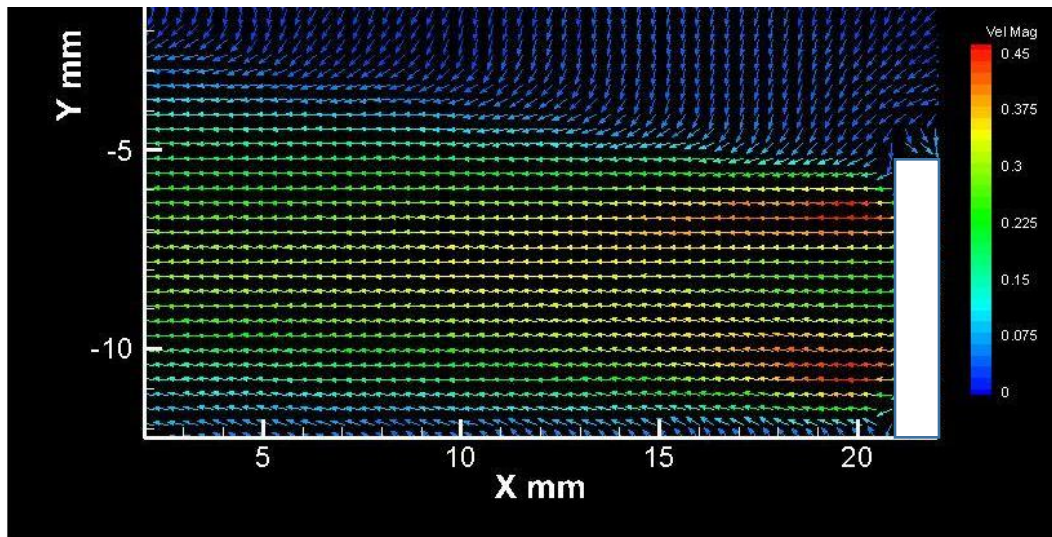
Figure 14. TSI Face 2 middle vertical plane 0.1 kg/s
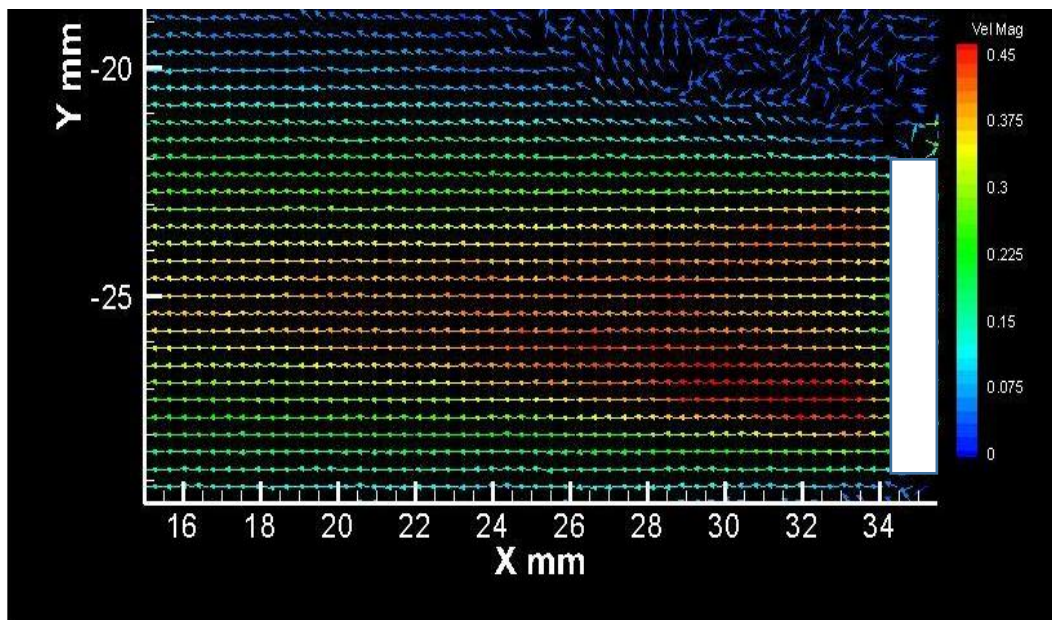
Figure 15. Vertical middle plane 0.1 kg/s

6.2. CFD simulation setup

The flow in the fan-nozzle was modeled using STAR-CCM+ CFD software. A CAD model of the nozzle was imported into the STAR-CCM+ and the internal volume was extracted as the volume of the walls was not needed for isothermal simulations performed in the present study. An external volume was attached to the outlet of the nozzle so that flow outside the nozzle could be predicted and the flow inside the nozzle will not be affected by the uniform pressure outlet boundary conditions at the four nozzle outlet planes. The volume consisted of a fluid region that was wide enough to allow for several diameters of flow outside of the nozzle. First, the geometry of the nozzle was subtracted from the block, and the two were united so that the wall thickness of the nozzle would not be included in the fluid volume. The internal nozzle geometry and the external block geometry were combined and meshed together. Figure 16 shows the entire fluid volume for which the simulation was done.
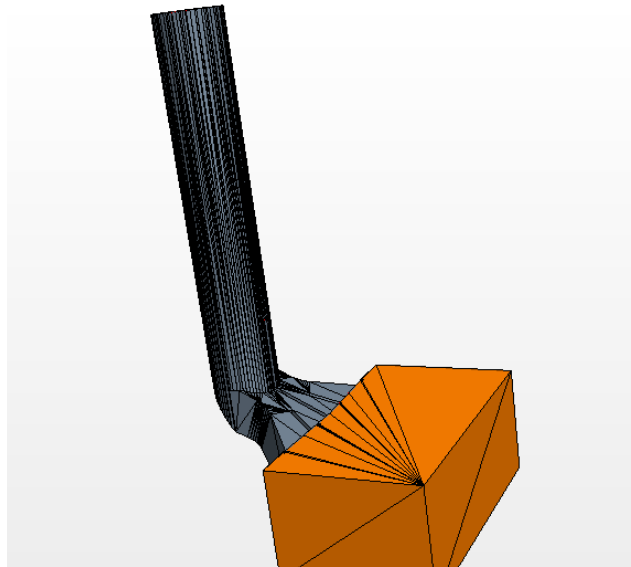
Figure 16. Simulation domain

The volume was meshed first with a trimmed cell mesher and a prism cell boundary

layer. The simulation with the tetrahedral mesh had a higher degree of convergence

than the trimmed cell mesh. A prism layer was used on the walls of the nozzle to

meet desired wall Y+ criterion. The base size of the final mesh used in the

simulation was 0.0025 m, with a size of 100% of the base for the prism layer which

comprised of 5 sub-layers. This size was used so that Y+ values of the order of

unity would be achieved on all the walls in the computational domain. Which is

approximately the same value used in the finer mesh in the separate effect study.

Figure 17 shows the Y+ values on the walls of the nozzle.
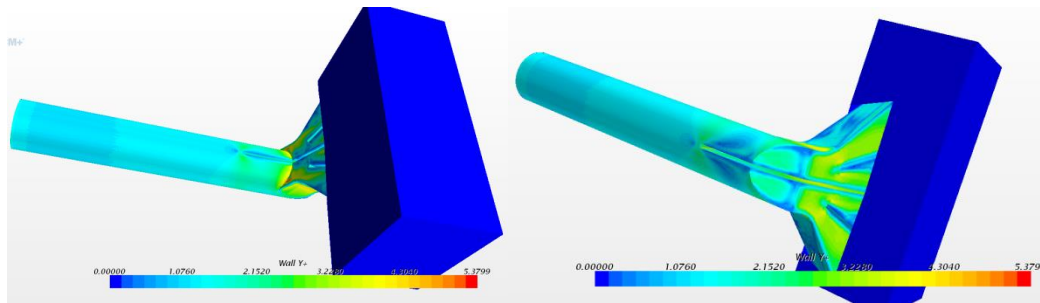
Figure 17. Y+ values on the nozzle walls

To allow for fully developed flow at the inlet a separate simulation was run. A short cylindrical geometry with the same diameter of the inlet of the nozzle was used with a tetrahedral mesh using the same base size and prism layer. Periodic boundary conditions were applied to allow the flow to obtain fully hydrodynamically developed conditions. The case was simulated for the two flow rates and the outlet average velocity profiles were exported to be further used for the nozzle computations inlet conditions (see the domain in Figure 16).

A coarser mesh was used in a simulation for mesh sensitivity analysis. With larger cell sizes and wall nodes but with the nearest wall node being approximately of the same position as for the finer grid. Mesh topology was the same for both grids: tetrahedral mesh with boundary layer. Figure 18 shows the effect of grid refinement on the velocity field in the outlet plane of the nozzle. It is seen that coarser mesh is incapable to resolve the velocity gradients. However, as the maximal and minimal values of the velocity were almost the same for both grids, the fine mesh was adopted in the present study.
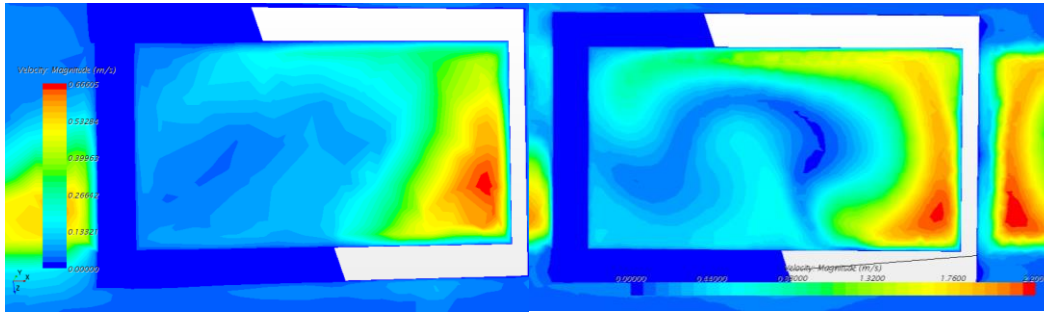
Figure 18. Velocity field - mesh refinement effect.

The turbulence model used was k-ω SST. From the benchmark simulations and literature review it was determined that this model would be best suited for a simulation with a circular to rectangular transition in the flow. Previous works done on comparing turbulence models showed some better agreement between physical measurements and the k-ω sst predictions. For example a study done by Furbo et al. (2009) showed that the sst model to be a better choice with flow separation compared to similar eddy-viscosity models. The turbulence suppression version of the equations were used in the simulations, meaning that in the model near wall turbulence will be suppressed. The all Y+ wall function was used in the final simulations.

Several planes were used to monitor the flow exiting the nozzle in the CFD simulations. These were in the same locations as the planes on the nozzle being measured by the PIV laser. The measurement planes to be compared with the PIV were placed by first creating a new coordinate system on the faces of the four outlets and then using it to properly position the planes.

Finally, due to the complex geometry, boundary layer separation within the nozzle, and the propensity for recirculating flows (spanning 2 to 3 orders of magnitude lower velocities as compared to the average stream wise velocity), the steady-state simulations showed poor convergence characteristics likely because some of these fine features show unsteady behavior. Therefore the results shown below are obtained from transient CFD simulations with a time step of 0.001s with 20 iterations per time step. These transient simulations were analyzed to assess the level of "steadiness" in the flow (i.e., how much key parameters are time dependent). The results show some time dependence in TKE although the variations are small, and this is likely the reason for the poor steady-state convergence characteristics. Therefore all of the results discussed in Chapter 7 are obtained at the end of these long duration transient CFD simulations. Further details are provided in Section 7.3. In addition, a simulation using the k-ε model was used to compare with the k-ω simulation. The simulation used a steady state model, opposed to a transient model, as it showed much better convergence than the k-ω simulation.

7. RESULTS AND DISCUSSION

In this chapter the PIV measurements CFD predictions are presented. For brevity, only the results of one flowrate (0.2 kg/s) will be discussed, other results appear in the Appendix. Figure 19 shows the nozzle geometry and the outlet ports numbered from 1 to 4. Measurements were taken on two of the four outlets as symmetry was assumed. In order to observe a large portion of the velocity field seven different planes were used as measurement positions which were discussed in the experimental setup section.

While taking the measurements the orientation of the nozzle was set so that on vertical planes the top of the graph corresponds to the top of the outlet. The horizontal orientation is so that the top of the graph corresponds to the side of the outlet closest to the middle of the nozzle. The direct planes are orientated so that the top of the graph corresponds to the top of the outlet. Given that the CFD results are calculated with much finer spatial resolution than the PIV results, CFD predictions are post processed and area averaged such that that the spatial resolution of the predictions and experiments are approximately equal.
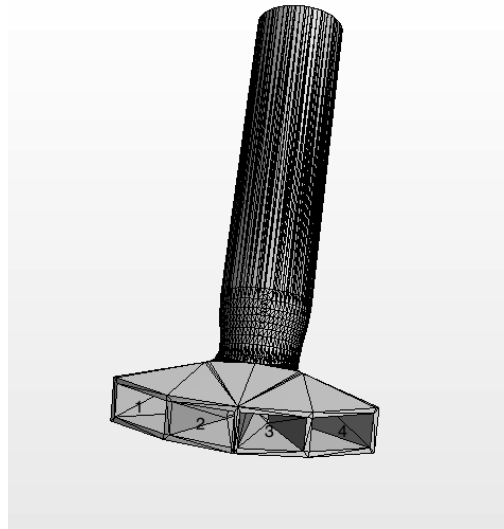
Figure 19. Nozzle geometry

7.1. Face 2 results

The CFD predictions were averaged using MATLAB, code for colourmap by Day

(2013), over special resolution similar to that of PIV so that both could be presented

in a similar format some of the figures have columns of vectors removed for ease

of viewing. A block was added on each figure to demonstrate the location of the

nozzle outlet. Figure 20 and Figure 21 show the vertical middle planes for the CFD

and PIV respectively, **however due to issues in the PIV plotting software the**

vector sizes are not scaled correctly. The color and direction of the PIV plots are

correct.

The simulation and experiments shows that there is a region of higher velocity at

the top of the nozzle with lower velocities towards the bottom. In the case of CFD

there is some recirculation flows while the PIV measurements show forward flow

at all elevations. The CFD shows a strong downwards component while the PIV

results at this plane are more uniform and with more aligned in the pure horizontal

direction. The CFD results generally have higher peak velocities than those of the

PIV measurements while exhibiting recirculation flows in the lower portion of the

nozzle while the laser measurements do not indicate that the flow is recirculating at

any point. This indicates that the CFD predictions are less diffusive then the

measured values since the PIV results are more uniform and unidirectional within

the jet region.
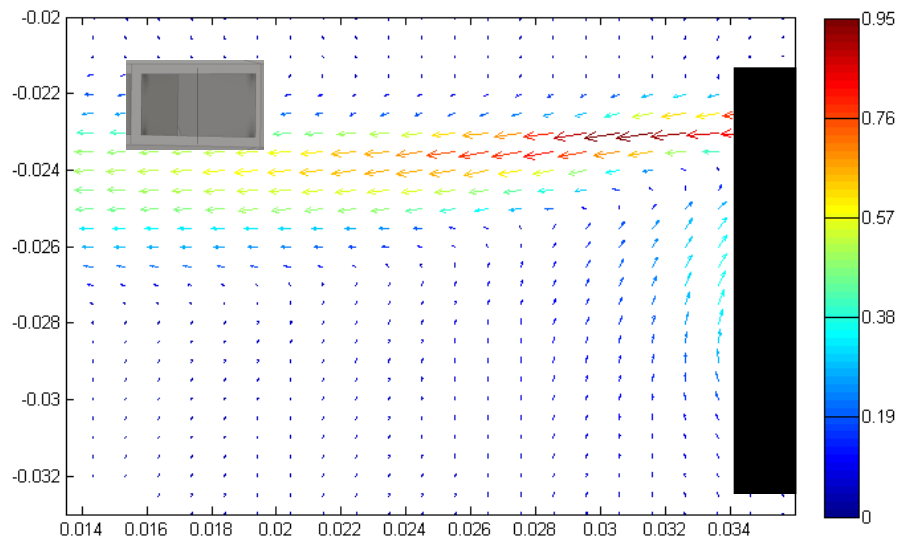
Figure 20. Face 2 mid vertical CFD
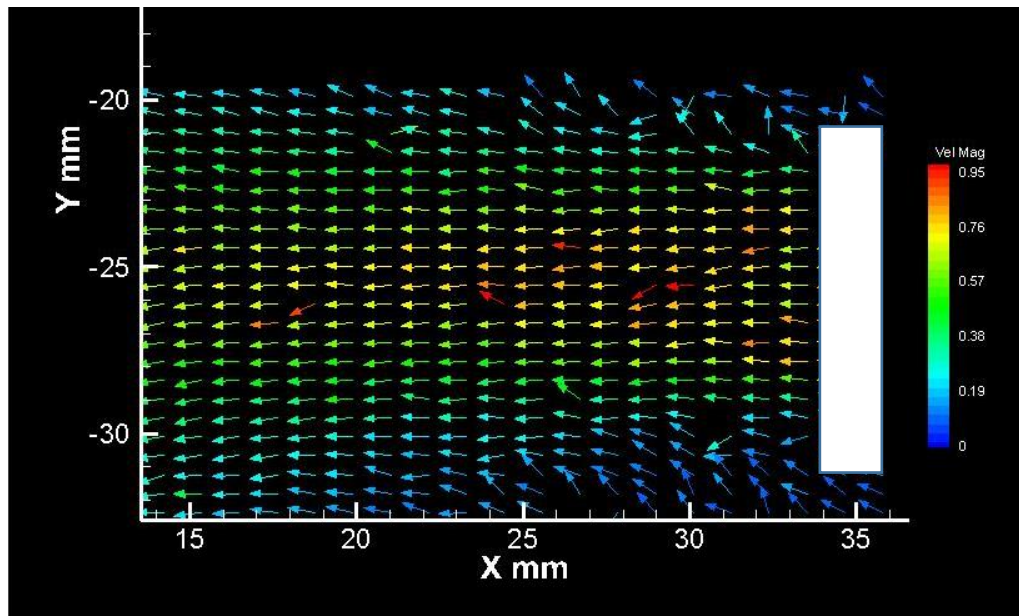
Figure 21. Face 2 vertical middle plane PIV

Examining the other faces in Figure 22 and Figure 23 we observe consistently downwards pointing velocities in both PIV and CFD results, with the CFD simulations showing higher peak velocities and more downward velocity components than the measurements. The jet width is much higher in the measurements than the CFD simulations again indicating that the flow is less diffusive in the computational results. As with the middle plane the CFD shows recirculation at the bottom of the outlet while the PIV indicates that instead there is flow exiting directly out from the nozzle.
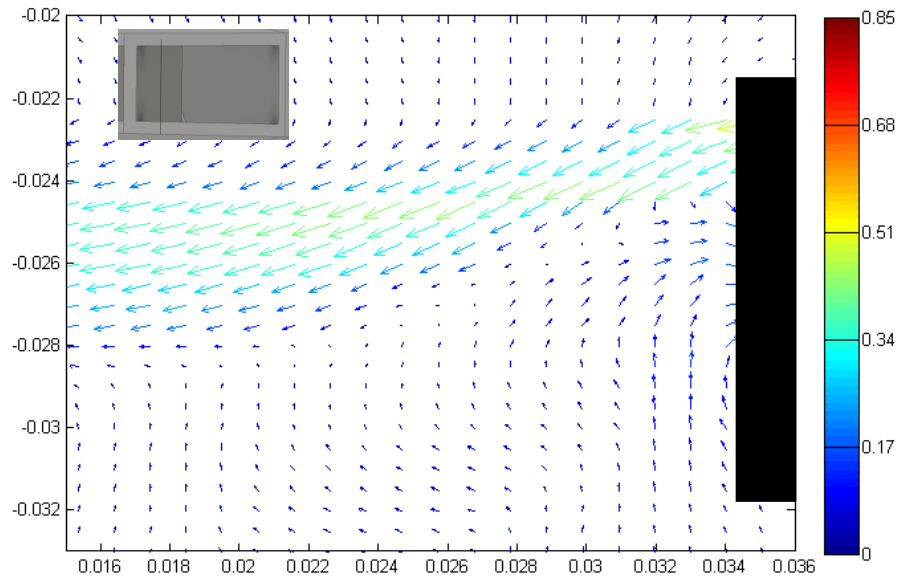
Figure 22. Left vertical plane face 2 CFD
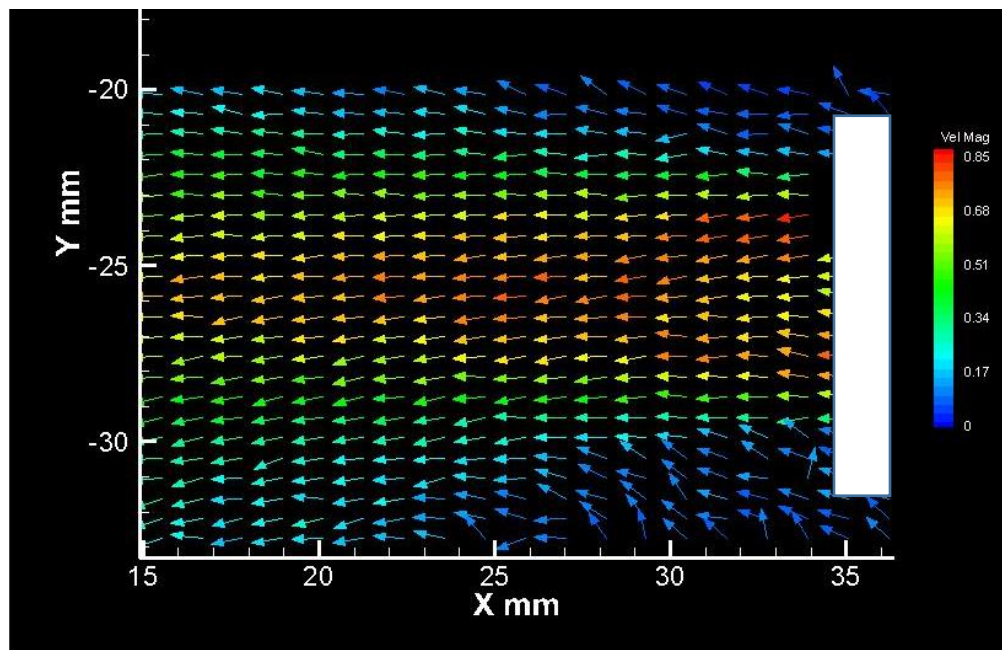
Figure 23. Left vertical plane face 2 PIV

The flow in the third plane 3mm to the right of the central plane on this face show markedly different behavior to the previous two planes. Figure 24 shows the CFD results in this plane has two areas of higher velocity located at the top and bottom of the outlet, with lower velocities in the central region of the outlet. The two high velocity jets converge as the flow moves away from the nozzle creating a more uniform distribution of velocity a few hydraulic diameters downstream of the outlet. Figure 25 shows the PIV measurements taken at the corresponding location and shows a more uniform exit velocity with lower peak magnitudes than the CFD case. Such results provide further evidence that the measured flows are much more diffusive and uniform than those predicted by CFD.
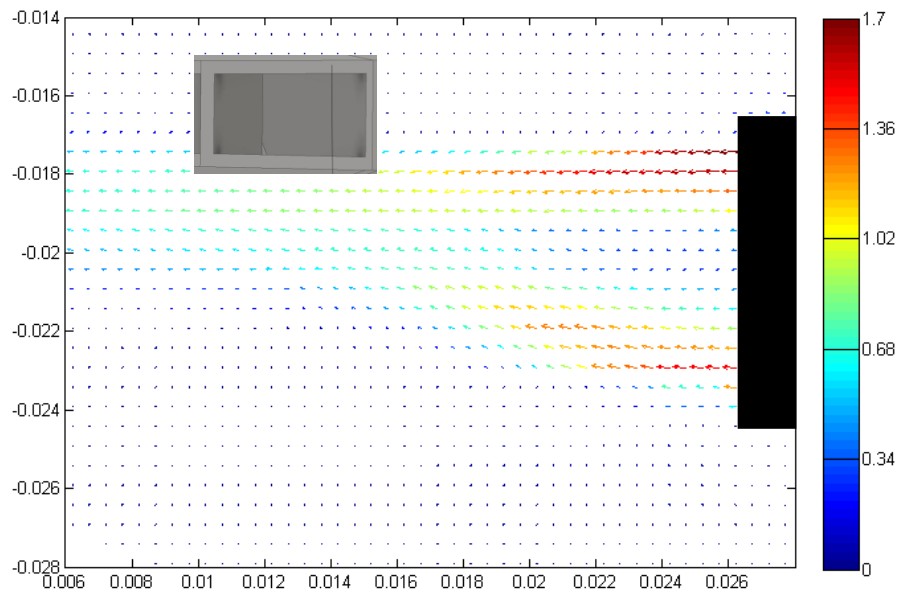
Figure 24. Right vertical plane face 2 CFD
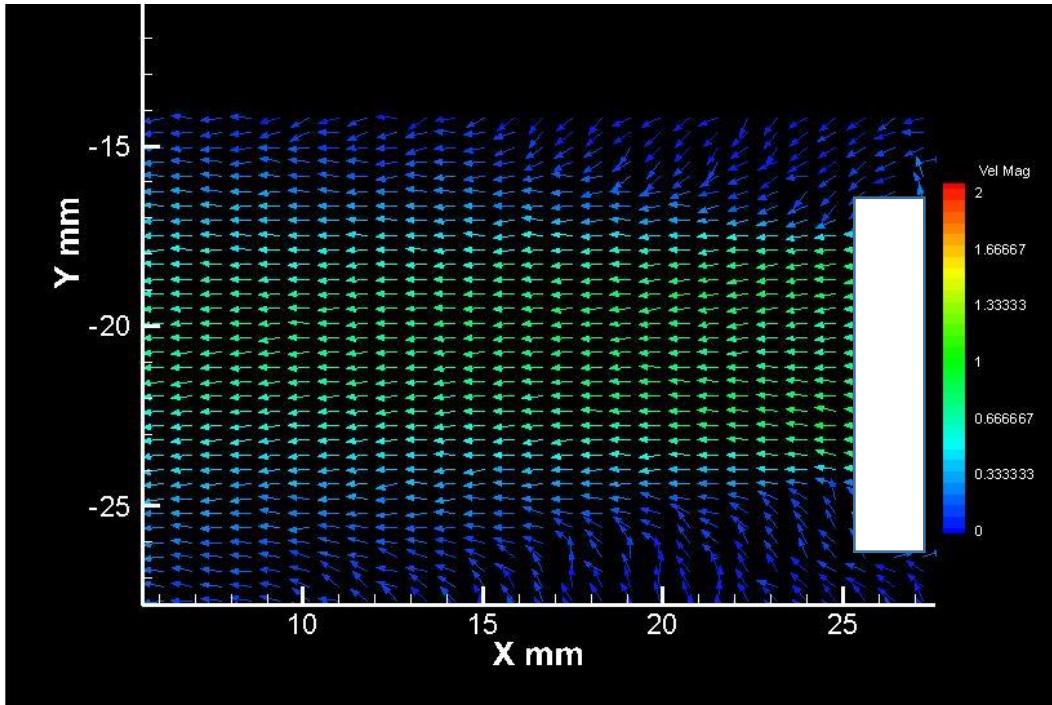
Figure 25. Right vertical plane face 2 PIV

Similar to the vertical planes, three horizontal planes were also measured. The orientation of the figures is such that the top of the graphs corresponds to the middle of the outlet and the bottom corresponds to the edge of the outlet of face 2 (connected to face 1). Due to the proximity of face 1 and 3 and the orientation of the flow exiting those faces we see high velocities immediately adjacent to the face 2 outlet in both the CFD and PIV predictions (i.e., there is some momentum transported from the exit of face 1 into the region of interest on face 2). Figure 26 shows the CFD predictions of the middle horizontal plane on face 2 with higher velocities located at the edge separating face 2 and 3 near the top of the figure. The

rest of the outlet portion has lower exit velocities or are recirculating. The high momentum flows exit the nozzle along the wall between face 2 and 3. At the middle of the outlet, the flow exits straight out of the face while on the edges the flow in general takes the same direction and the solid diverging wall within the fan-nozzle geometry. Figure 27 shows the PIV measurements of the velocity in the horizontal plane located at the midpoint of the nozzle. There is much better qualitative agreement in this regard between the laser measurements and the simulation for this horizontal plane as compared to the vertical planes discussed previously. However quantitatively the peak velocities exiting the nozzle in the CFD simulations are approximately twice larger than those seen in the PIV results. At the top and bottom of the vector fields the flow from the surrounding outlets faces can be seen. The results from the top and bottom planes are presented in the appendix as they were similar to the middle plane discussed here.
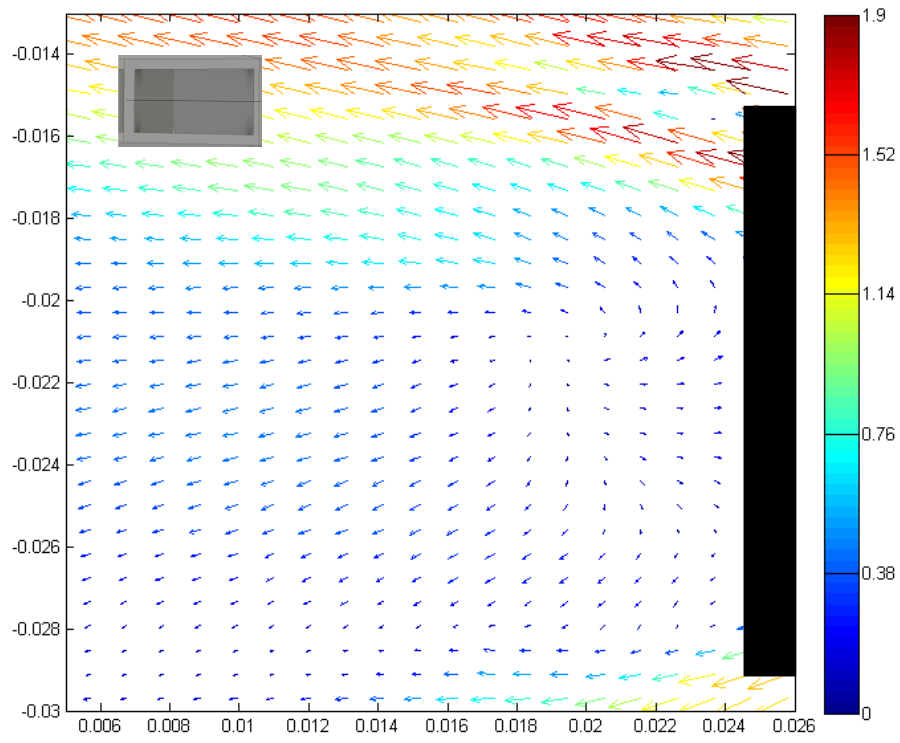
Figure 26. Horizontal middle plane face 2 CFD
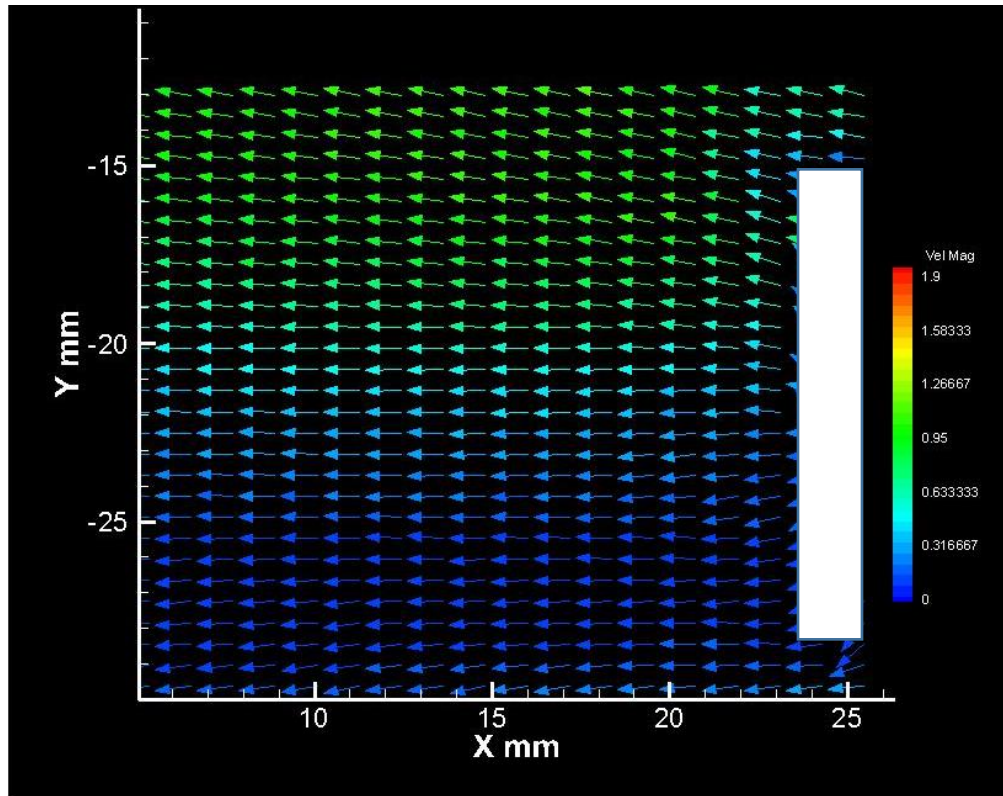
Figure 27. Horizontal middle plane face 2 PIV

Figure 28 shows the CFD of the plane directly parallel with face 2 (showing the velocity components orthogonal to the exit face). There is a vortex on the left side of the outlet face close to the wall. The right side shows transverse velocities pointing towards face 3 and some vortex motion in the upper right corner, with much lower magnitude than the left side vortex. The highest velocities occur on the top of the left vortex and the lowest near the middle of the outlet. Figure 29 shows the PIV measurements of a plane directly in line with the end of the nozzle. The CFD succeeds in qualitative prediction of the measured velocity field as both vortex structures are captured correctly. Consistent with the previous discussion the

T.M.J. Sheasgreen
M.A.Sc. Thesis

Chapter 7
Results And Discussion

McMaster University
Engineering Physics

velocity magnitudes are over predicted by CFD.
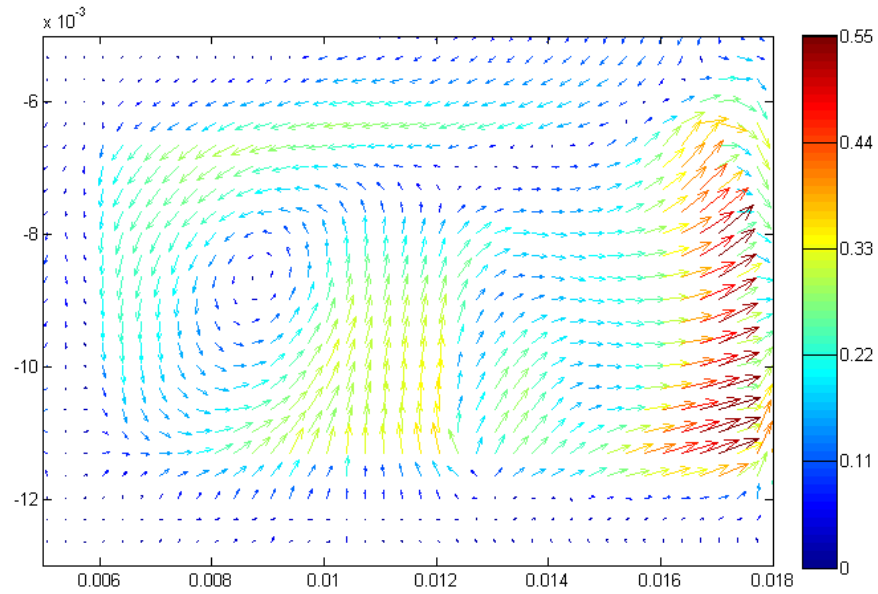
Figure 28. Direct plane face 2 CFD
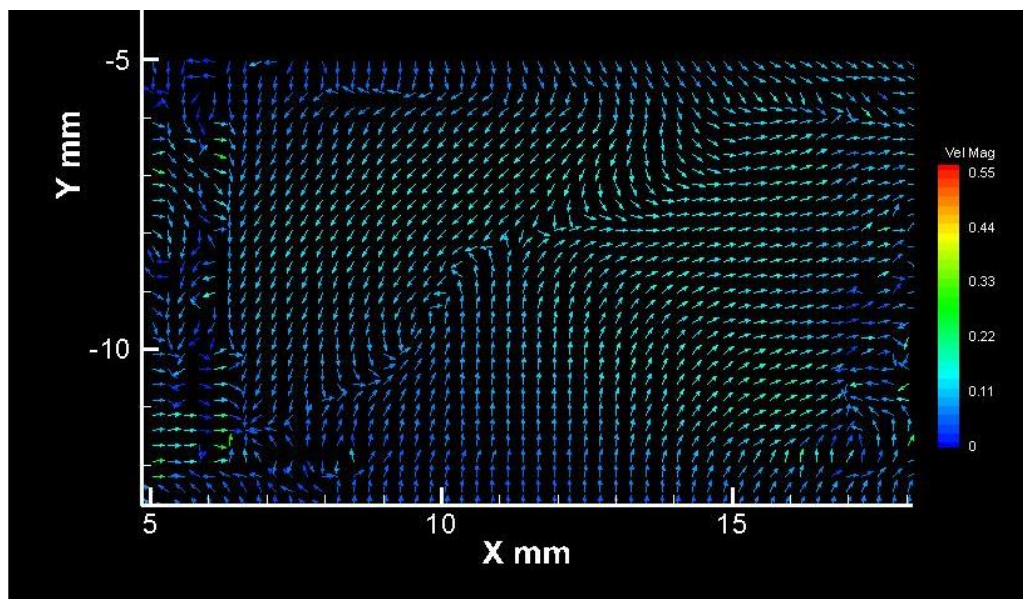
Figure 29. Direct plane face 2 PIV

7.2. Face 1 results

Figure 30 shows the CFD results of the middle plane of face 1 at flow rate of 0.2 kg/s. The simulation shows that there is a region of higher velocity at the bottom portion of the outlet with the rest of the outlet in a zone of recirculation. The high velocity gradient region ends at the midplane with this flow having a slight upward velocity. Figure 31 shows the PIV measurements of the middle vertical plane of face 1 and indicates that the flow is in generally higher at the bottom of the face and lower towards the top with no obvious recirculation region. Both results show higher velocities on the bottom of the outlet with a gradient to lower velocities towards the top. Consistent with the findings for face 2 there are higher peak velocities in the simulation than in the laser measurements indicating that the real flows are more diffusive than the simulations.
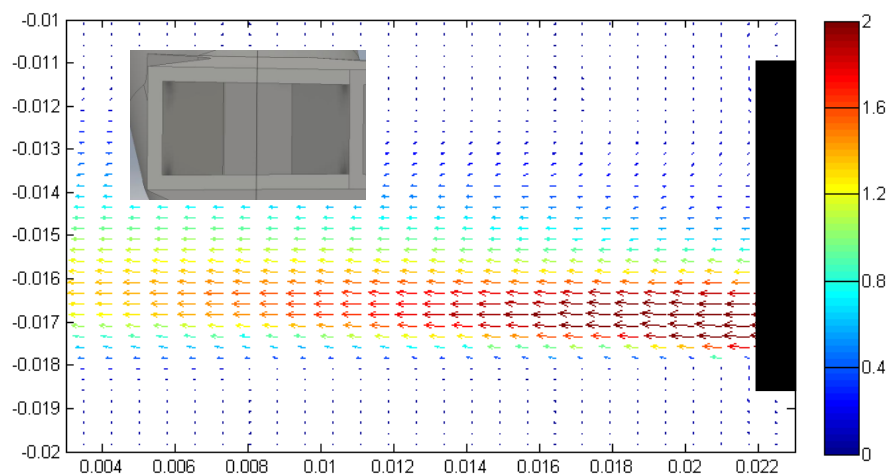
Figure 30. Veritcal middle plane face 1 CFD
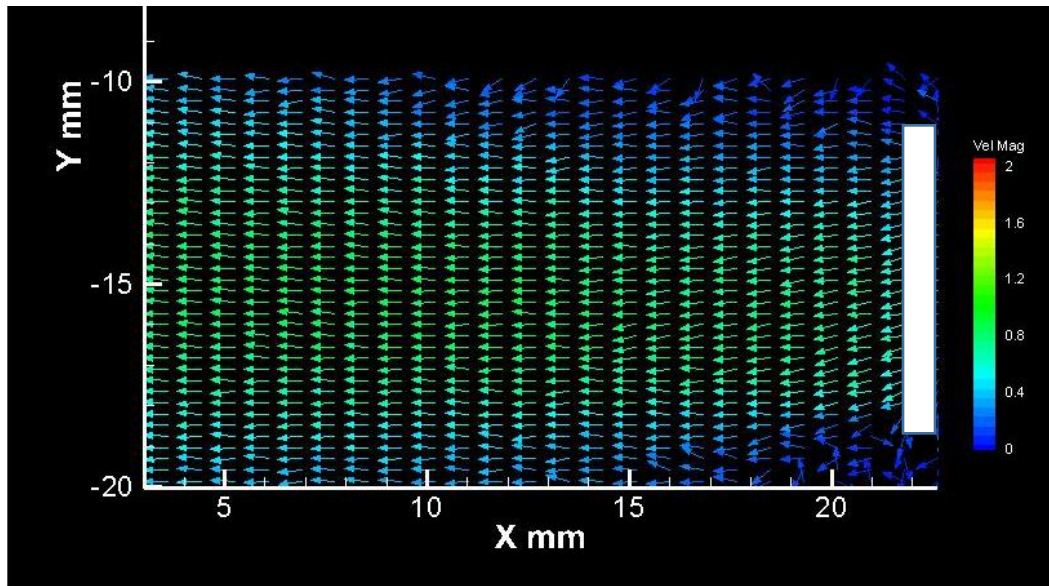
Figure 31. Vertical middle plane face 1 PIV

Figure 32 shows the CFD velocities in the middle horizontal plane on face 1. In general there is a peak velocity in the simulations near the top of the nozzle with lower velocities towards the bottom. However just downstream of the nozzle exit there is another region of high velocity in the CFD simulations, and in fact subsequent inspection shows this secondary peak is generated from a large momentum flows at the bottom of the nozzle but coming from a position outside this plane (i.e., there is in fact two velocity peaks in the CFD results, one at the top in this plane and a second at the bottom in a plane a short distance from the one shown here).

Figure 33 shows the PIV measurements in the middle horizontal plane on face 1. The results show two high momentum regions at the top and bottom of the nozzle

with a lower velocity region in the middle. Hence there is qualitatively good

agreement in the flow field, CFD showing two velocity peaks slightly out of plane

(i.e., by examining mesh locations in proximity to this plane) while PIV shows both

peaks within this plane. CFD in general under predicts the velocities at all locations

on this face however the gradients are larger again indicating that the flow is less

diffusive than the measurements. The vertical planes to the left and right of the

middle are presented in the appendix as they had similar results.
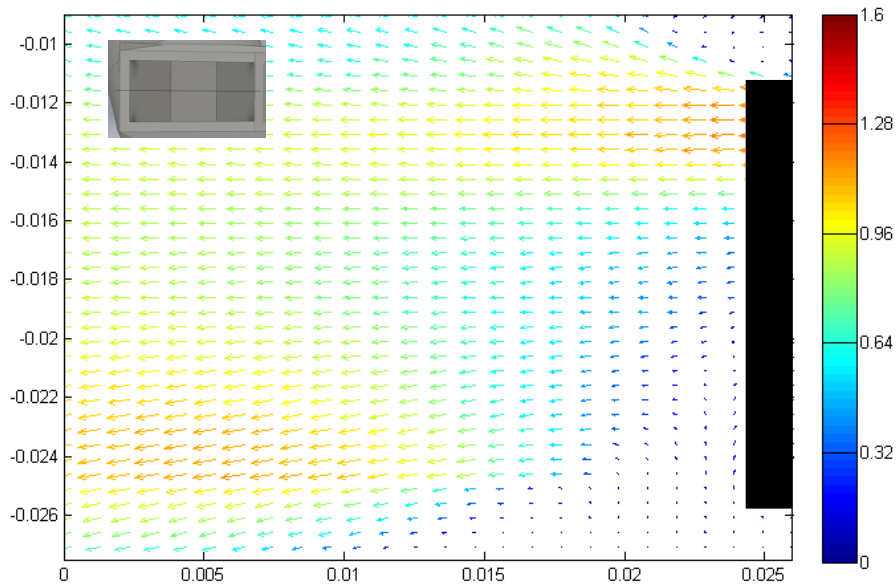
Figure 32. Horizontal middle plane face 1 CFD
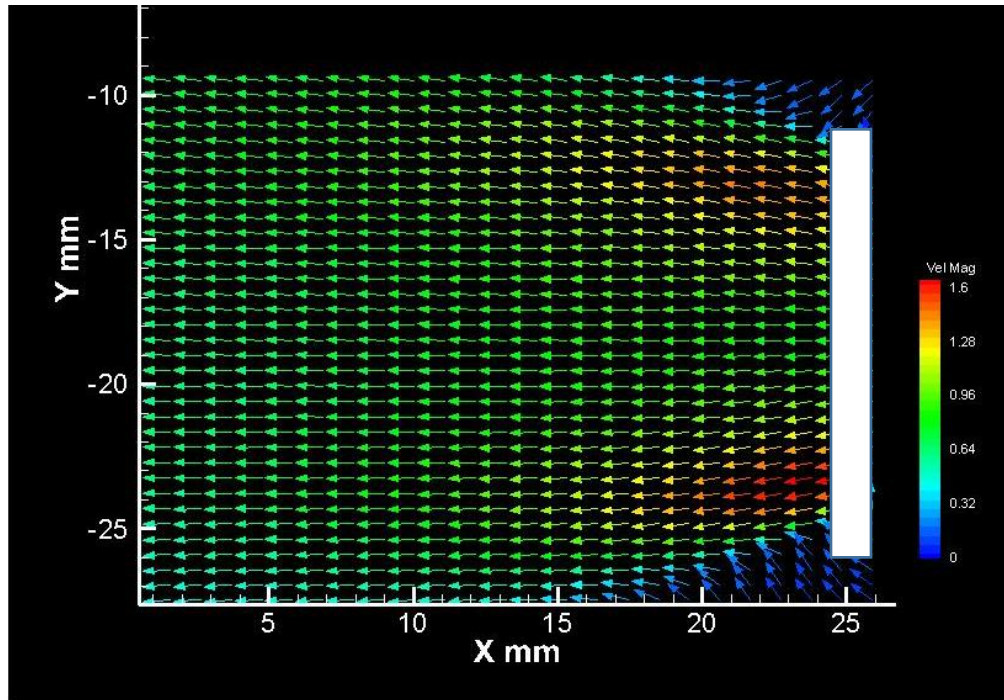
Figure 33. Horizontal middle plane face 1 PIV

Figure 34 shows the CFD results of the top horizontal plane 2 mm above the mid-plane of the nozzle with the orientation such that the top of the figure indicates the right side of the face. The results show the momentum is concentrated on the right side of the face with recirculating flow on the left side. Figure 35 shows the measured velocity field at the same elevation. Similar to the discussion above, the PIV shows two peaks within this measurement plane while CFD shows a single peak along the right wall. However, upon inspection of the CFD results we see a second peak a short distance away from the nozzle which is coming from a region of high momentum on the left edge which is just out of the CFD plane shown in Figure 34. Hence, this results in this plane qualitatively agree on both PIV and CFD,

with both showing higher velocities near the sides of the outlet and lower velocities near the middle albeit the CFD results predict the peak on the left edge at a slightly different elevation. Consistent with the vertical planes, the PIV measured flows tend to be higher on this face than the CFD predictions.
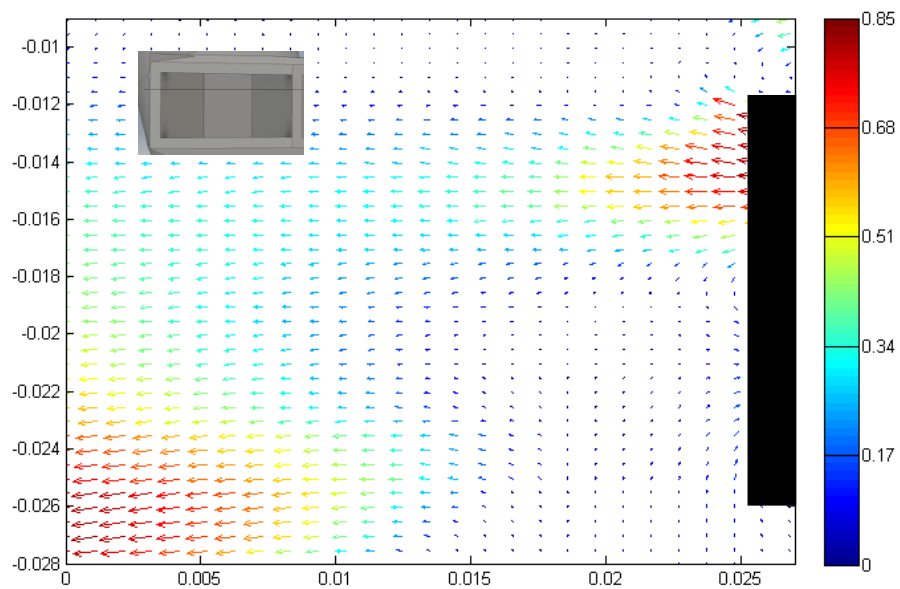
Figure 34. Horizontal top plane face 1 CFD
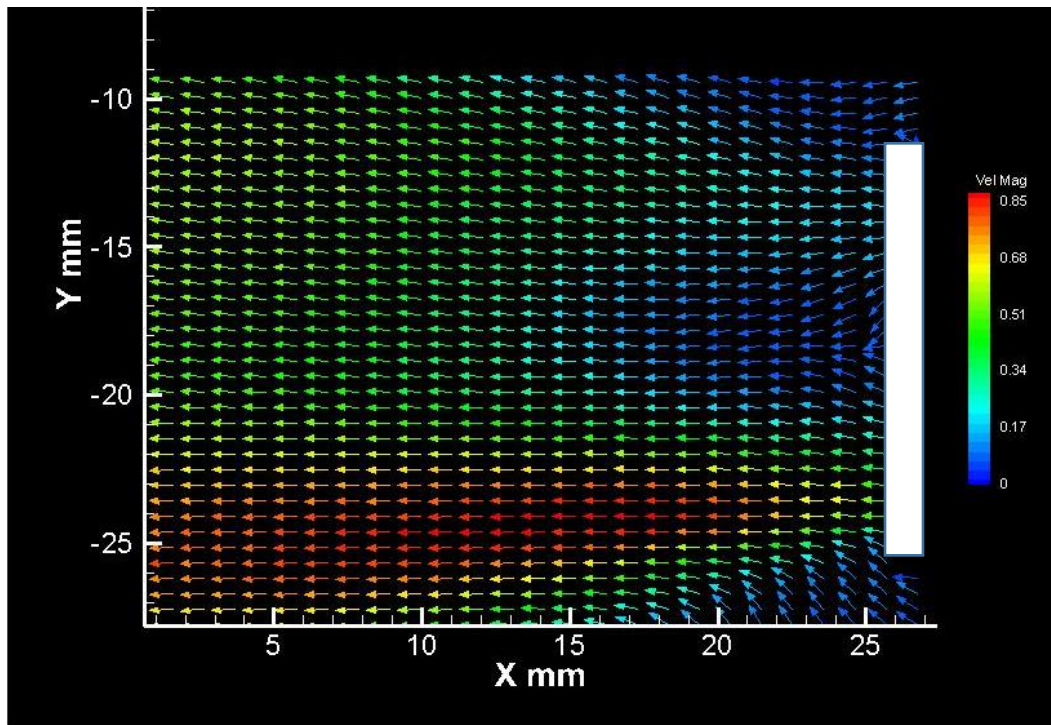
Figure 35. Horizontal top plane face 1 PIV

Figure 36 shows the CFD for the bottom horizontal plane located 2 mm below the

midplane off the nozzle. The flow out of the outlet closely follows the angles of the

two side walls. Figure 37 shows the PIV bottom horizontal plane for face 1. The

CFD and PIV results both show somewhat uniform velocities at this elevation.
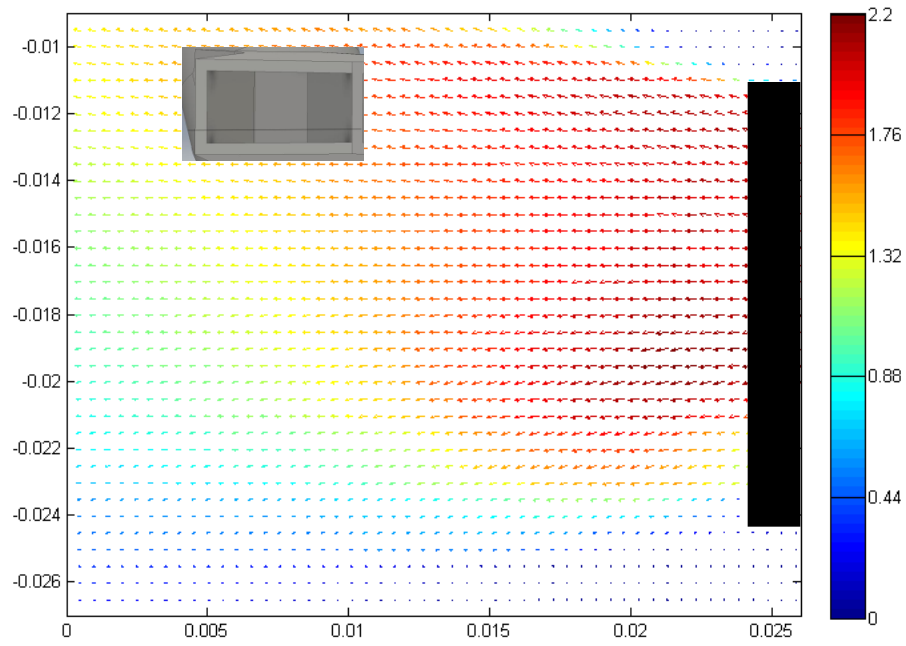
Figure 36. Horizontal bottom plane face 1 CFD
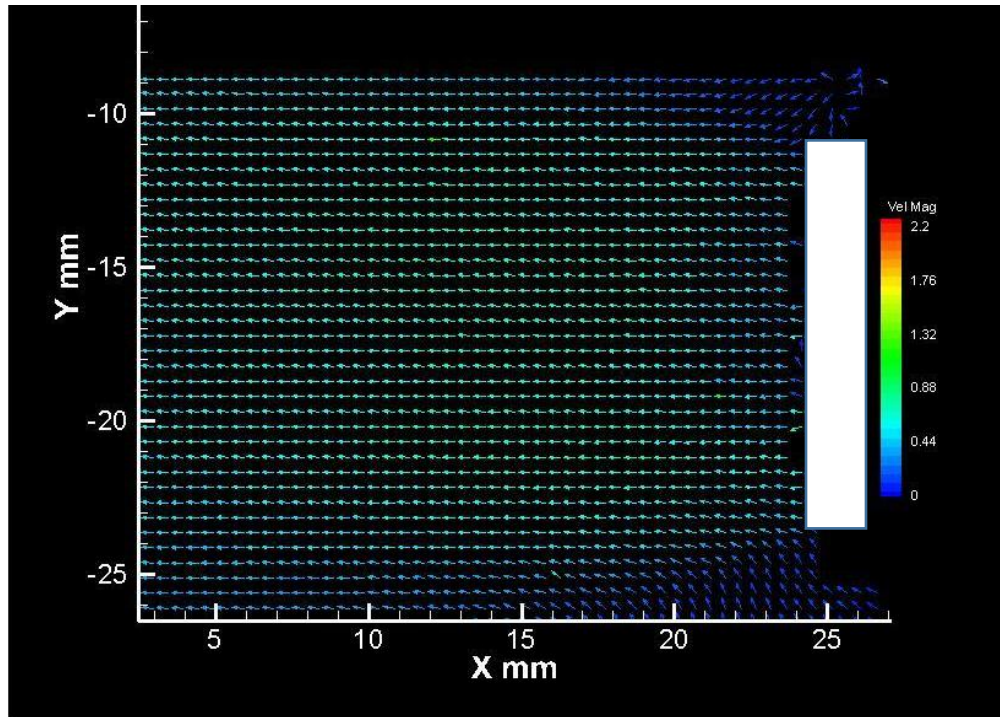
Figure 37. Horizontal bottom plane face 1 PIV

Figure 38 shows the CFD of the velocity field orthogonal to the face 1 outlet. There

is a strong vortex formed on the left side of the outlet with the maximum velocities

reaching 25-30% of the axial flow component. CFD also shows a strong outwards

flow on the right side of the figures. Towards the bottom of the outlet on either side

there is a change in the velocities as the flow moves outwards from both sides. In

the region of near-zero velocity the simulation convergence characteristics were

poor in the steady-state RANS models suggesting flow instabilities. Figure 39

shows similar vortex structure in the PIV measurements and at a similar location

albeit with slight lower and more uniform velocity magnitudes. Both CFD and PIV

results also show significant outwards velocities at the right hand side of the face

and with comparable magnitudes.
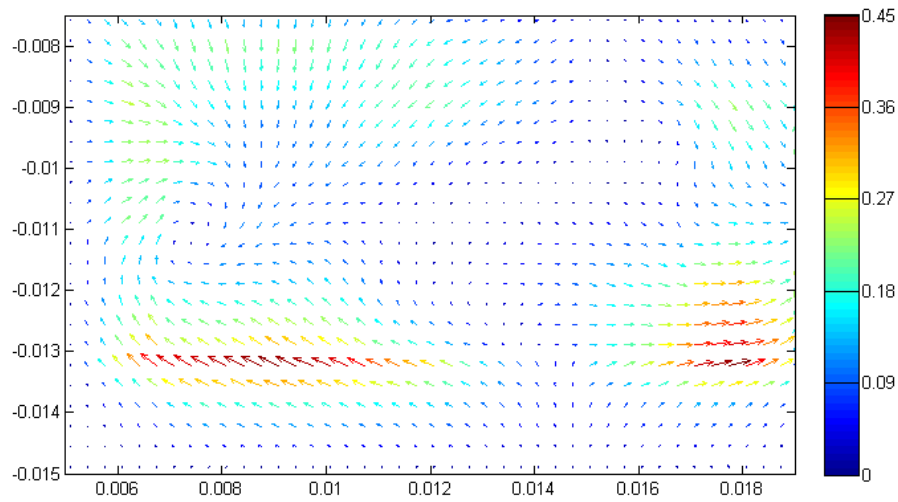
Figure 38. Direct plane face 1 CFD
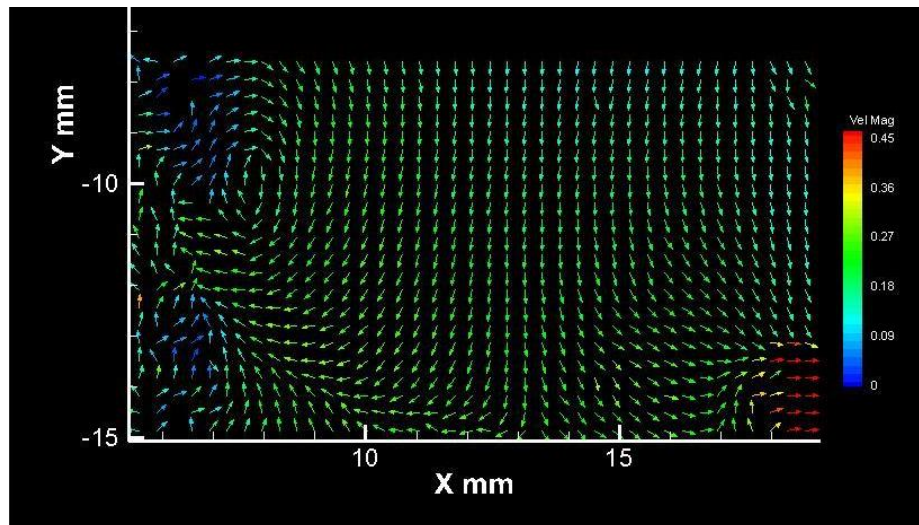
Figure 39. Direct plane face 1 PIV

Contour plots were created using both measured and calculated velocity magnitude results. Figure 40 and Figure 41 show the contour plots for the top horizontal plane on face 2. The velocity contours can be used for qualitative comparison between the measured and the predicted velocity fields.
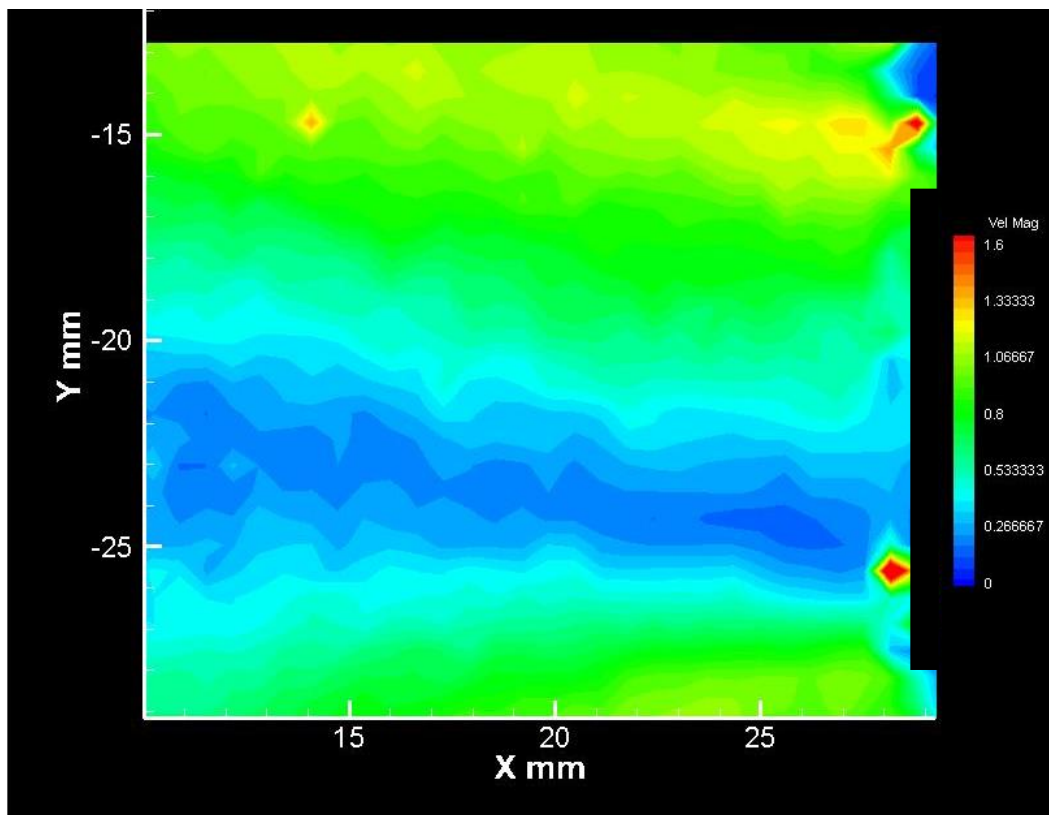
Figure 40: Contour face 2 top horizontal PIV
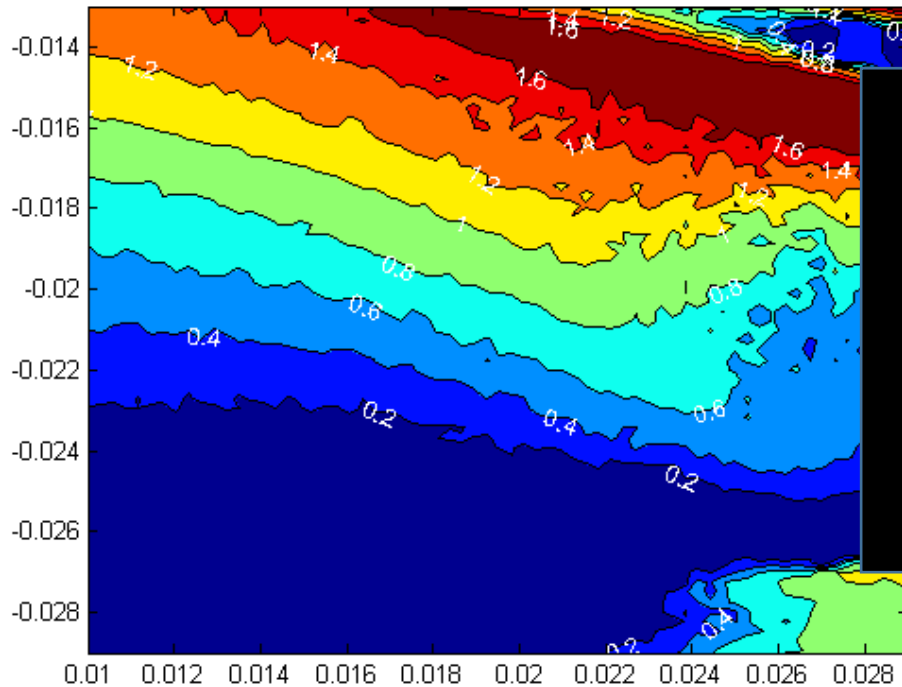
Figure 41: Contour face 2 top horizontal CFD

7.3. K-epsilon predictions

The results obtained with k-ω SST model were compared to those using k-ε simulation. Similar results were obtained using both models on face 2. On the other hand, appreciable discrepancy was seen for the velocity fields on face 1.

Figure 42 shows the velocity vectors at the middle horizontal plane on face 1. The k-ε model predictions show that there is an area of higher velocities near one of the outlet walls compared to those obtained with k-ω SST model which show two

separate areas of relatively higher velocity. It can be seen that the peak velocities

are comparable between the two predictions. However, the higher velocities in the

k-ε simulations are grouped together in a larger area.
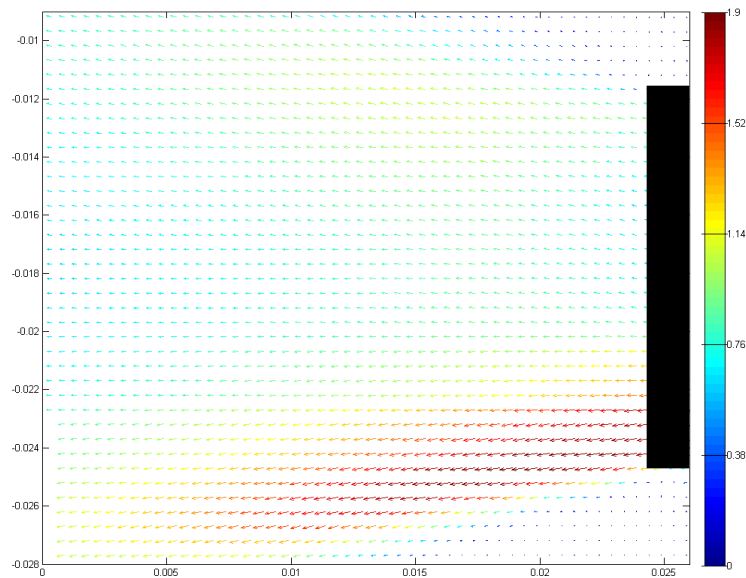
Figure 42: K-ε face 1 horizontal middle plane
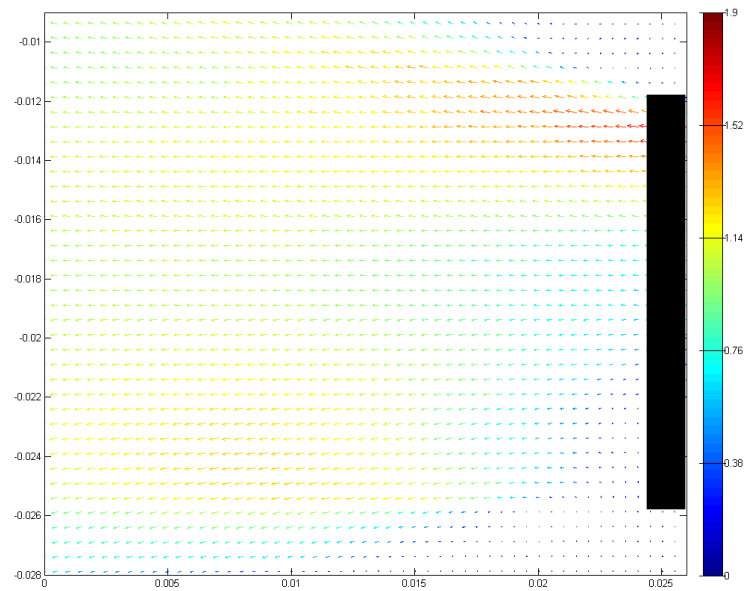
Figure 43: K-ω sst face 1 horizontal

Figure 44 shows the top horizontal plane on face 1. Here, like in the results presented in Figures 42 and 43, the k-ε simulation shows higher peak velocities - the jets of higher velocities are located near the edges of the graph and are not fully captured.
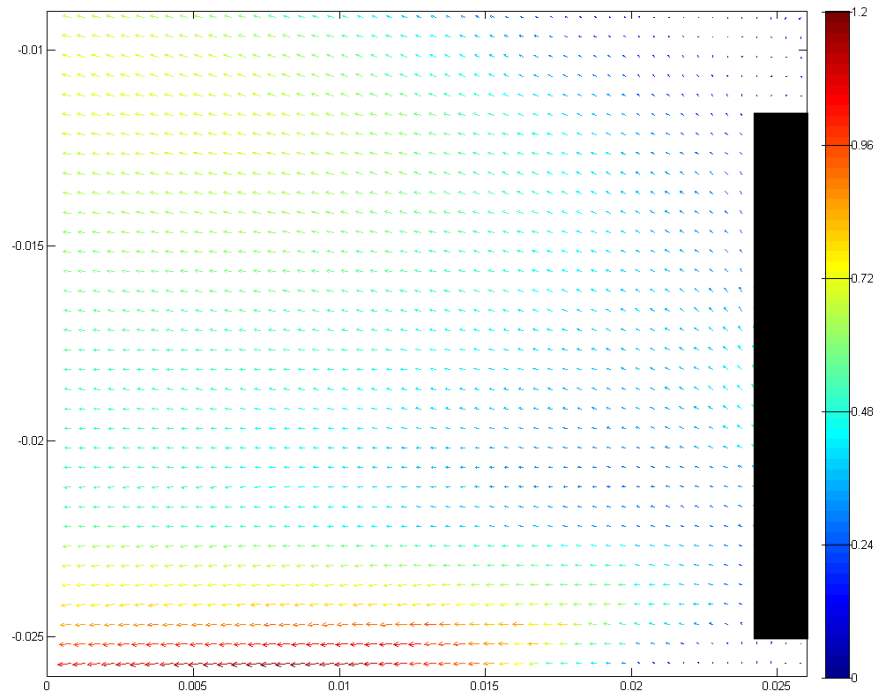
Figure 44: K-ε face 1 top horizontal plane
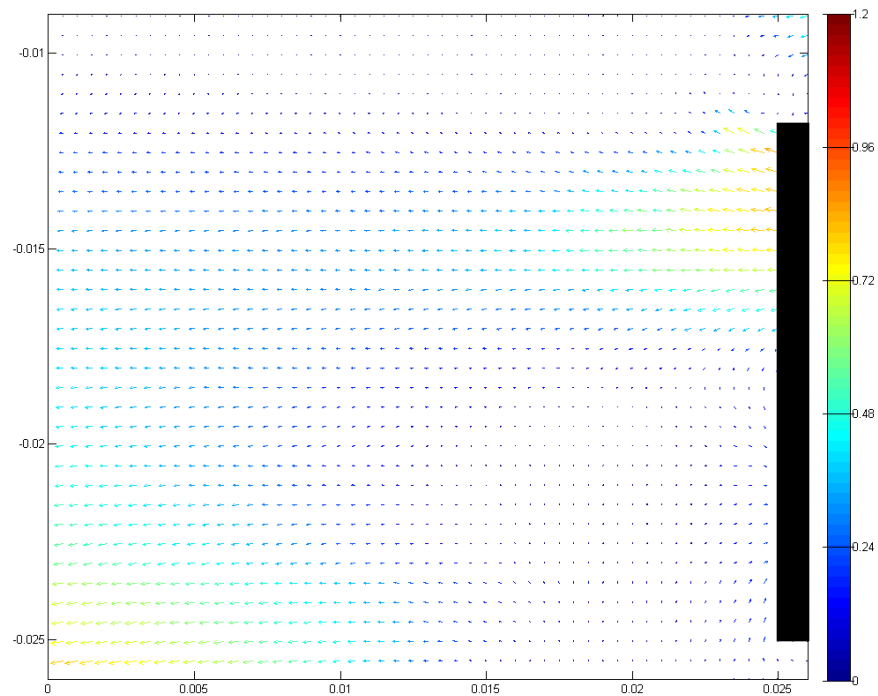
Figure 45: K-ω sst face 1 horizontal top

Figure 46 and 47 show velocity vector fields for the bottom horizontal plane on face 1 as predicted with k-ε and k-ω SST models respectively. Consistently with the above presented velocity vector fields for face 1 planes, the high velocity region is larger for the k- ω SST model.
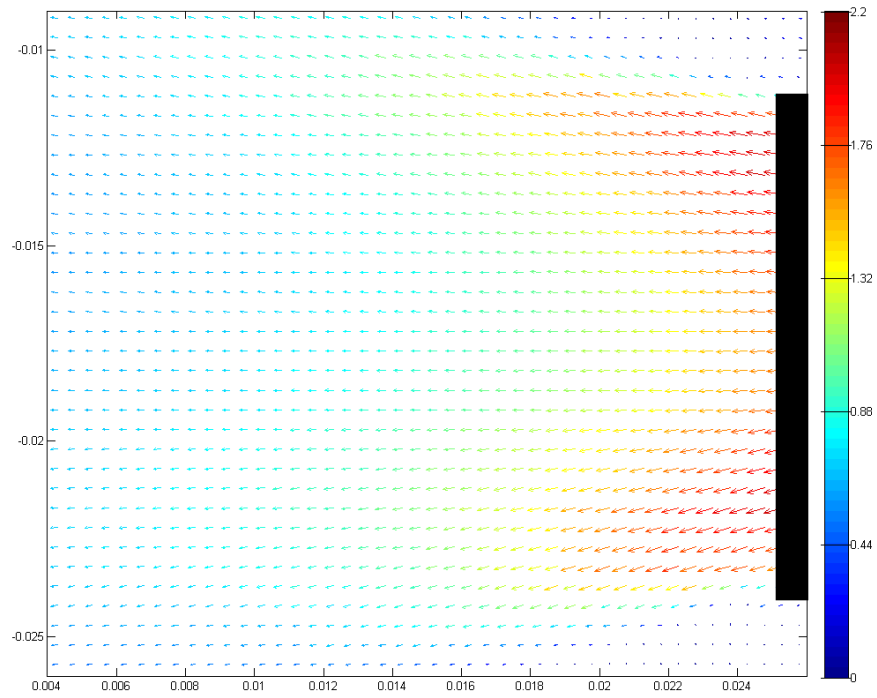
Figure 46: K-ε face 1 bottom horizontal
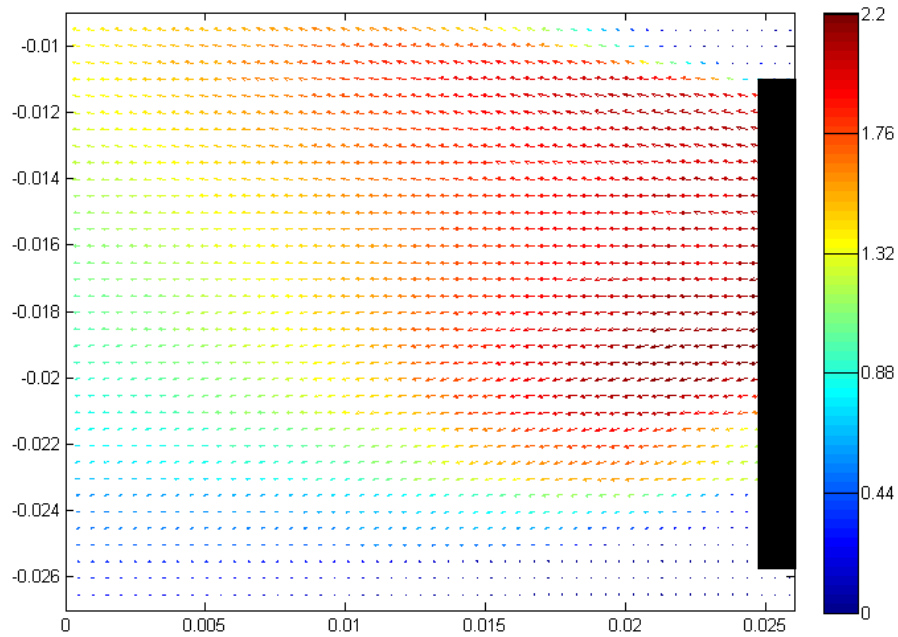
Figure 47: K-ω sst face 1 horizontal bottom

Figure 48 and 49 show velocity vector fields for the middle vertical plane on face 1 as predicted with k-ε and k-ω SST models respectively. The same quantitative observation, as those for the results presented above, can be made for the velocity magnitudes as predicted with the two models in question: the velocities obtained with k-ε model are lower than those predicted with k-ω SST**.**
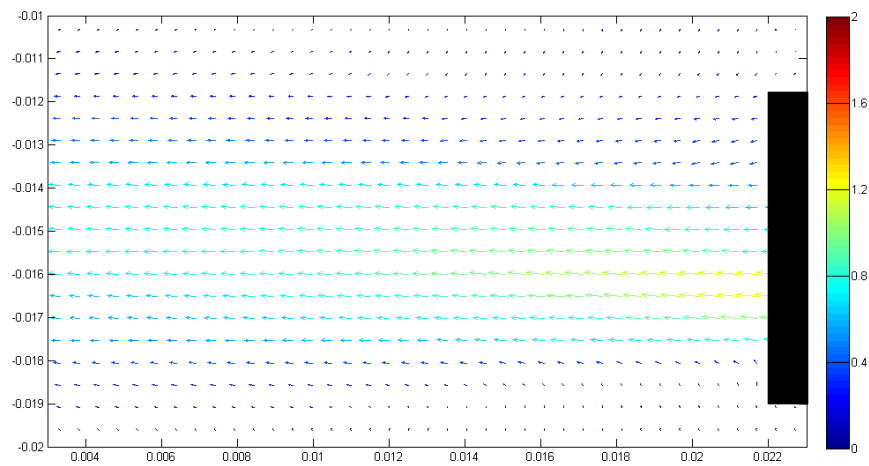
Figure 48: K-ε face 1 middle vertical plane
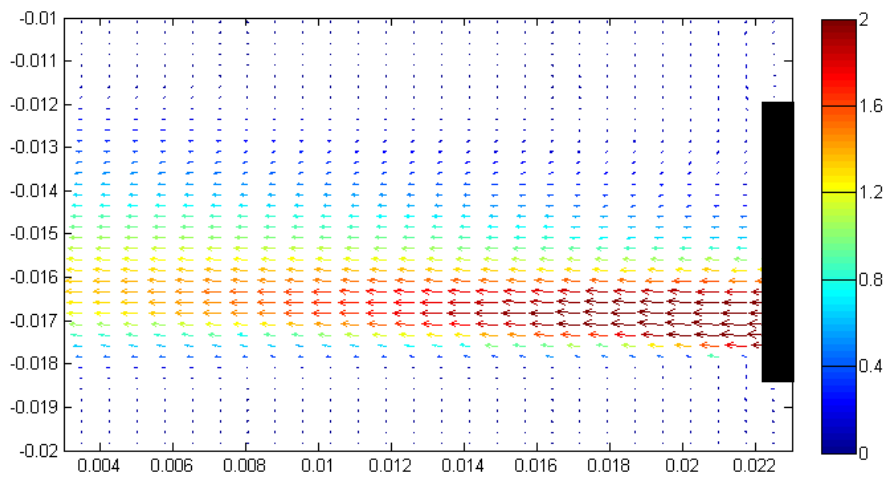
Figure 49: K-ω sst face 1 middle vertical

It can be concluded that predictions obtained with k-ε model were generally in worth agreement with experimentally obtained velocity fields, than those obtained using k-ω SST model.

7.4. Simulation convergence

In order to allow for the simulation to converge the results shown above were obtained using a transient model with a time step of 0.001s and 20 iterations per time step. An example of the dependency is shown in Figure 50 and Figure 52 for the TKE at a point probe on face 2 and face 1, respectively. Figure 51 and Figure 53 show the location of the probe in the outlet of face 2 and face 1 respectively. During the simulation over time the TKE values converge to steady values on each outlet, although on face 1 some variations are still observed even after ~500s of transient simulation. Based on the TKE variability at this location it is unlikely that steady-state residuals would be low enough for a normal steady simulation to be judged as converged, however the degree of variability is small. Based on the asymptotic behaviour of the scalers such as TKE in the transient simulations the CFD results at the end of the transient simulations were selected as being representative of the solutions. Figure 54 shows the typical conservation equations residuals behavior during these simulations.
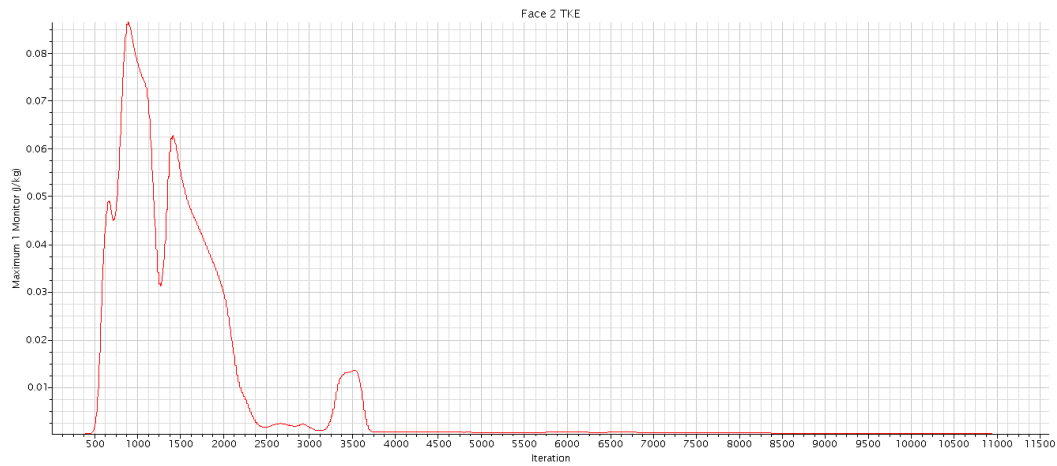
Figure 50. Turbulent kinetic energy at a point throughout simulation
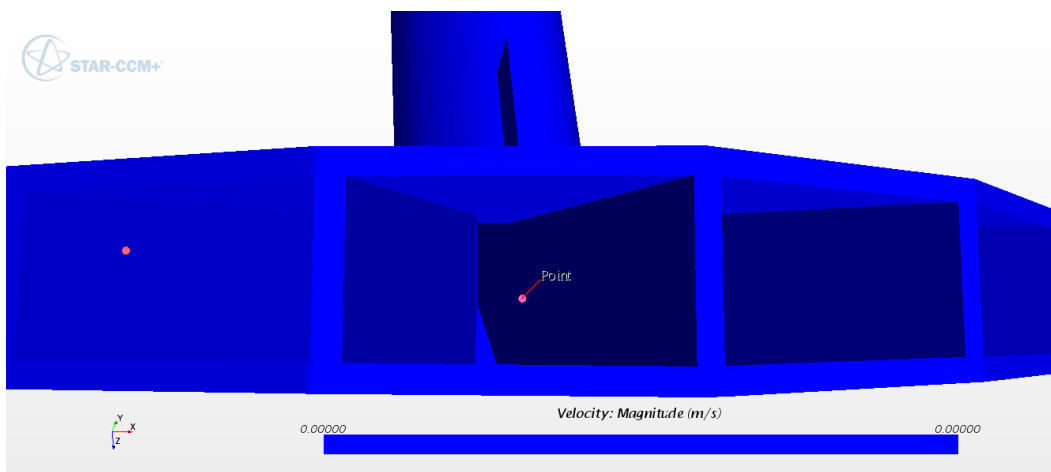
Figure 51. Position of probe on face 2

`
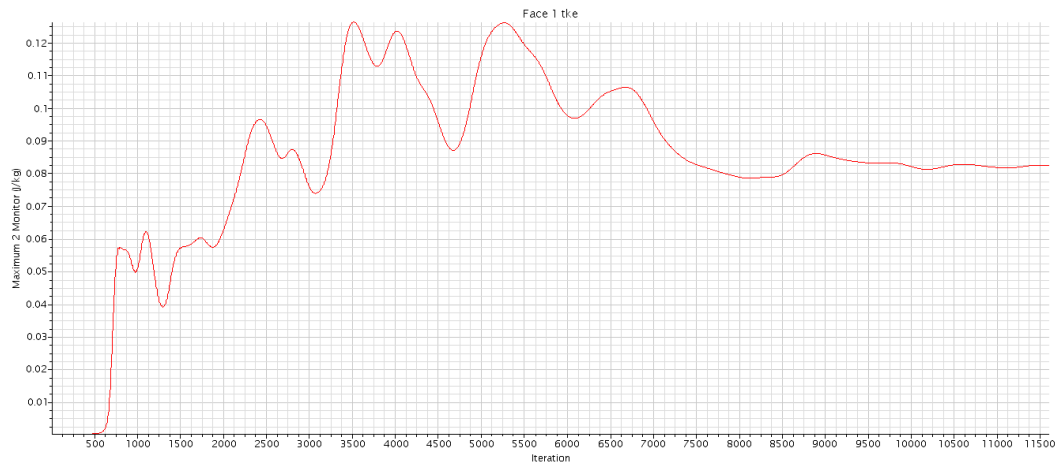
Figure 52. Turbulent kinetic energy during iterations
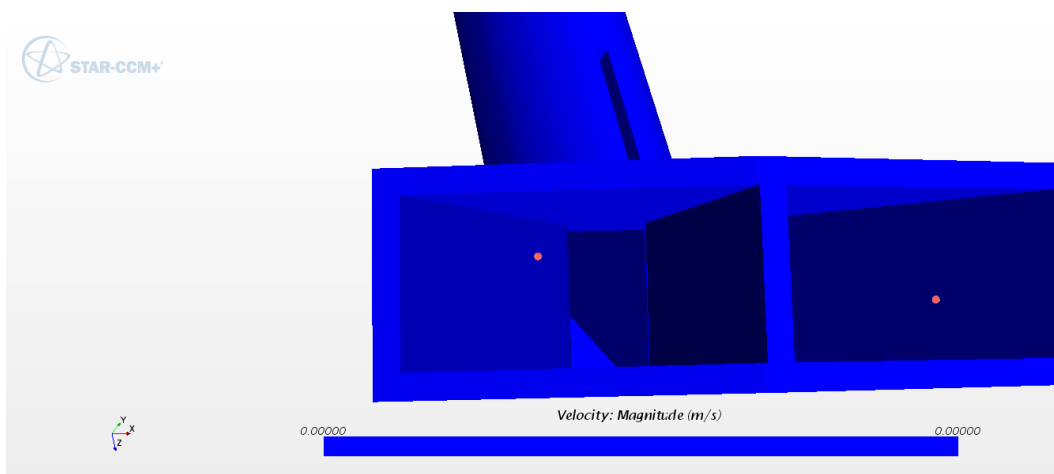
Figure 53. Location of probe on face 1
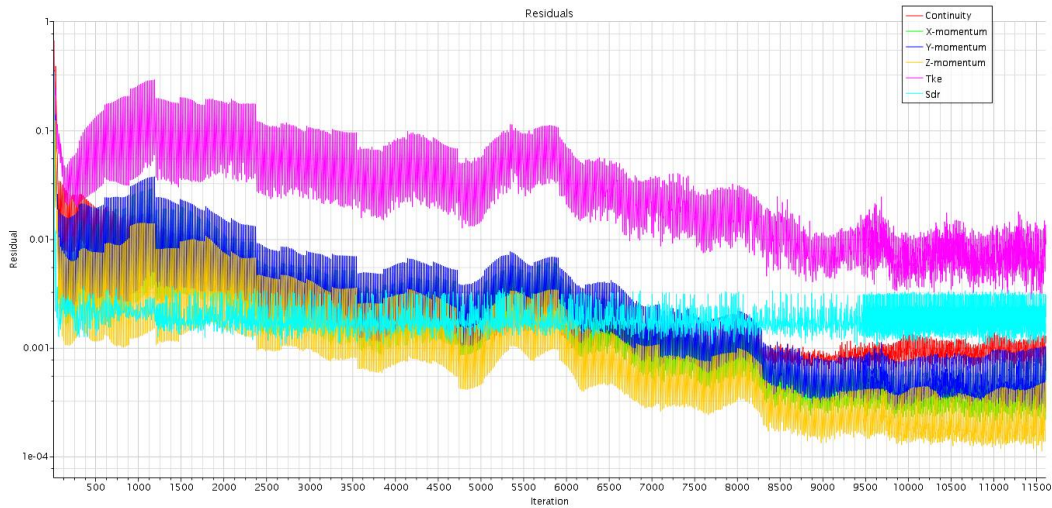
Figure 54. k-ω SST Simulation residuals

The k-ε simulations using the same mesh and a steady state model resulted in better convergence than the k-ω model simulation (see Figure 55), therefore a transient simulation was deemed unnecessary for the former. Similar to the steady state simulation of the k-ω model the k-ε model TKE residuals are higher than the others. Although these were overall significantly lower than the previous simulation so it was assumed to be converged.
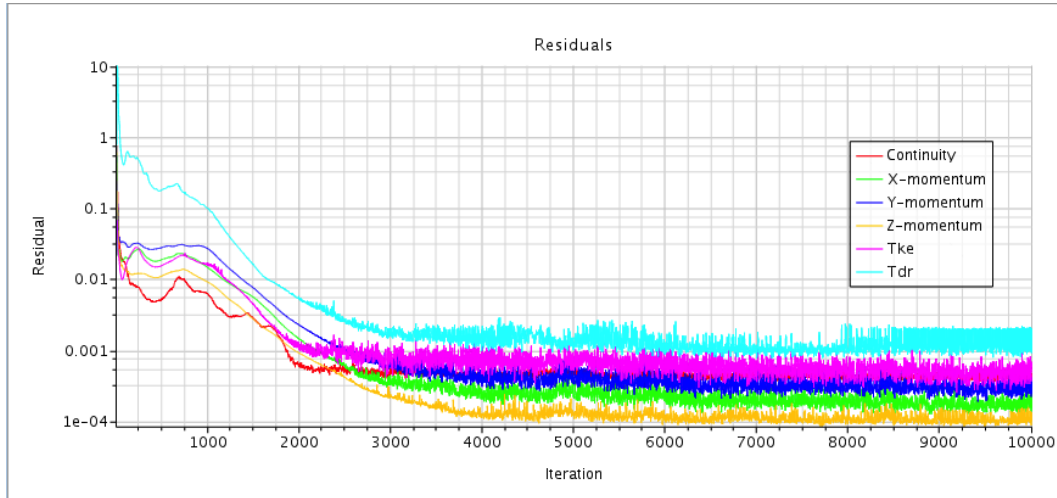
Figure 55: k-ε residuals

7.5. PIV to CFD discrepancies

The measured peak velocity magnitude and velocity gradients were generally lower

than the CFD results for almost all the planes and flow conditions considered in the

present study. Though the k-ω SST turbulence model was shown to be able to

replicate quantitatively the velocity fields at the outlet of the nozzle, it showed much

higher velocity gradients as compared to experiment. Any separation areas within

the nozzle may change the behavior of the outlet flow while rendering the inlet flow

to be less impactful. Discrepancies between physical results and simulation

predictions can have significant impact on the flow out of the nozzle which could

create some changes.

In addition to the turbulence model approximations, several factors can contribute

to the differences seen in the CFD and PIV results. Planes defined in the CFD

simulation for comparison with PIV obtained velocity fields have near zero

thickness (i.e., velocities are representative of the small volumes used in the mesh).

The PIV measurements are actually averaged through the laser thickness being of

finite size. Hence the PIV measurement will be a combination of the particles

velocities over the thickness of the laser sheet, and treating them as if they were all

located within an infinitely thin plane would be inaccurate. Depending on the

velocity gradients this may have an appreciable effect on the measured velocities.

For example, in the horizontal planes a 1-mm laser thickness will cover a significant

portion of the outlet area. Looking at the middle horizontal plane on face 1 if the

laser extended from -20 mm to -18 mm the velocities at the outlet will vary from 1

m/s to 0.7 m/s making an average of 0.85 m/s compared to 0.9 m/s in the results.

The orientation of the laser sheet could also affect the measurements captured by

the systems in that small angular deviations of the laser sheet will cause a two fold

problem: i) the reported velocities will be along the plane specified by the user but

the actual measurements will fall on the true plane illuminated by the laser, ii) if the

laser sheet was non-orthogonal to the camera the reported velocity magnitudes will

be skewed since the pixel sizes at the bottom and top of the illumined plane will

correspond to different physical sizes. Change in angle may also cause the laser to

be aligned outside of the peak velocities or aligned with a section of lower velocity

outside of the nozzle. The sensitivity to these changes will be discussed in the

following sections.

Additionally the actual locations of the measurement planes may be insufficient to

track the peaks and gradients of the flow. As there is a limited number of planes

and measurement locations, if a velocity peak were to occur in between the locations of the two of the measurement planes then it would not be observed in the measurements. If the velocity profiles in both the physical experiments and simulations were similar but skewed towards a different direction, then the measurement planes may show very different results.

7.5.1. Measurement planes position uncertainty

Sources of uncertainty for the measurements of the velocity in an illuminated plane include.

- Angle of laser sheet with respect to the outlet of the nozzle: less than approximately 5 degrees

- Flow rate uncertainty ($\pm$ 0.5% based on instrument calibration)

- Timing of camera and synchronizer (negligible, error due to outside sources $>$ 0.5ns)

- Location of the laser sheet with respect to nozzle face (X,Y,Z) ($\pm$1.0mm)

- Thickness of laser sheet (up to 1 mm)

- Flowrate uncertainty ($\pm$0.2 l/min)

- Angle of the camera with respect to measurement plane (estimated to be a maximum of 5 degrees)

- Nozzle dimensions ($\pm$ 0.2 mm based on micrometer inspections)

As stated, both measurement plane position and orientation can have an effect of the resulting velocity field obtained using PIV. While changing the orientation of the plane does not have a great effect on the velocities distributions, moving the plane to either side causes an appreciable increase or decrease of the measured velocities owing to the significant gradients in this direction. To assess these sensitivities one could perform new experiments with the camera and laser orientation deviating from normal measurement locations according to the uncertainties listed above. While such tests are recommended for future work, the sensitivities were investigated by examining the sensitivity of CFD results to translations and rotations of the measurement plane, since such post processing can be obtained on a shorter time scale.

Figure 57, Figure 58 and Figure 59 show the results of plane shift of 1 mm to the right of the original position and rotation of 5 degrees around both, X and Y axes. The X axis is directed from the center of the outlet, pointing directly outwards, while the Y axis is aligned vertically with the outlet edge. From these figures it is apparent that the dominant uncertainty is the position of the laser sheet within the high gradient field, and rotation of the laser plane plays only a secondary role in the uncertainty of the reported velocities.
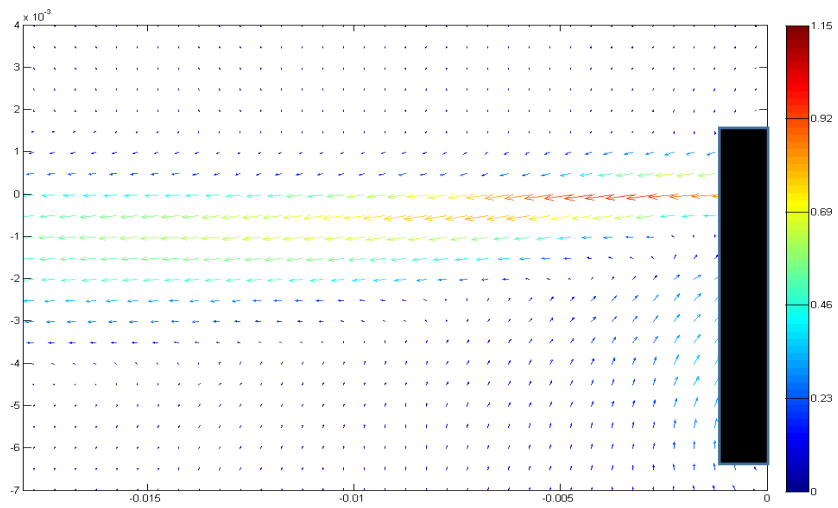
Figure 56: Face 2 middle vertical original position
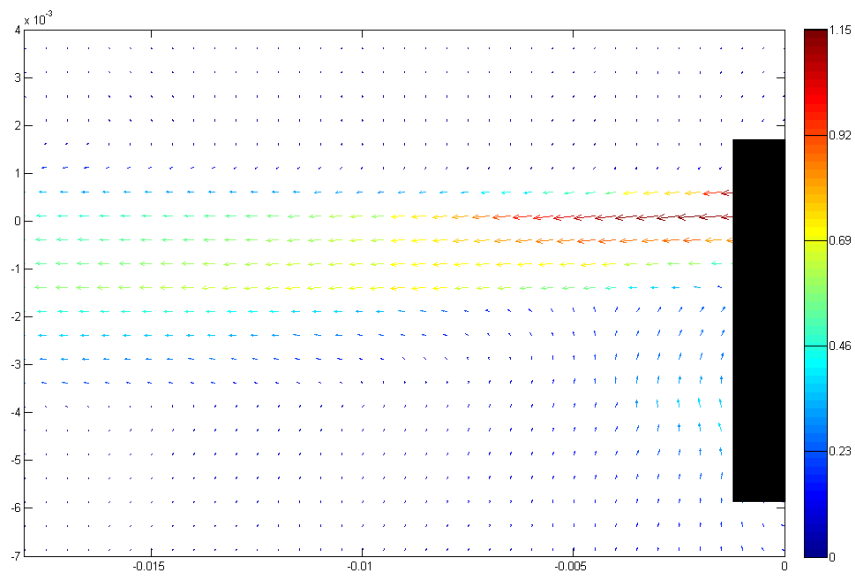
Figure 57. Face 2 middle vertical plane shifted 1mm to right
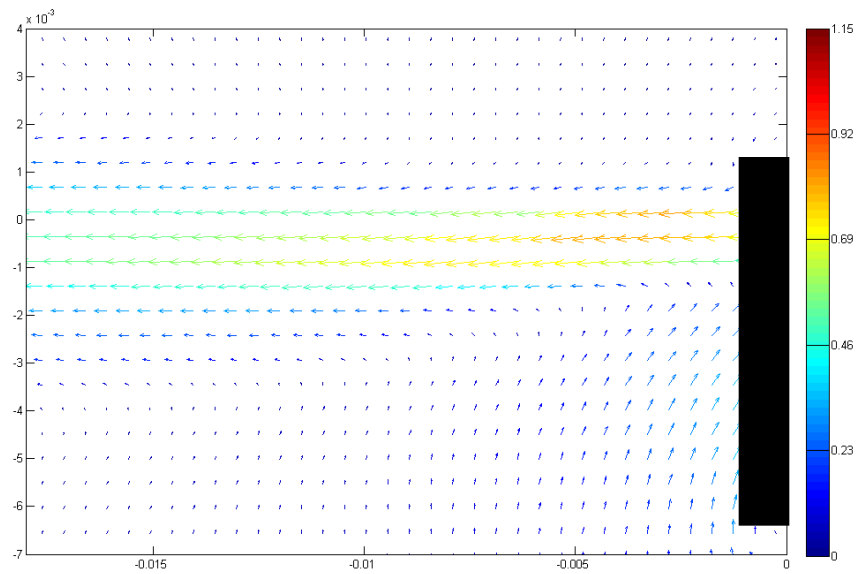
Figure 58. Face 2 middle vertical plane rotated 5º around X axis
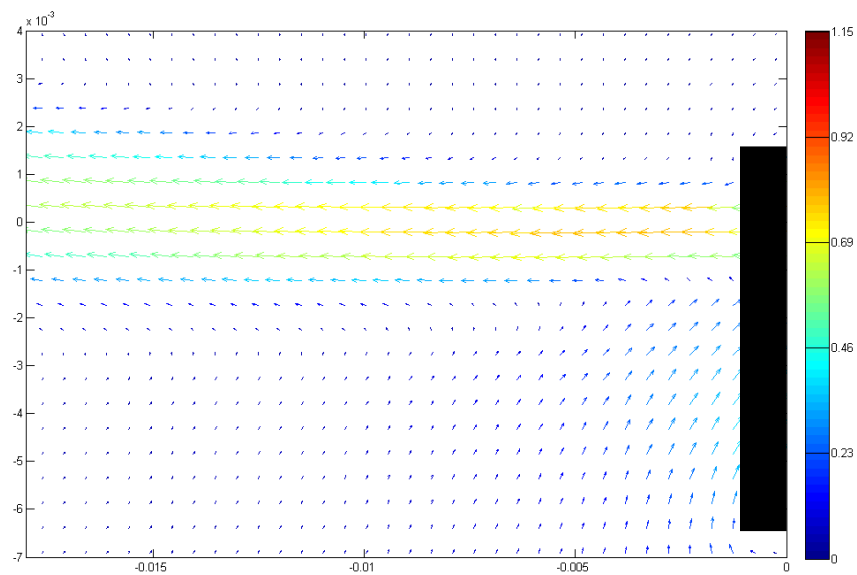
Figure 59. Face 2 middle vertical plane rotated 5º around the Y axis

The same changes in plane location are used for the horizontal planes with a small observed impact, largely owing to the small gradients in velocity field with elevation at this specific plane. Figure 61 shows the planes shifted by 1 mm with little to no change in the velocity distributions. Figure 62 shows the plane rotated 5° around the X axis (directly outwards from the center of the outlet), showing very little change in the flow patterns. Figure 63 shows the plane rotated 5° around the Y axis (intersection of measurement plane and nozzle outlet), indicated very little change in the flow.
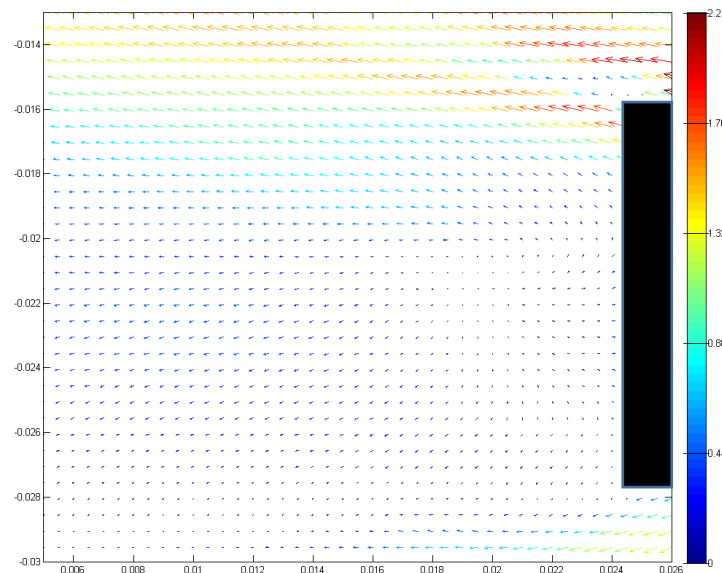
Figure 60: Face 2 middle horizontal original position
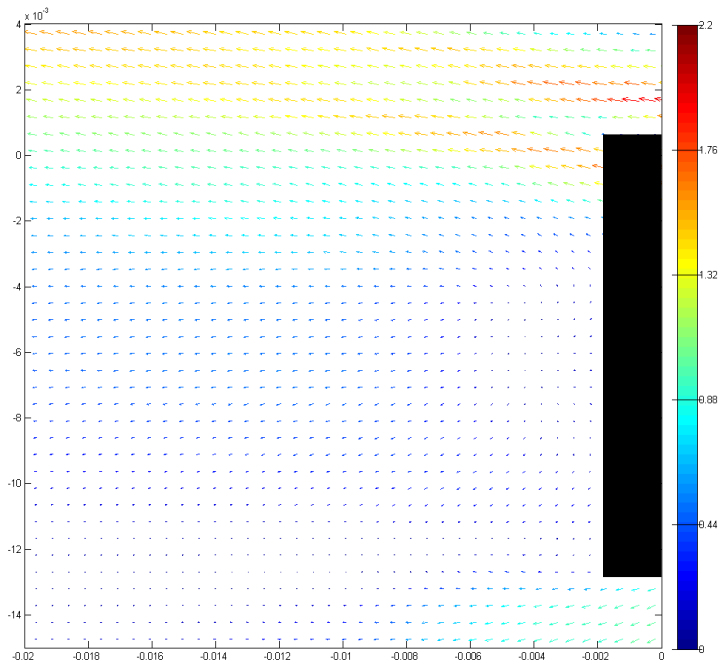
Figure 61. Face 2 plane shifted 1 mm towards top of outlet
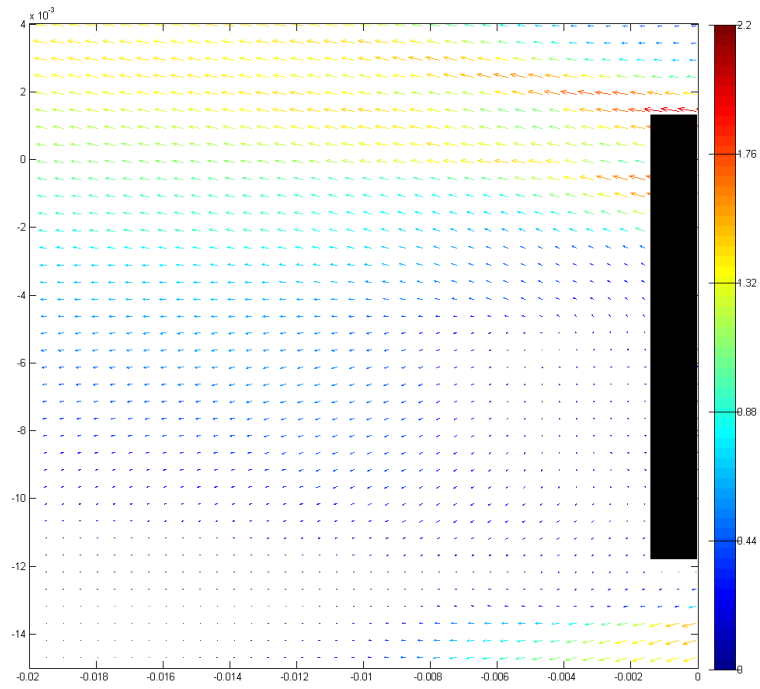
Figure 62. Face 2 middle vertical plane rotated 5º around X axis
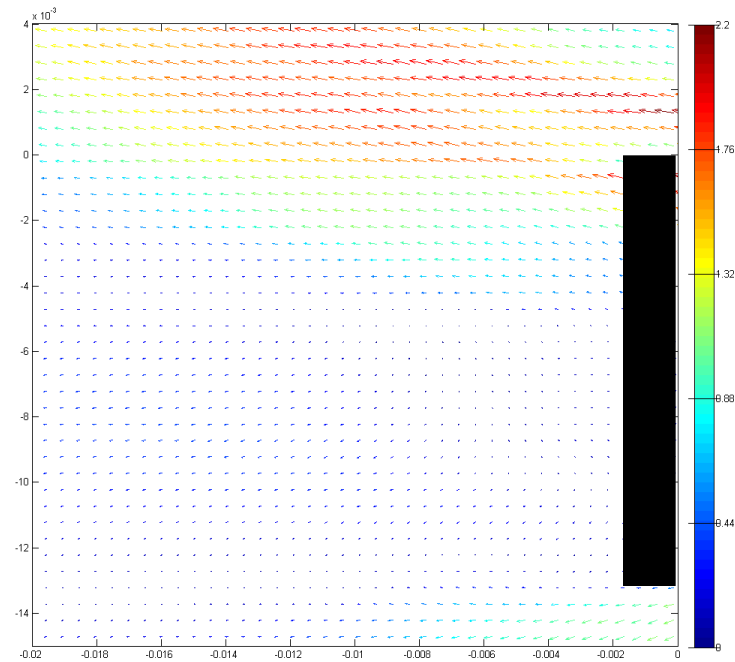
Figure 63. Face 2 middle horizontal plane rotated 5º around the Y axis

The same changes in plane location were applied to face 1. Figures 64-67show the vertical middle plane on face 1 shifted by 1 mm to the right of the original position and rotated 5º around the X (along the center of the outlet directly outwards) and Y axis (along the intersection of the measurement plane and the outlet). These do not show any major changes of the calculated velocity distributions from this outlet and at face 1 elevation.
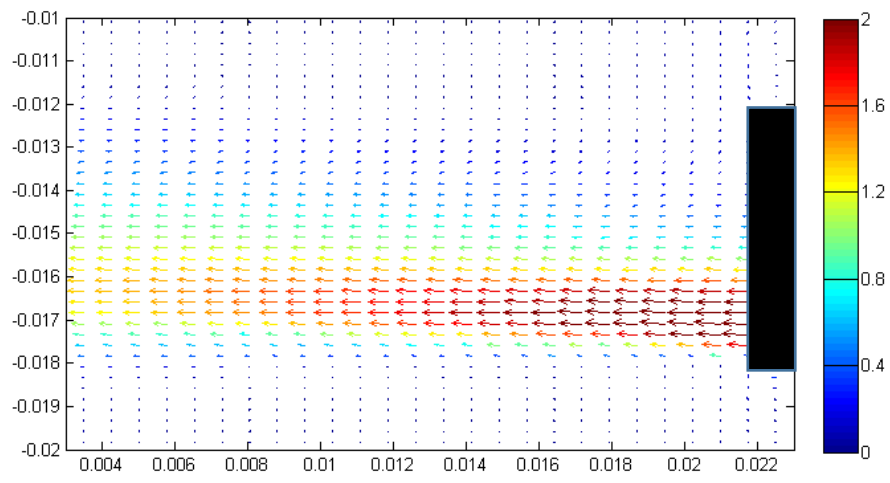
Figure 64: Face 1 middle vertical original position
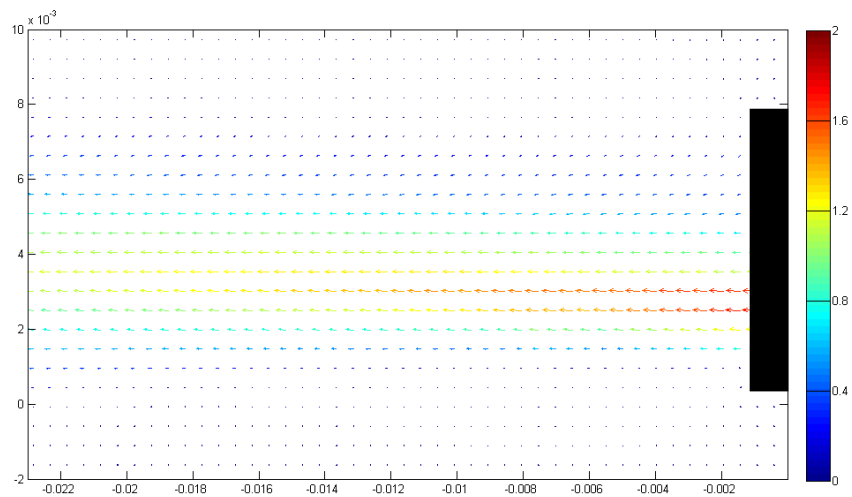
Figure 65. Face 1 middle plane shifted 1 mm to right of outlet
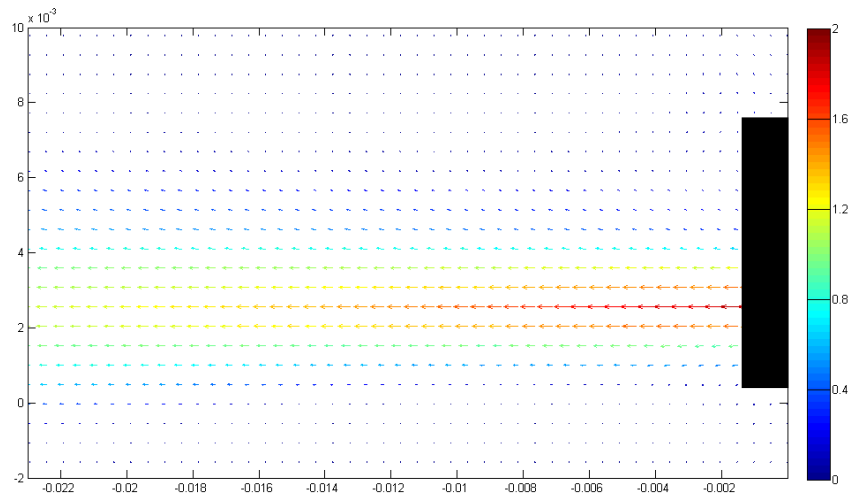
Figure 66. Face 1 middle vertical plane rotated 5º around Y axis
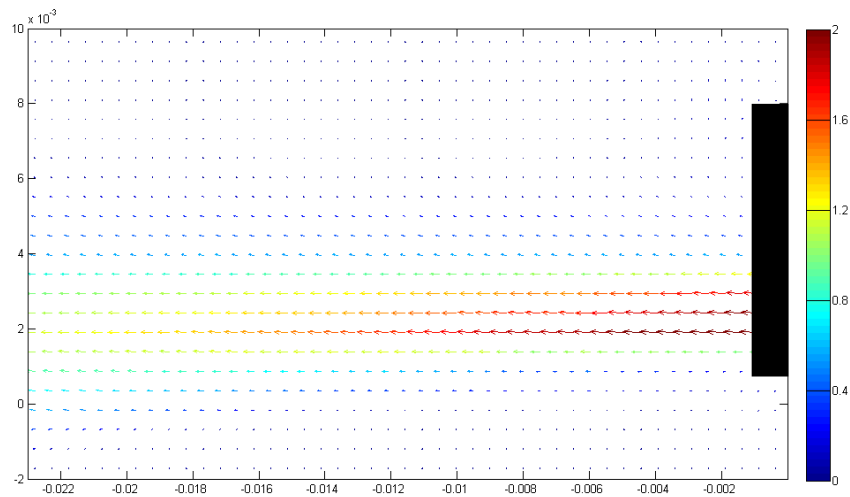
Figure 67. Face 1 middle vertical plane rotated 5º around X axis

For the horizontal middle plane on face 1 the changes in angle and plane shift position have a much greater effect on the flow field. Figure 69, Figure 70 and

Figure 71 show the middle horizontal plane on face 2 shifted 1 mm and rotated 5º around X and Y axis. Moving the plane up or down results in an appreciable change in the velocity field. Rotating the plane causes the peak velocity location to significantly change position and magnitude.
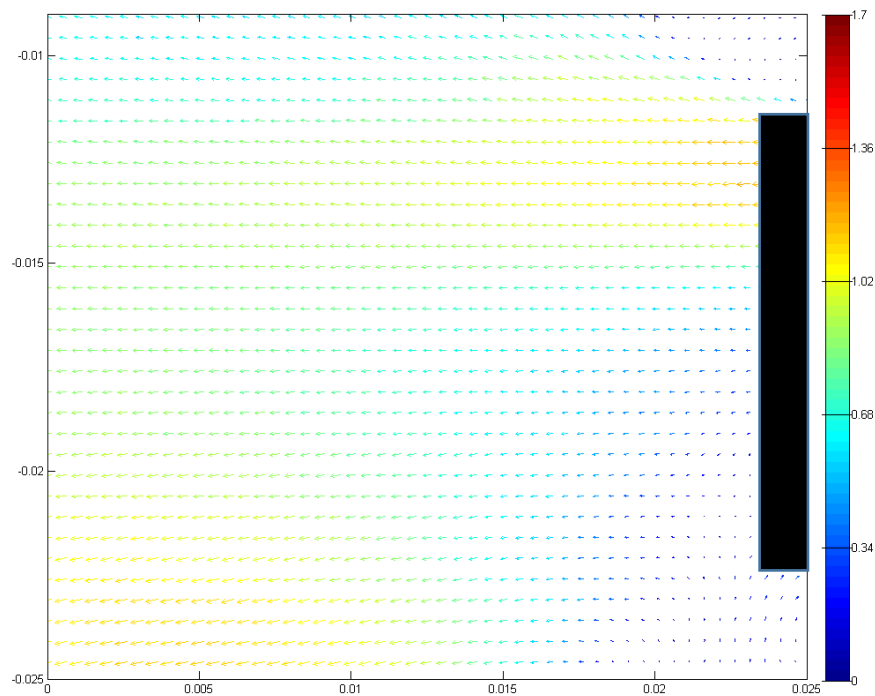
Figure 68: Face 1 horizontal original position
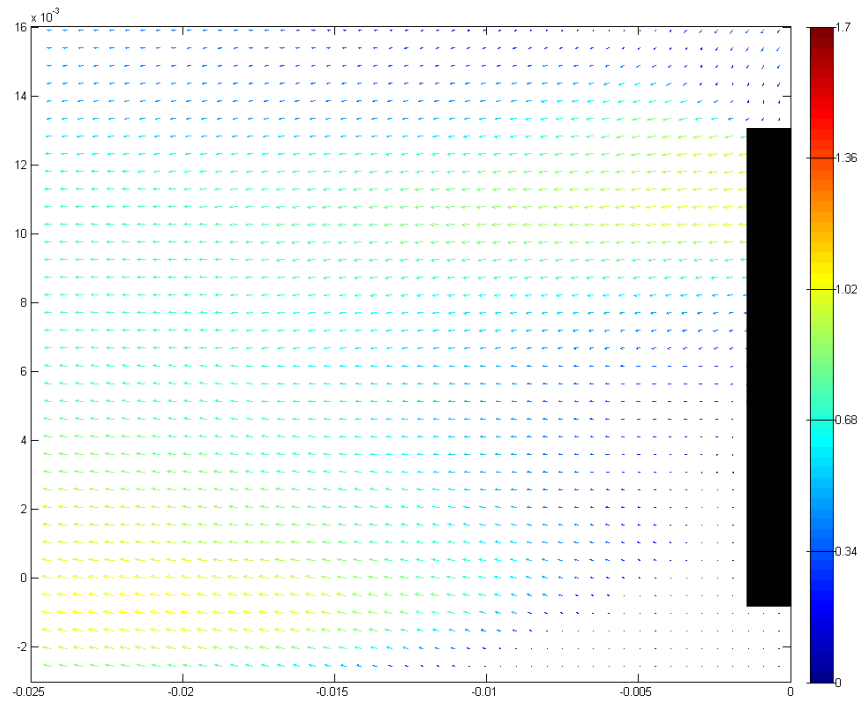
Figure 69. Face 1 middle horizontal plane shifted 1 mm towards the top
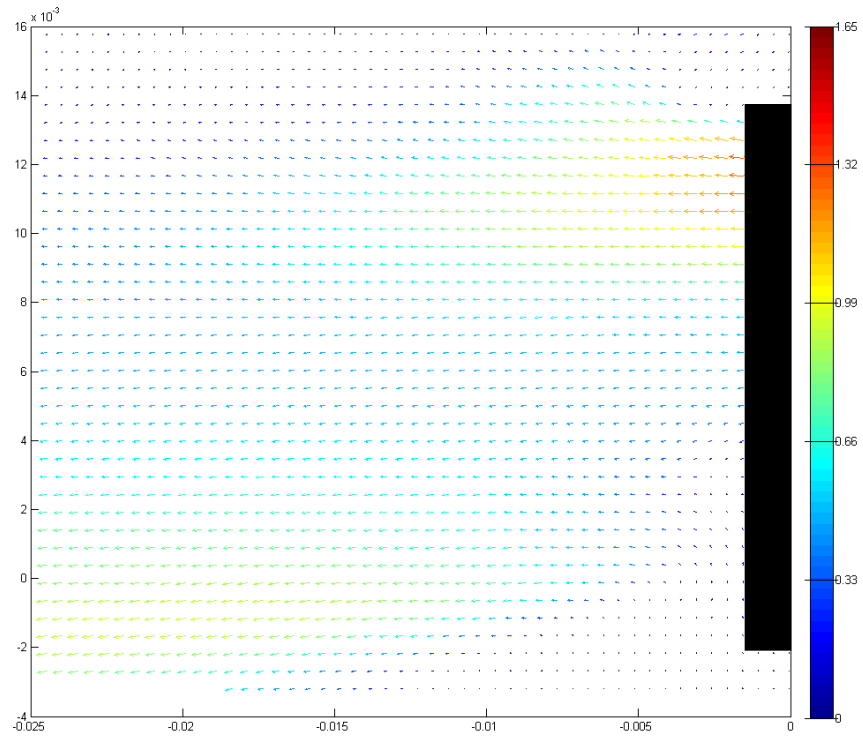
Figure 70. Face 1 middle horizontal plane rotated around x axis
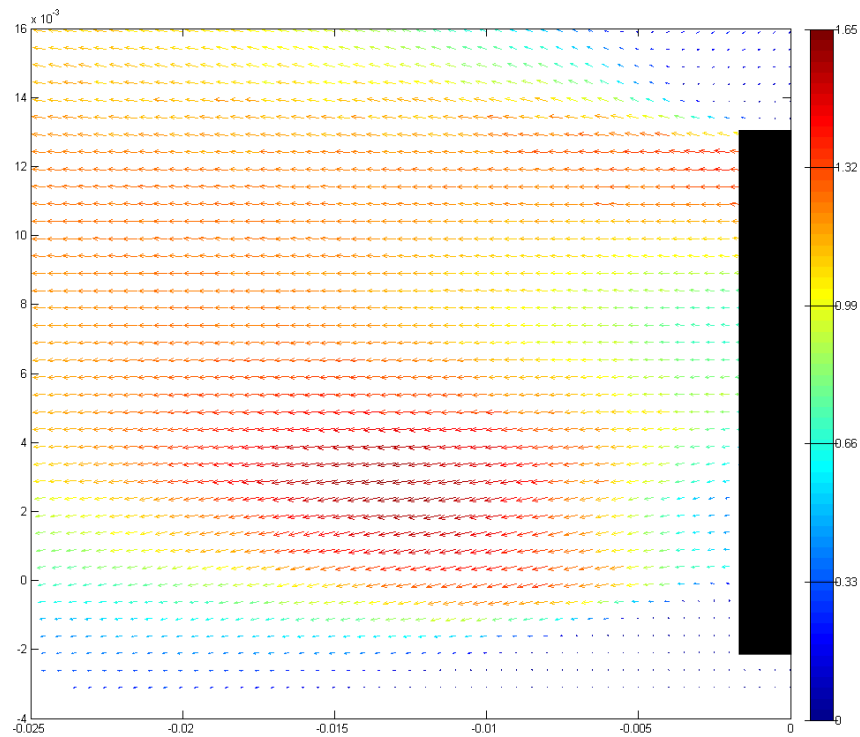
Figure 71. Face 1 middle horizontal plane rotated 5º around y axis

Figures 73-76 show the direct view plane of face 2 rotated and shifted outwards. The velocity profiles do not change significantly with any movement of the plane also retaining the vortex location and shape. However, rotating the plane around the vertical axis shows a significant change in the velocities to the right of the outlet, though the velocity magnitude still remains higher than obtained with the PIV measurements.
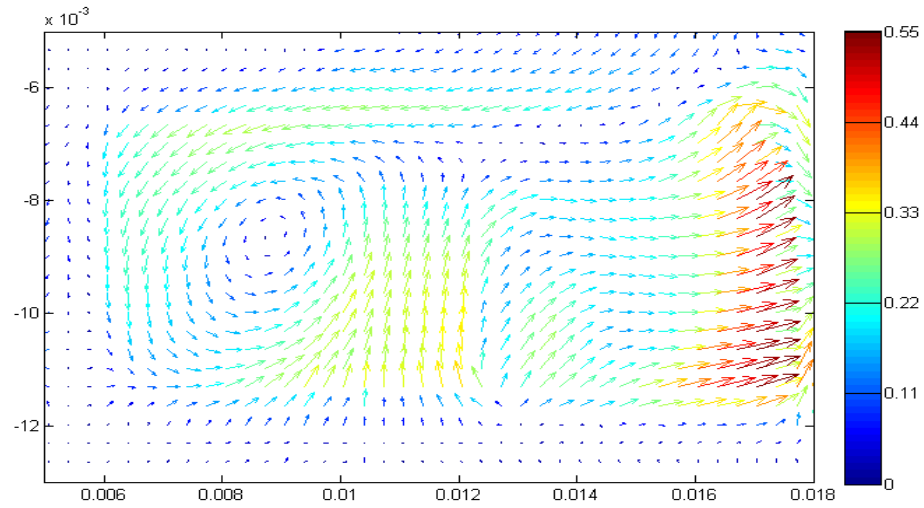
Figure 72: Face 2 direct original position
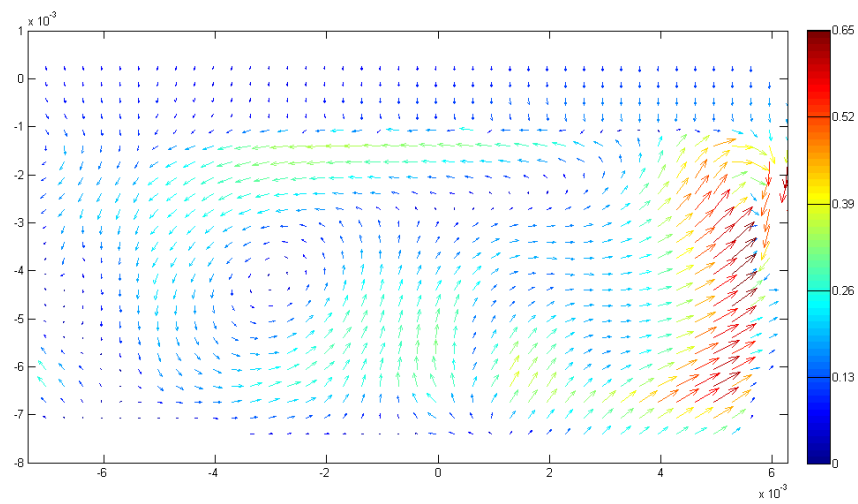
Figure 73. Face 2 direct plane rotated 5º around X axis

T.M.J. Sheasgreen
M.A.Sc. Thesis

Chapter 7
Results And Discussion

McMaster University
Engineering Physics
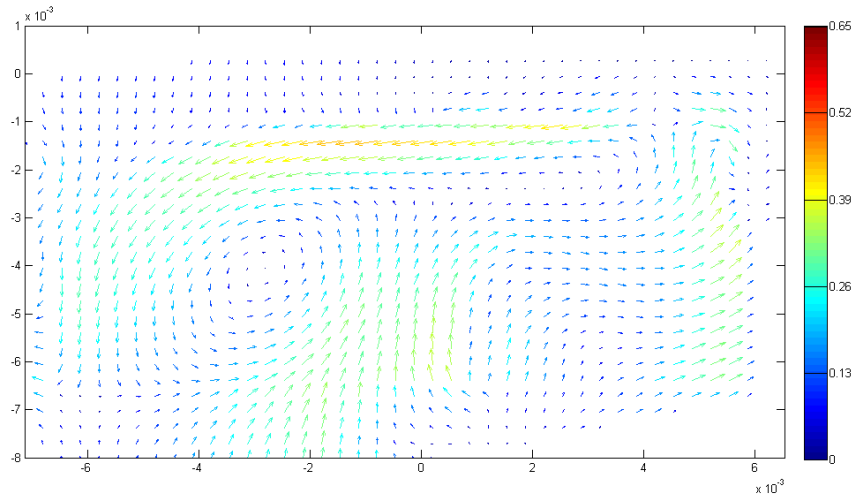
Figure 74. Face 2 direct plane rotated 5º degrees around Y axis
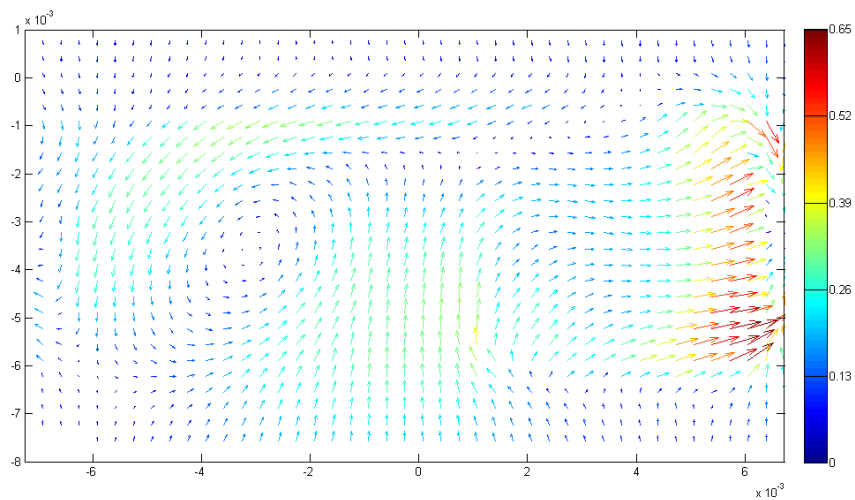
Figure 75. Face 2 direct 1 mm out from outlet

Figures 77-80 show the face 1 direct view plane rotated and shifted outwards. The velocity profile does not change significantly when the orientation is changed. The magnitudes also exhibit little change with the exception of the top left portion when the plane is rotated around the horizontal axis.
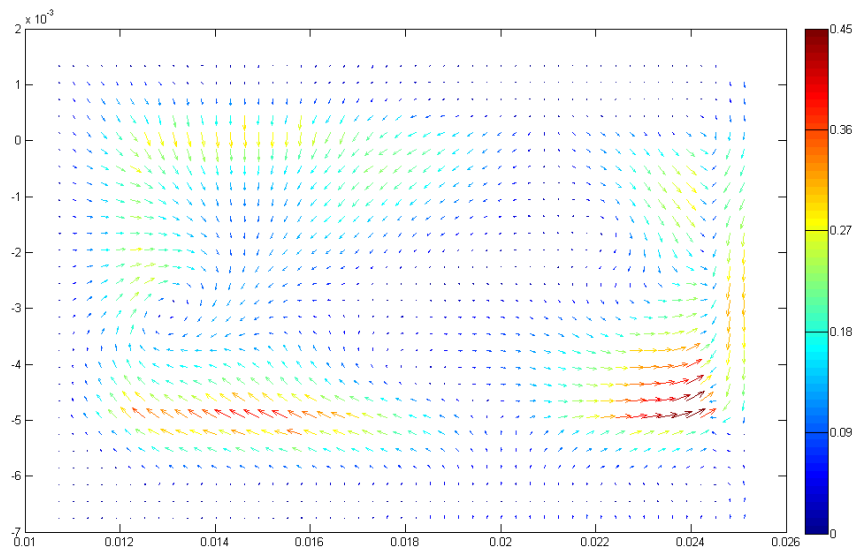
Figure 76: Face 1 direct original position
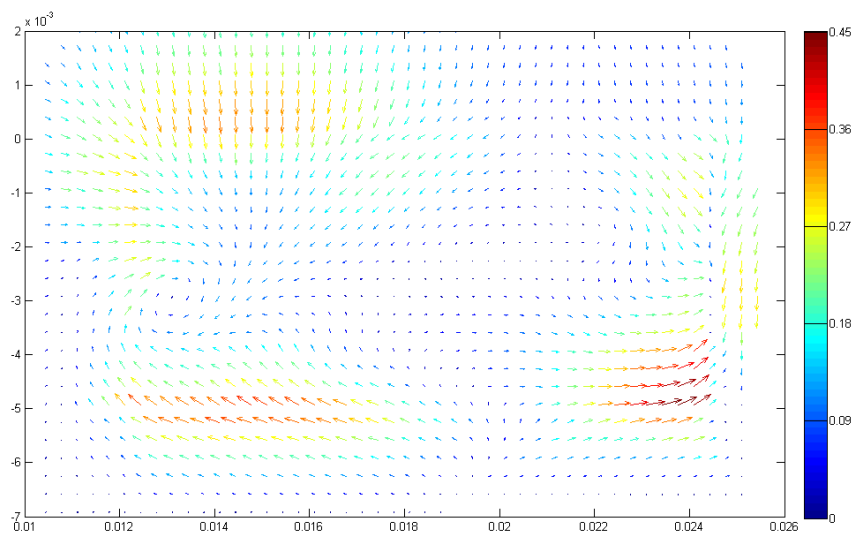
Figure 77. Face 1 direct rotated 5º around X axis
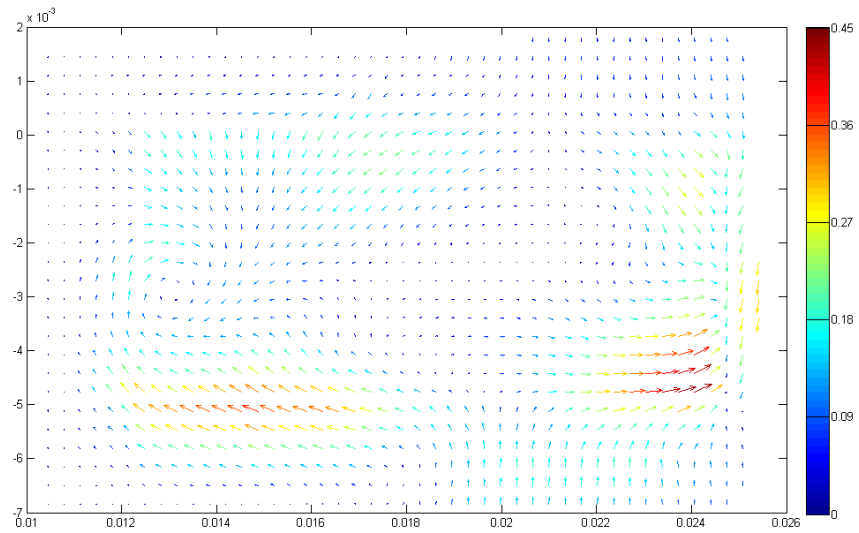
Figure 78. Face 1 direct rotated 5º around Y axis
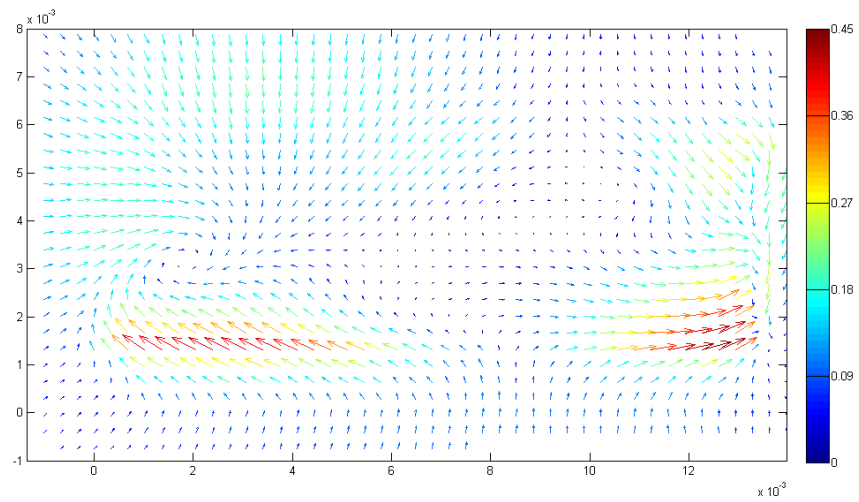
Figure 79. Face 1 direct 1 mm out from outlet

8. CONCLUSIONS

Water velocity measurements were undertaken close to the outlet from a scaled down version of a Pickering Nuclear Reactor moderator nozzle. Seven velocity planes were measured using a PIV laser system on two of the outlet faces of the nozzle (the other two being assumed symmetric), and compared to results predicted using two RANS based turbulence models. A thorough procedure, involving the positional and angular locations of the laser and detector was developed and applied to the experimental set-up of the PIV system to ensure accurate results. The impacts of the uncertainty in key measurement parameters on the obtained velocity vector field was quantified. The velocity fields were post-processed to the form suitable to be compared to the CFD simulation results obtained employing the same boundary conditions as in the experiment. k-ω SST model generally outperformed its k-ε counterpart in terms of agreement with the experimentally observed velocity fields.

While most of the calculated results were in qualitative agreement with the measured velocity fields, the peak velocity magnitudes were found to be generally higher in the simulation compared to the physical results. The possible reasons for the observed discrepancies were discussed and quantified where possible. The laser sheet finite thickness, the positional uncertainty of both the laser sheet and the CCD camera were shown to be partly responsible for the insufficient CFD results quality.

Based on the results obtained in the present study it is rather hard to state the sufficiency of the employed turbulence models to cope with the all the phenomena present, like secondary flows, boundary layer separation and reattachment, to name a few. The results obtained with both models used agreed qualitatively. Some quantitative differences were not consistently closer to the experimentally observed results, depending on the measurement plane in question.

The impact of the uncertainties of the measurement plane position were quantified. It was found that changing the plane position within the limits of the relevant position tolerance can bring the comparison of computed and measured results much closer than for the nominal positions. The laser measurements were not very sensitive to changes in angle of the beam, although at one location the effect was much more pronounced (due to high gradients in the region near that specific measurement plane). Sensitivity to translation was in general larger than that due to angular alignment since translation systematically moves the beam through a gradient while angular rotations leave some portions of the beam thickness nearer to the original unperturbed location. On relatively small scale nozzle employed in the present study, high quality PIV measurements are difficult to achieve.

The following is recommended as an extension of the present work:

- The results obtained in the near field in the present study could be of limited use for the Pickering scaled down tank simulations. It is suggested to measure and calculate the flow field at distances of around 10 to 15 nozzle

heights. Comparing the measured and the calculated using different turbulence models results at these locations could be used to establish the modelling strategy in a way similar to the reported in the present study.

- A larger nozzle could be studied and compared to the results shown here to determine the potential scaling effects in a nozzle. Such a larger test would likely have smaller PIV uncertainties since the beam thickness and position relative to the characteristic dimension of the larger fan nozzle would be smaller.

- Additional analysis of the sensitivity of the position and orientation of the measurement place should be done on different locations at the nozzle outlets.

- Using LDV is recommended thus allowing to take measurement over a more precisely controlled area through gradients.

- Additional turbulence models could be assessed to see if they have more diffusive behavior, and hence better agreement with the measured results.

- More extensive verification method, using different experiments with different geometry elemenys, as well as a more thorough mesh sensitivity analysis for a better convergence.

9. REFERENCES

1. Austman, G., Szymanski, J., Garceau, M., & Midvidy, W. I. (1985). Measuring moderator temperatures in a CANDU reactor, 6th Annual Conference of CNS, Ottawa, Canada.

2. Davis, D.O. (1992). Experimental investigation of turbulent flow through a circular-to-rectangular transition duct. NASA Technical Memorandum 105210.

3. Davis, D. O., & Gessner, F. B. (1992). Experimental investigation of turbulent flow through a circular-to-rectangular transition duct. AIAA journal, 30(2), 367-375.

4. Day, Melissa (2013). Quiverwcolorbar (https://www.mathworks.com/matlabcentral/fileexchange/40224-quiverwcolorbar), MATLAB File Exchange. Retrieved December, 2016.

5. Demuren, A. O., & Rodi, W. (1984). Calculation of turbulence-driven secondary motion in non-circular ducts. Journal of Fluid Mechanics, 140, 189-222.

6. Furbo, E., Harju, J., & Nilsson, H. (2009). Evaluation of turbulence models for prediction of flow separation at a smooth surface. Report in Scientific Computing Advanced Course-Project, 9.

7. Gerolymos, G. A., & Vallet, I. (2016). Reynolds-stress model prediction of

3-D duct flows. Flow, Turbulence and Combustion, 96(1), 45-93.

8. Höhne, T., Kliem, S., & Vaibar, R. (2009). Experimental and numerical modeling of transition matrix from momentum to buoyancy-driven flow in a pressurized water reactor. Journal of Engineering for Gas Turbines and Power, 131(1), 012906.

9. Huget, R. G., Szymanski, J. K., & Midvidy, W. I. (1989). Status of physical and numerical modelling of CANDU moderator circulation, 10th annual conference of the Canadian Nuclear Society, Ottawa, ON (Canada), 4-7 Jun 1989

10. Huget, R. G., Szymanski, J. K., & Midvidy, W. I. (1990). Experimental and numerical modelling of combined forced and free convection in a complex geometry with internal heat generation. In Proceedings of 9th International Heat Transfer Conference (Vol. 3, p. 327).

11. Khartabil, H. F., Inch, W. W. R., Szymanski, J., Novog, D., Tavasoli, V., & Mackinnon, J. (2000). Three-dimensional moderator circulation experimental program for validation of CFD code MODTURC-CLAS.

12. Kim, H. T., Cha, J. E., Rhee, B. W., Choi, H. L., Seo, H., & Bang, I. C. (2013, c). Measurement of velocity and temperature profiles in the scaled-down CANDU-6 moderator tank. In 2013 21st International Conference on Nuclear Engineering (pp. V004T09A050-V004T09A050). American Society of Mechanical Engineers.Busan.

13. Kim, H. T., Seo, H., & Cha, J. E. (2013,b). Measurement of Velocity Profile

in the 1/8 Scale CANDU-6 Moderator Tank Using Particle Image Velocimetry. In Proceedings of 9th Pacific Symposium on Flow Visualization and Image Processing, Busan, Korea.

14. Kim, H. T., Rhee, B. W., Cha, J. E., & Choi, H. L. (2013, a). Status of moderator circulation test at Korea atomic energy research institute. In Proceedings of Korea Nuclear Society Spring Meeting, Gwangju, Korea.

15. Kim, M., Yu, S. O., & Kim, H. J. (2006). Analysis on fluid flow and heat transfer inside Calandria vessel of CANDU-6 using CFD. Nuclear Engineering and Design, 236(11), 1155-1164.

16. Kim, W. J., & Patel, V. C. (1994). Origin and decay of longitudinal vortices in developing flow in a curved rectangular duct. TRANSACTIONS-AMERICAN SOCIETY OF MECHANICAL ENGINEERS JOURNAL OF FLUIDS ENGINEERING, 116, 45-45.

17. Koroyannakis, D., Hepworth, R. D., & Hendrie, G. (1983). An experimental study of combined natural and forced convection flow in a cylindrical tank. TDVI-382, AECL, 100.

18. Lamarsh, J. R., Baratta, A. J. (2001). Introduction to nuclear engineering (3rd edition). Upper Saddle River, NJ: Prentice-Hall Inc.

19. Launder et al. Progress in the development of a Reynolds-stress turbulence closure , Journal of Fluid Mechanics Volume 68, Issue 3 April 1975, pp. 537-566.

20. Launder, B. E., Spalding, D. B. The numerical computational of turbulent

flows, computer methods in applied mechanics and engineering, volume 3 issue 2, March 1974, p. 269-289.

21. Mahaffy, J., Chung, B., Song, C., Dubois, F., Graffard, E., Ducros, F., ... & Moretti, F. (2007). Best practice guidelines for the use of CFD in nuclear reactor safety applications (No. NEA-CSNI-R--2007-05). Organisation for Economic Co-Operation and Development.

22. Melling, A., & Whitelaw, J. H. (1976). Turbulent flow in a rectangular duct. Journal of Fluid Mechanics, 78(02), 289-315.

23. Menter, F. R. Improved two-equation k-omega turbulence models for aerodynamic flows, NASA Techinical Report Server , Oct 01, 1992.

24. Miau, J. J., Lin, E. C., Chen, Q. S., Chou, J. H., Pan, D., & Lin, C. K. (1996). Swirling flows in circular-to-rectangular transition ducts. Experiments in fluids, 20(6), 401-409.

25. Rosemount, Sanitary Magmeter Flowtube. 2006-2007. Product data sheet. *http://www2.emersonprocess.com/siteadmincenter/pm%20rosemount%20 documents/00813-0100-4901.pdf*

26. Sarchami, A., Ashgriz, N., & Kwee, M. (2012). Three dimensional numerical simulation of a full scale CANDU reactor moderator to study temperature fluctuations. World Academy of Science, Engineering and Technology, International Journal of Mathematical, Computational, Physical, Electrical and Computer Engineering, 6(3), 221-227.

27. Sion, N. (1983). In-core moderator temperature measurement within candu

reactors. Nuclear Instruments and Methods in Physics Research, 206(3), 527-536.

28. Sotiropoulos, F. (2000). Progress in modeling 3D shear flow using RANS equations and advanced turbulence models. ADVANCES IN FLUID MECHANICS, 27, 209-248.

29. Sotiropoulos, F., & Patel, V. C. (1994). Prediction of turbulent flow through a transition duct using second-moment closure. AIAA journal, 32(11), 2194-2204.

30. Sotiropoulos, F., & Patel, V. C. (1995). Turbulence anisotropy and near-wall modeling in predicting three-dimensional shear-flows. AIAA journal, 33(3), 504-514.

31. Spalart, P., & Allmaras, S. (1992, January). A one-equation turbulence model for aerodynamic flows. In 30th aerospace sciences meeting and exhibit (p. 439).

32. Star-ccm+ user manual CD-adapco

33. Suagiyama, H. (1999, January). Numerical Analysis of Turbulent Structure through a circular to Rectangular transition duct. In Procgs of 5th Jnt. Thermal Engineering Conf.

34. Tsi PIV presentation booklet.

35. Versteeg, H. K., Malalasekera, W. (2007) An Introduction To Computational Fluid Dynamics: The Finite Volume Method (2nd edition). Essex, England: Pearson Education Ltd.

36. Wereley, S. T., & Santiago, J. G. (2000). A PIV algorithm for estimating time-averaged velocity fields. TECHNICAL PAPERS, 285.

37. Wilcox, D. C. (1988). Reassessment of the scale-determining equation for advanced turbulence models. AIAA journal, 26(11), 1299-1310.

38. Yoon, C., Rhee, B. W., & Min, B. J. (2004). 3-D CFD Analysis of the CANDU-6 Moderator Circulation under Normal Operating Conditions". Journal of the Korean Nuclear Society, 36(6), 559-570..

39. Yoon, C., Rhee, B. W., Kim, H. T., Park, J. H., & Min, B. J. (2006). Moderator analysis of Wolsong units 2/3/4 for the 35% reactor inlet header break with a loss of emergency core cooling injection. Journal of Nuclear Science and Technology, 43(5), 505-513.

40. Yu, S.O., Kim, M., Kim, H.J., 2005. Analysis of fluid flow and heat transfer inside calandria vessel of CANDU-6 reactor using CFD. Nuclear Engineering and Technology, 37(6); p. 575-586.

Appendices

PIV measurement 0.1 kg/s
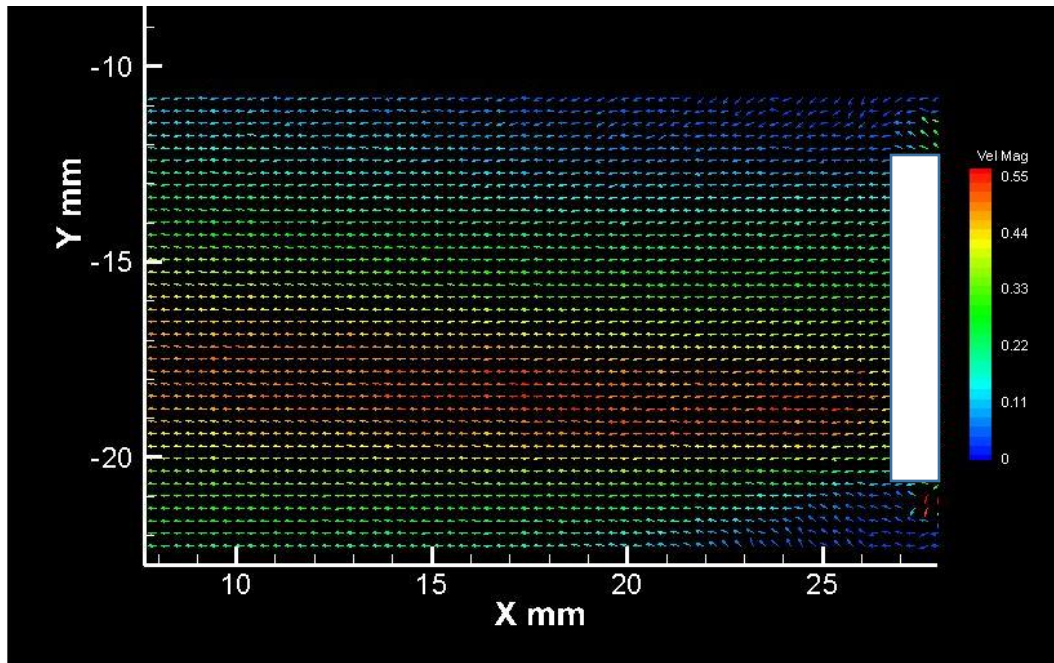
Figure 80: Face 1 middle vertical plane 0.1 kg/s
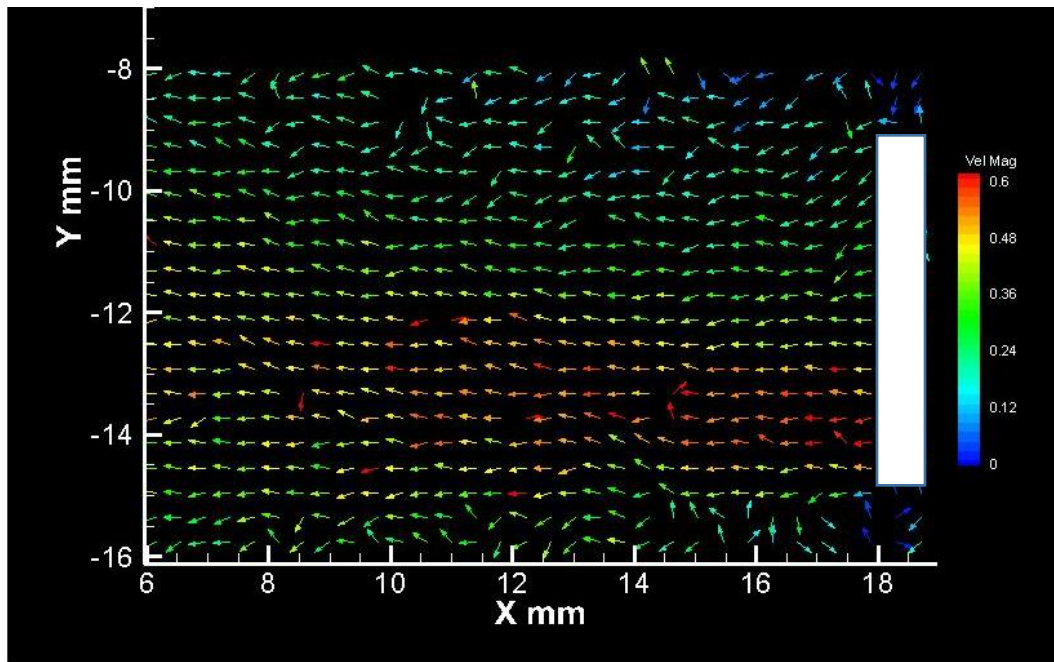
Figure 81: Face 1 left 0.1 kg/s
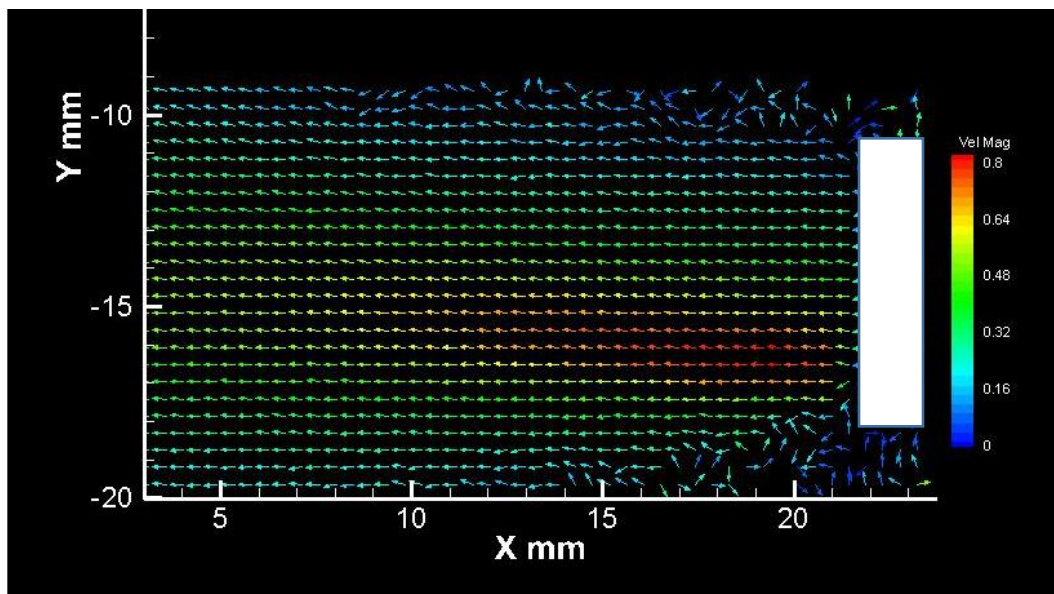
Figure 82: Face 1 right 0.1 kg/s
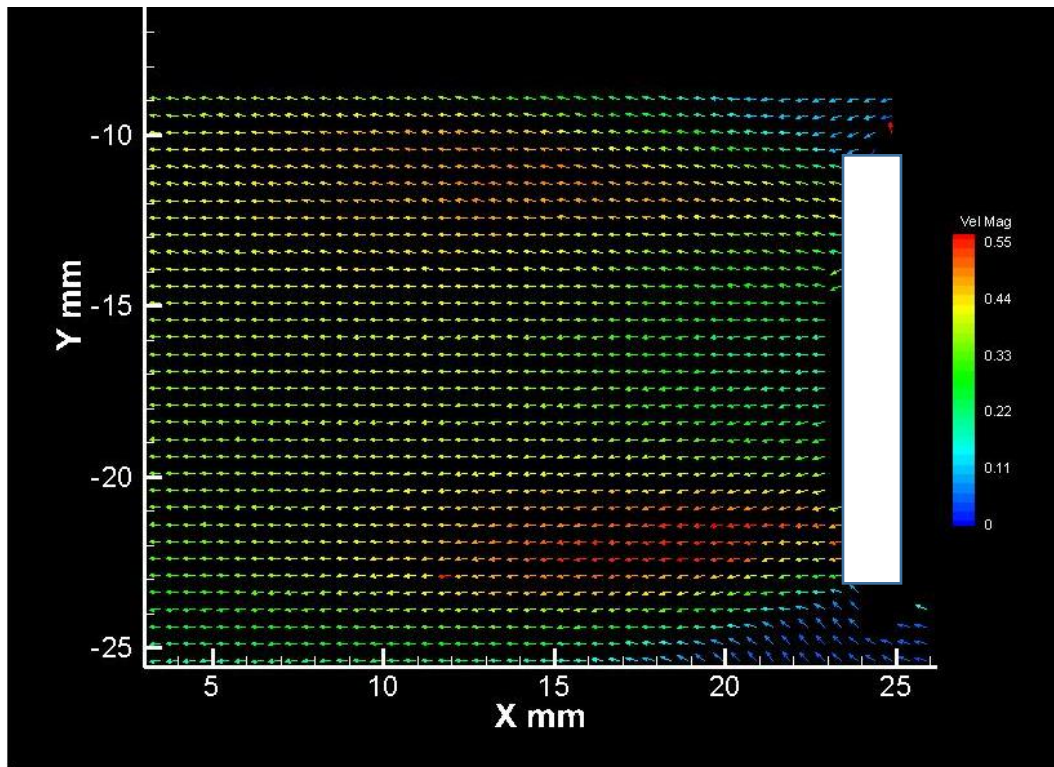
Figure 83: Face 1 middle horizontal 0.1 kg/s
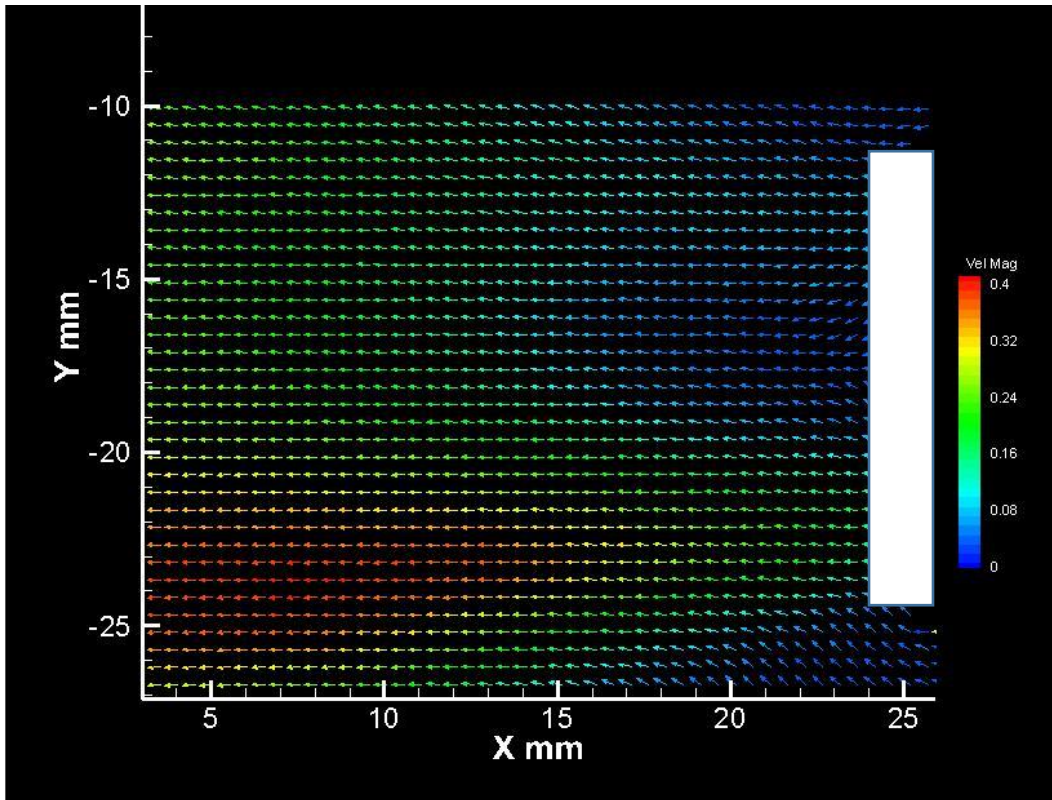
Figure 84: Face 1 top 0.1 kg/s
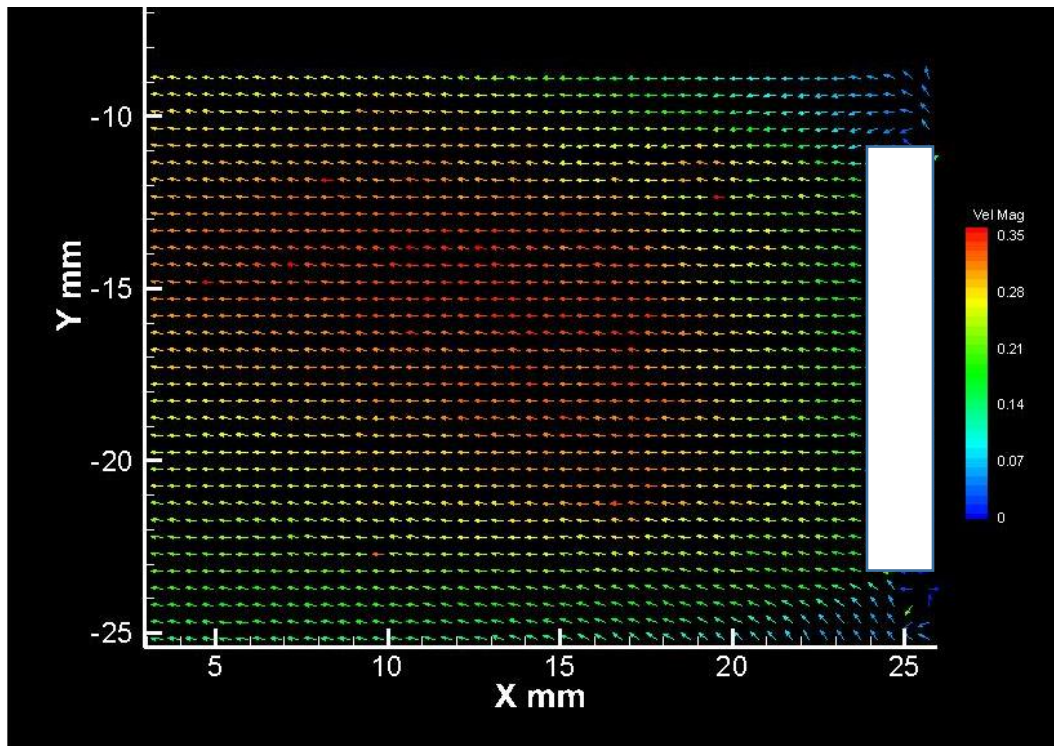
Figure 85: Face 1 bottom 0.1 kg/s
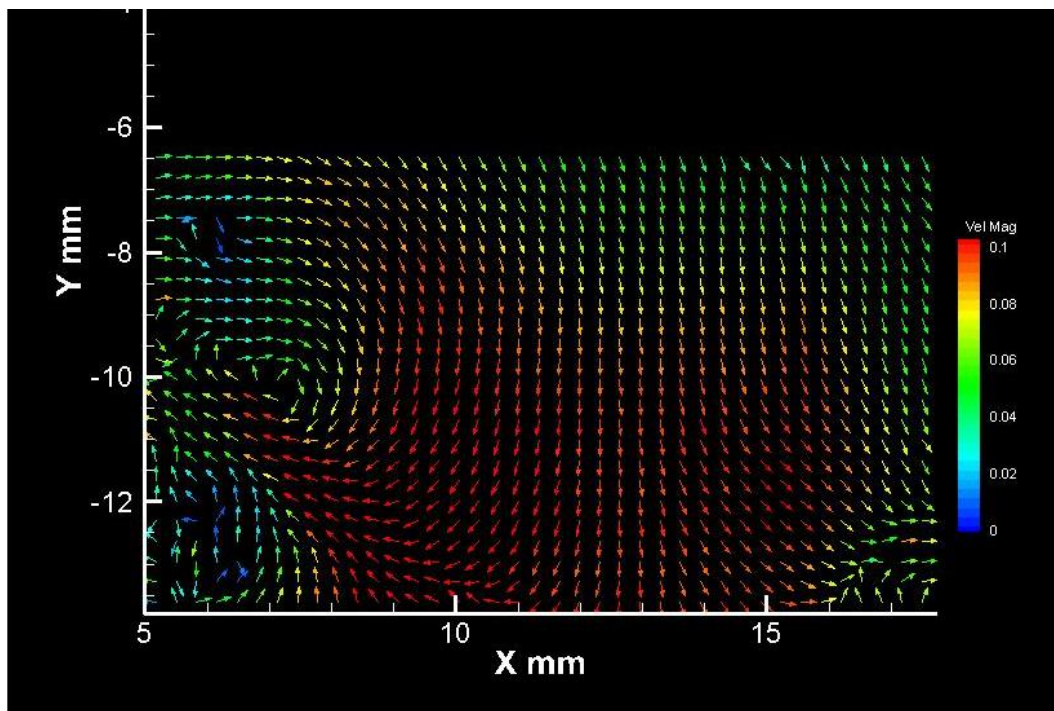
Figure 86: Face 1 direct 0.1 kg/s

119
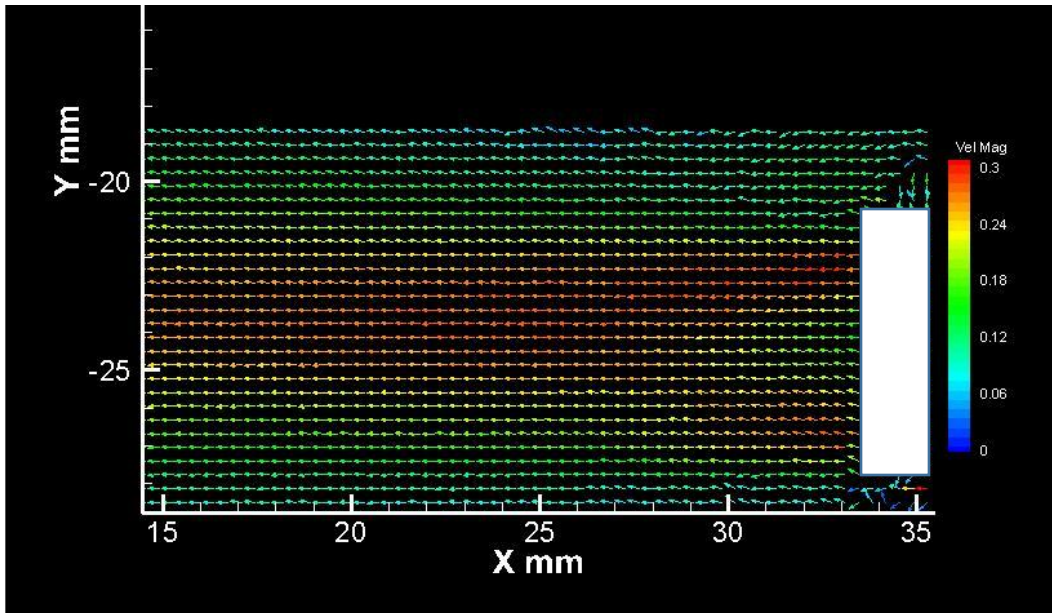
Figure 87: Face 2 left vertical 0.1 kg/s
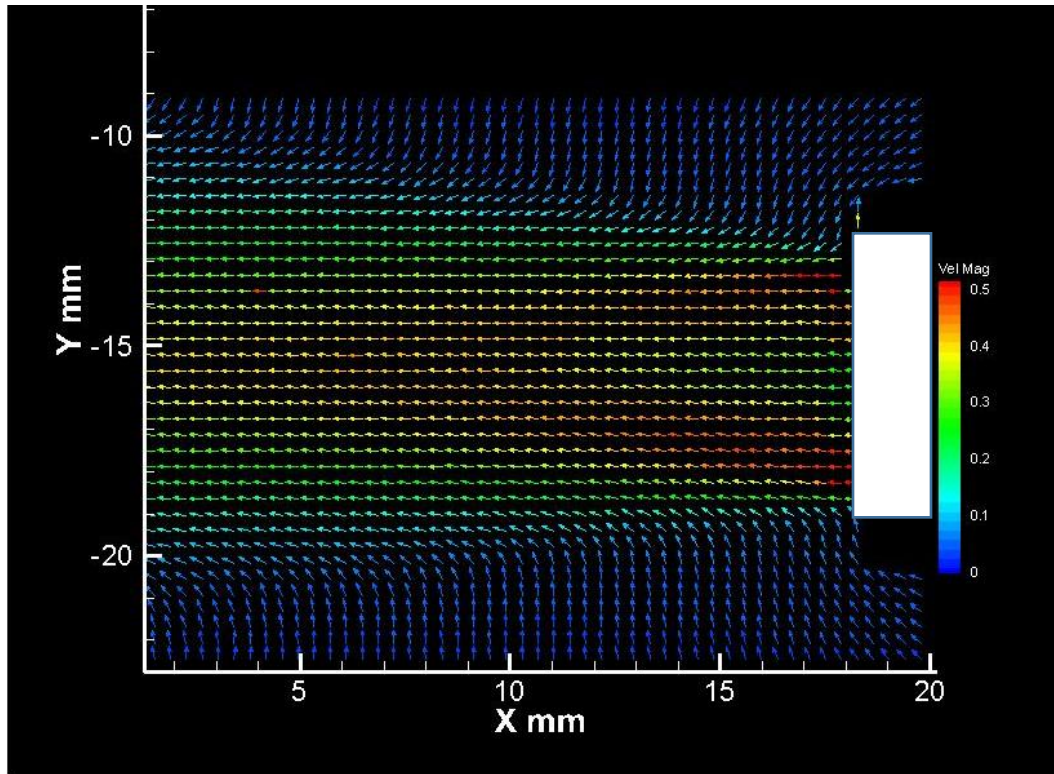
Figure 88 : Face 1 right 0.1 kg/s
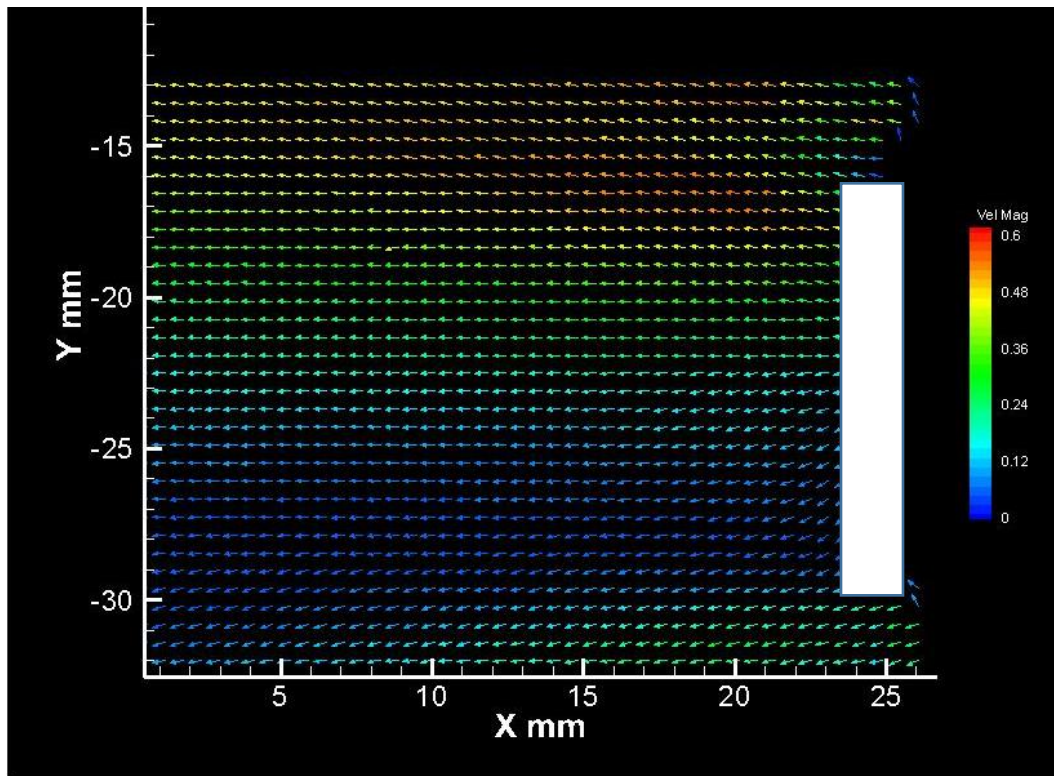
Figure 89 : Face 2 middle horizontal 0.1 kg/s
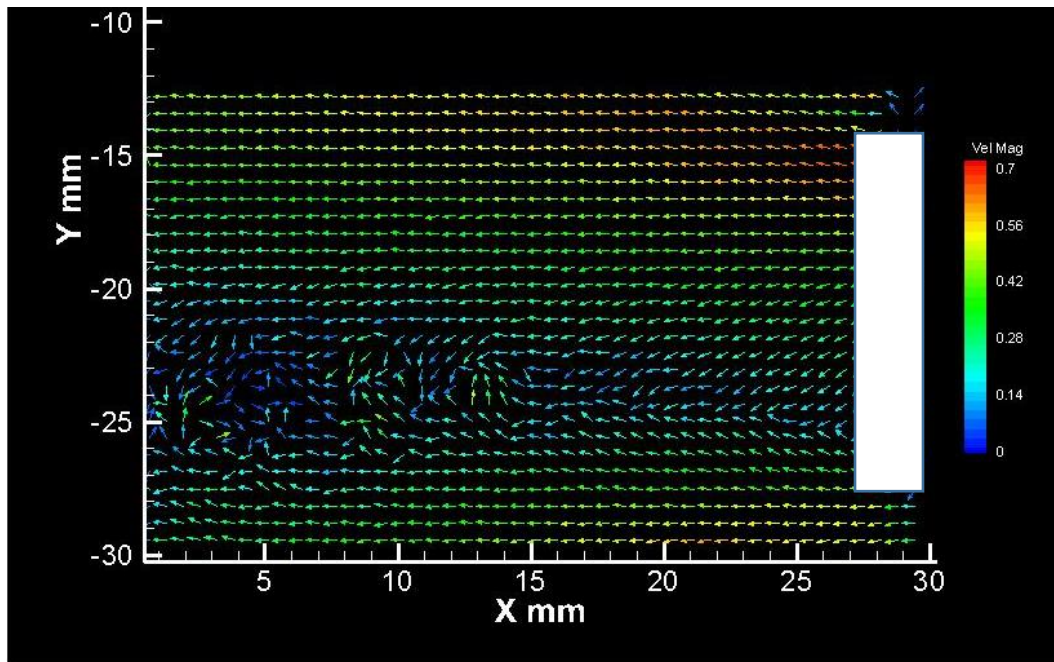
Figure 90 : Face 2 top 0.1 kg/s
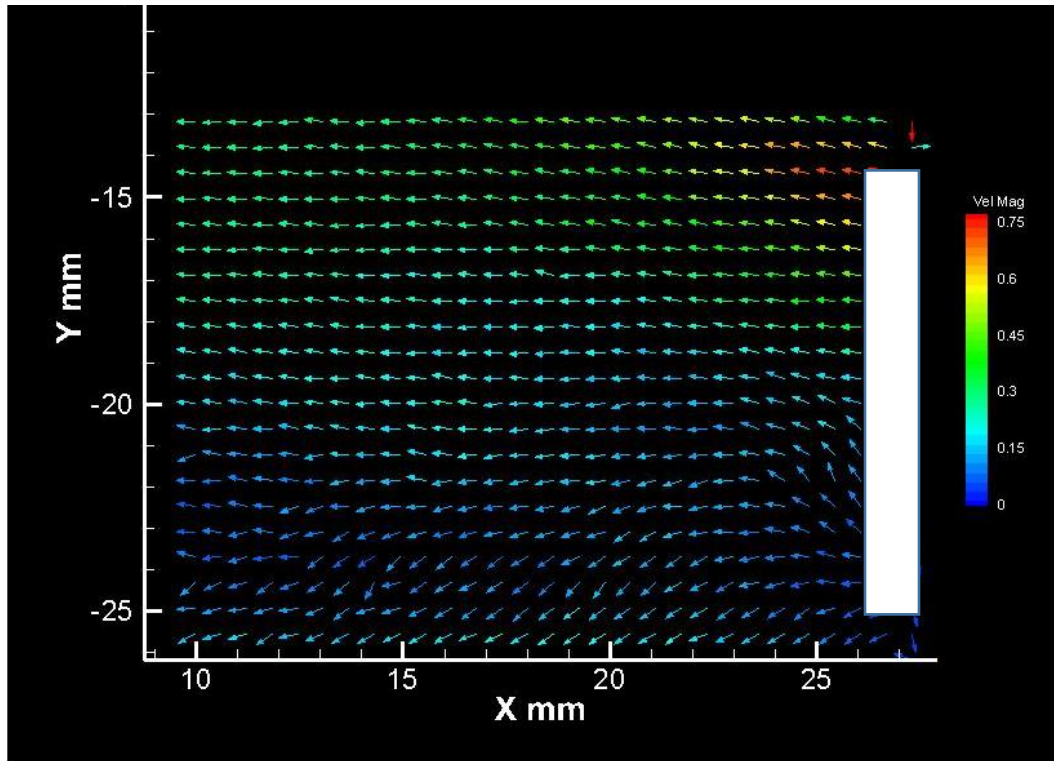
Figure 91 : Face 2 bottom 0.1 kg/s
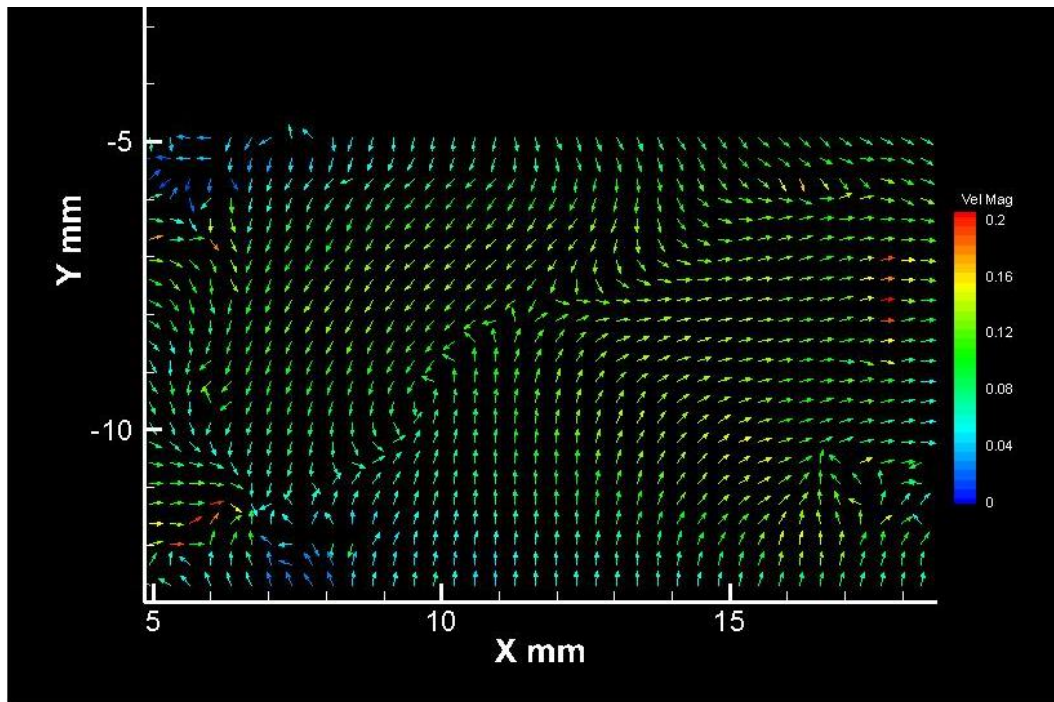
Figure 92 : Face 2 direct 0.1 kg/s

2. CFD 0.1 kg/s results
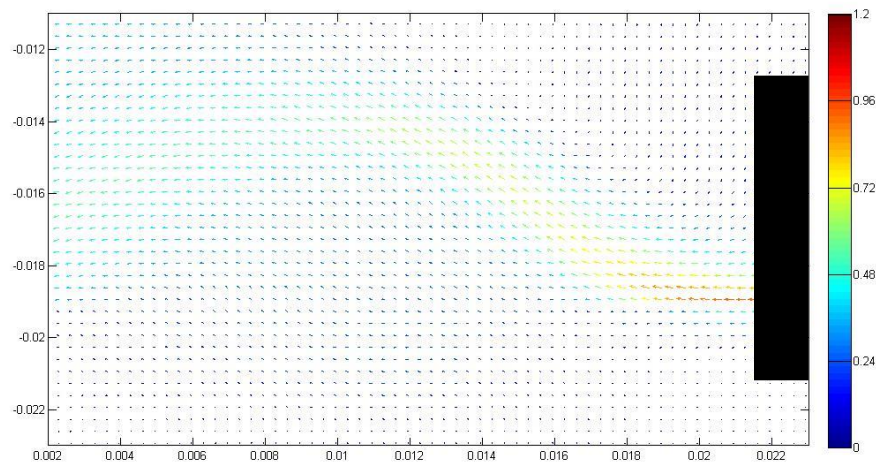
Figure 93 : Face 1 mid 0.1 kg/s
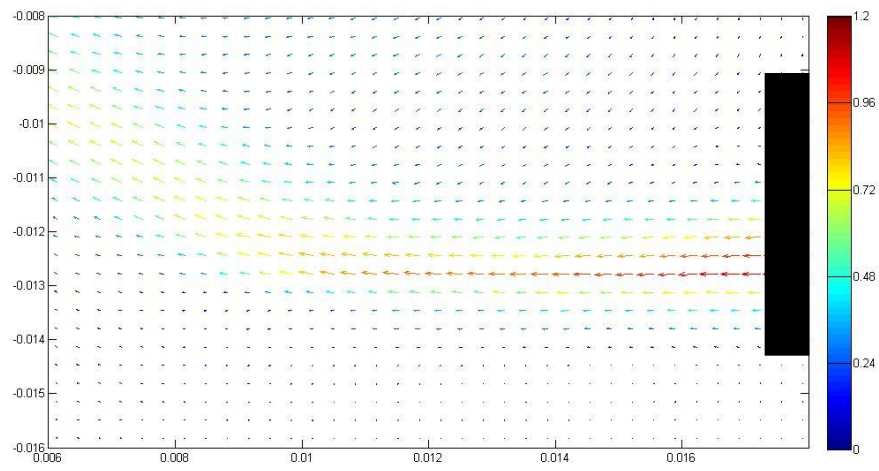
Figure 94: Face 1 left 0.1 kg/s
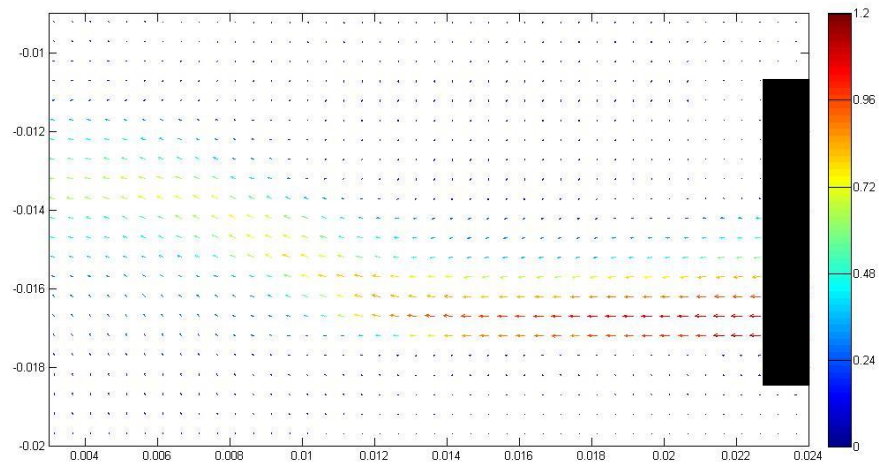
Figure 95: Face 1 right 0.1 kg/s
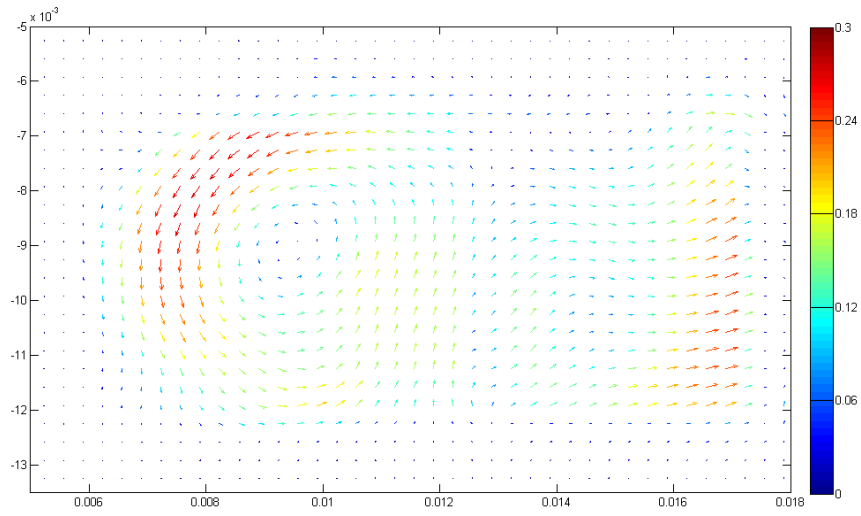
Figure 96: Face 2 direct 0.1 kg/s
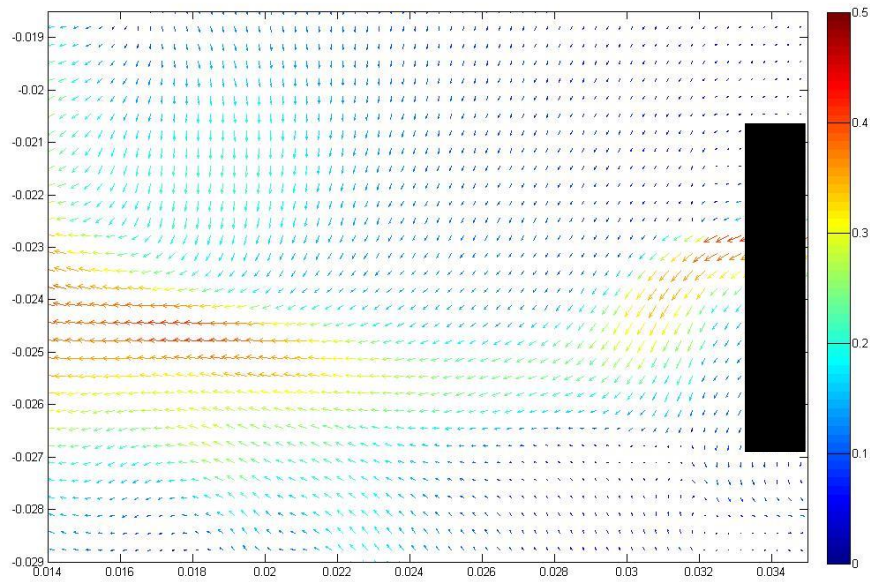
Figure 97: Face 2 left 0.1 kg/s
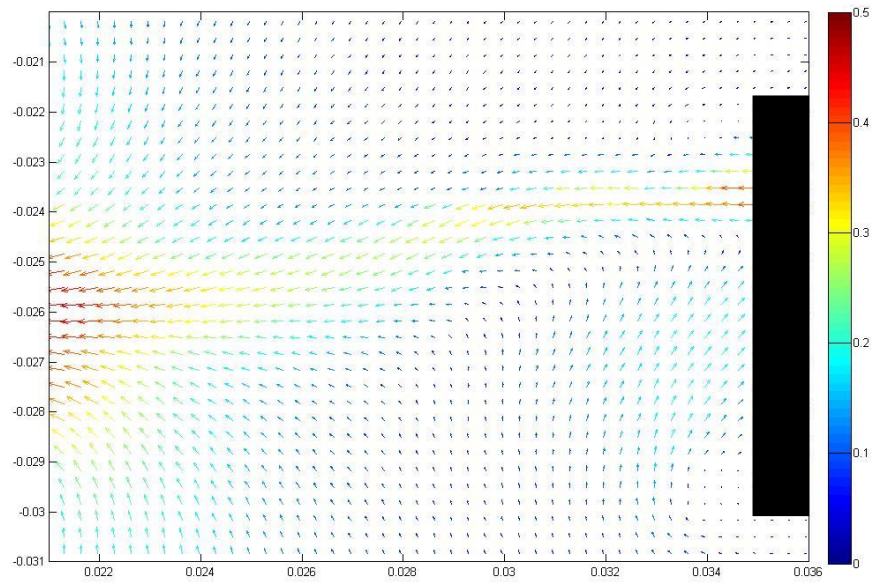
Figure 98: Face 2 mid 0.1 kg/s
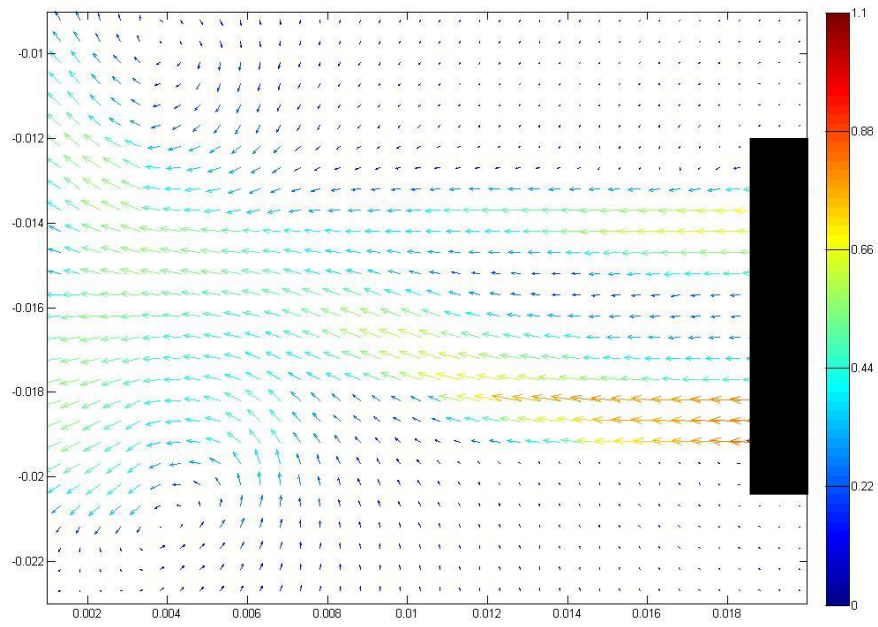
Figure 99: Face 2 right 0.1 kg/s

Other Face 1 results
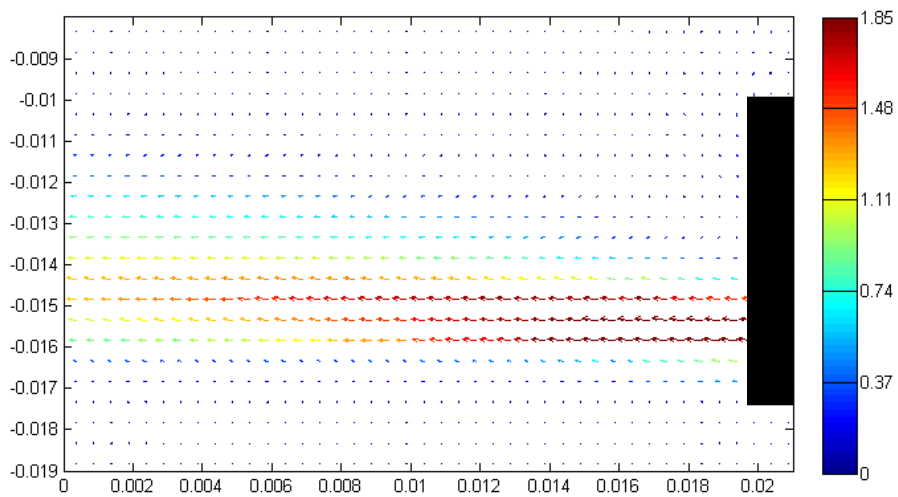
Figure 100: Face 1 right 0.2 kg/s CFD
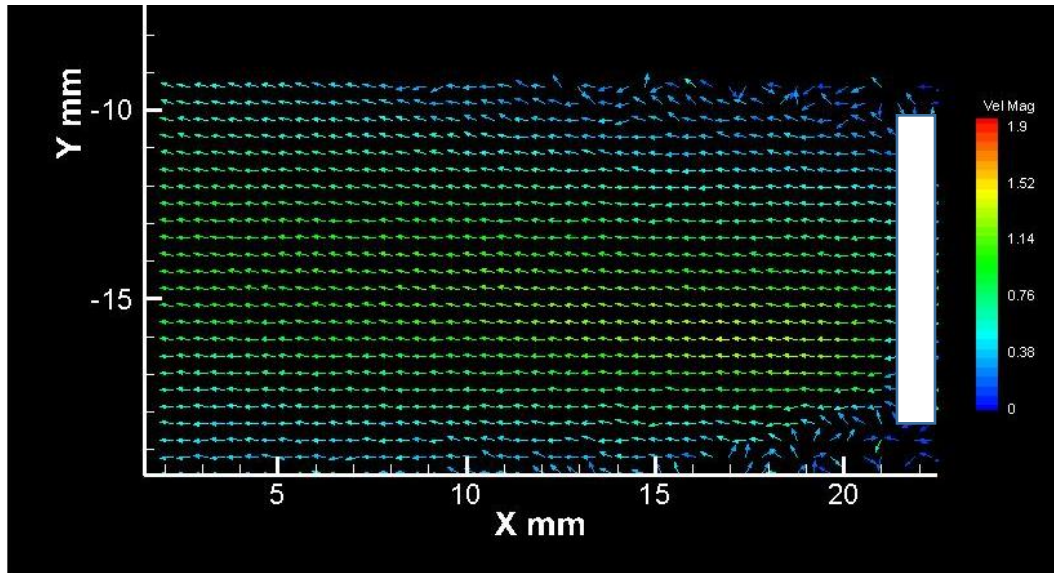
Figure 101: Face 1 right 0.2 kg/s PIV
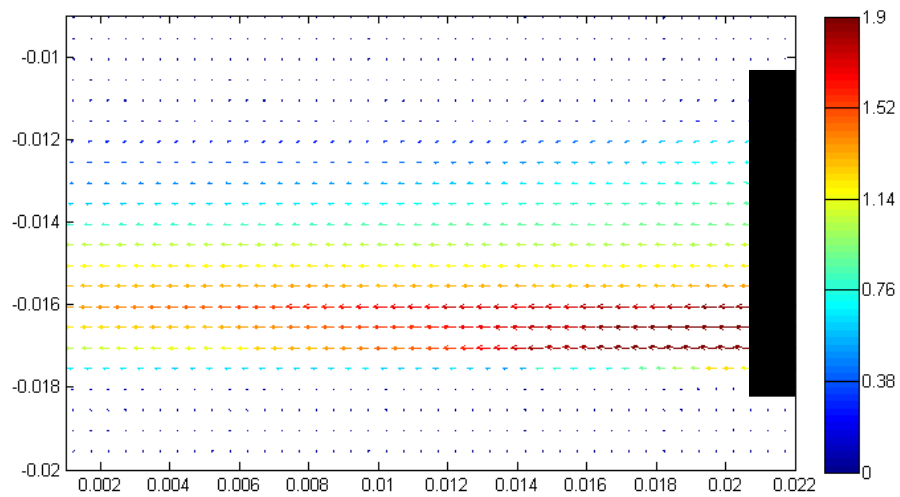
Figure 102: Face 1 left 0.2 kg/s CFD
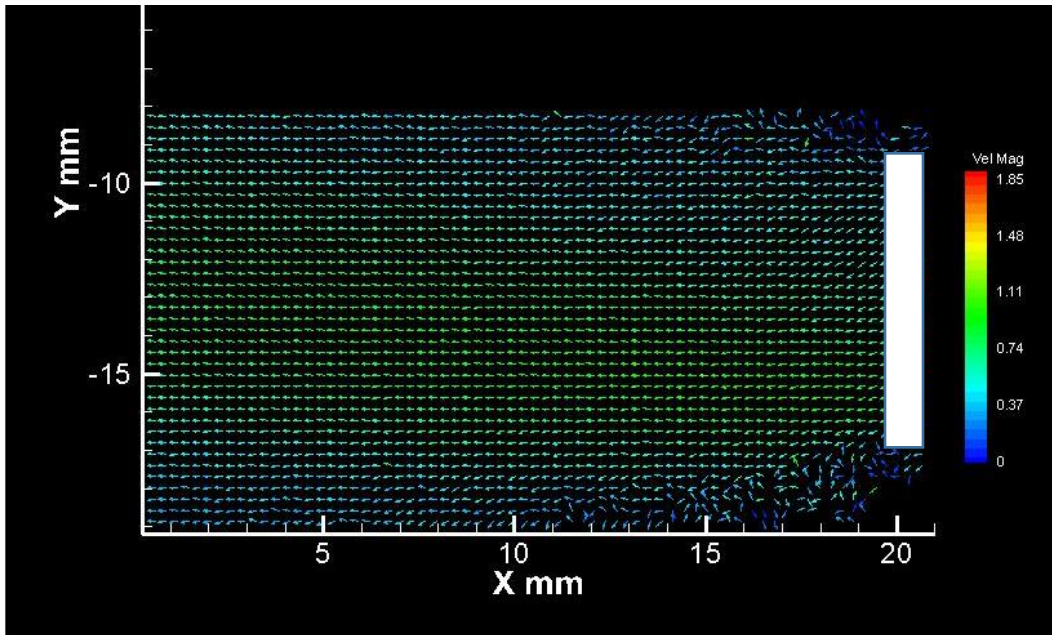
Figure 103: Face 1 left 0.2 kg/s PIV

Other Face 2 results
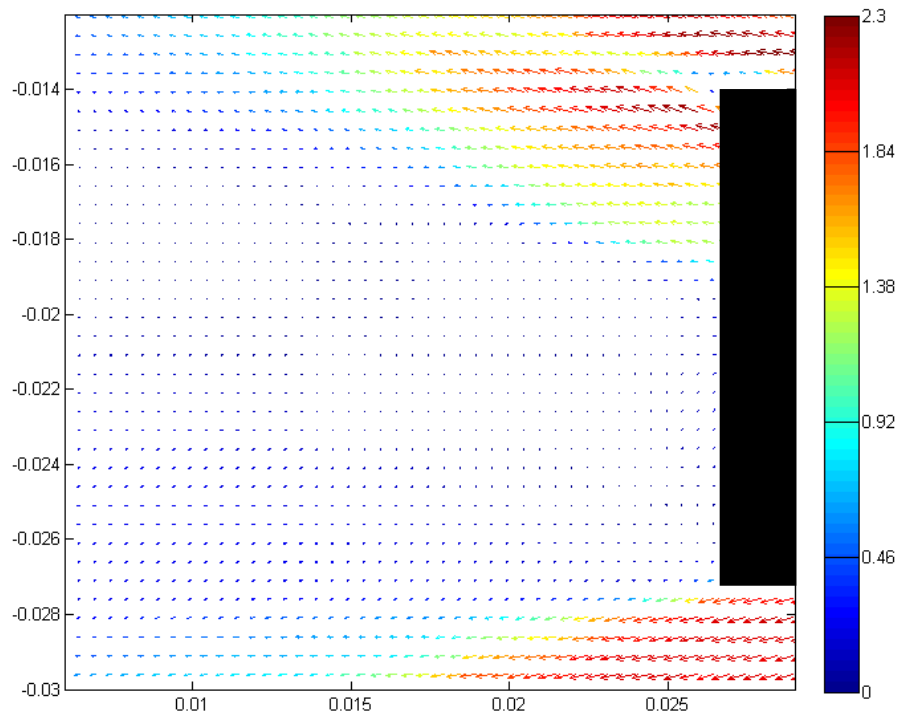
Figure 104: Face 2 bottom 0.2 kg/s CFD
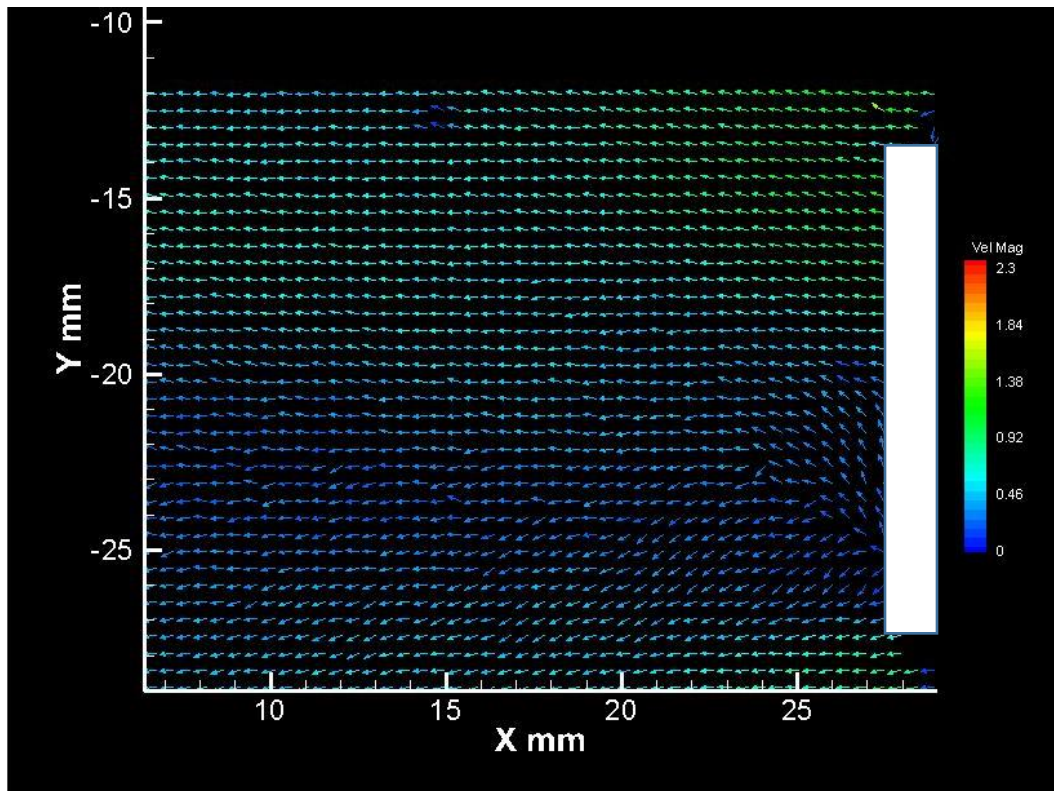
Figure 105: Face 2 bottom 0.2 kg/s PIV
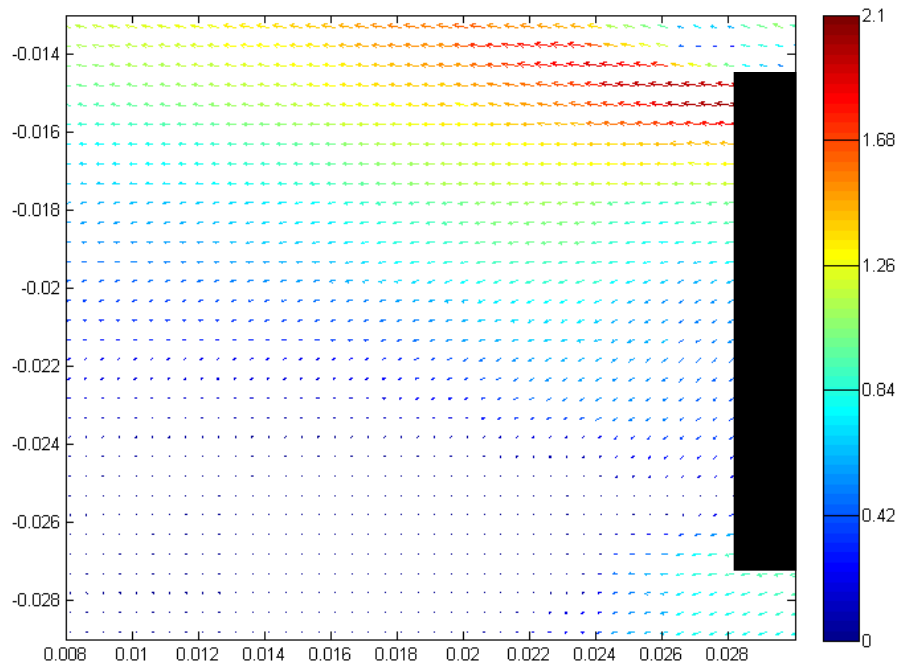
Figure 106: Face 2 top 0.2 kg/s CFD
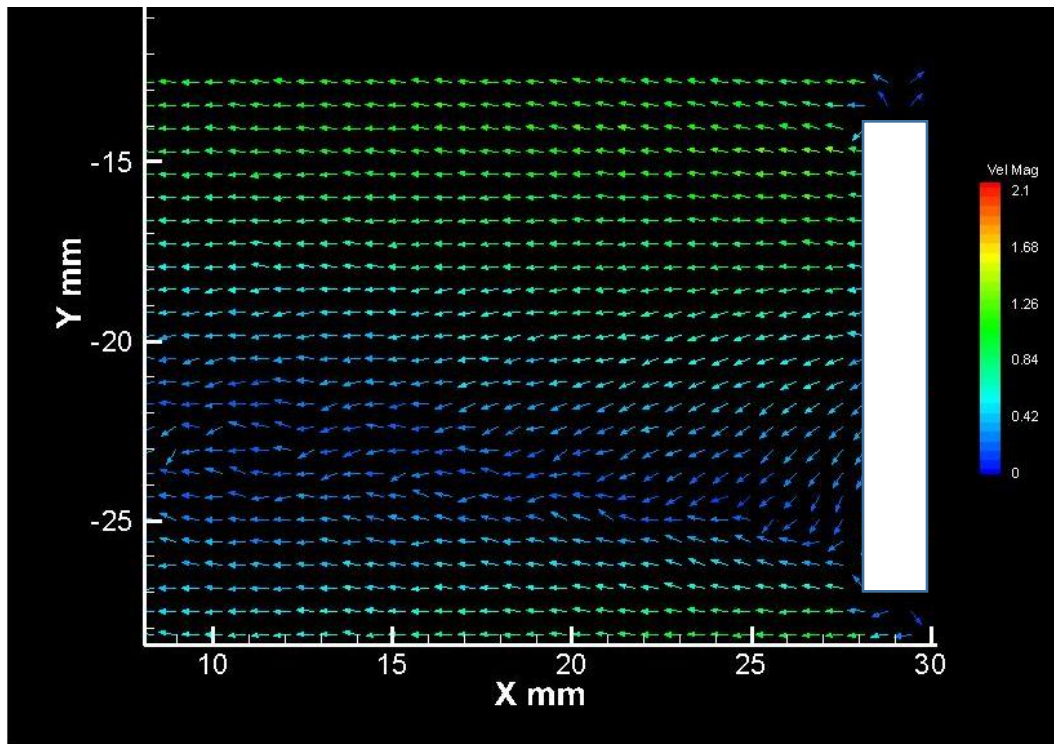
Figure 107: Face 2 top 0.2 kg/s PIV

Other changed planes results
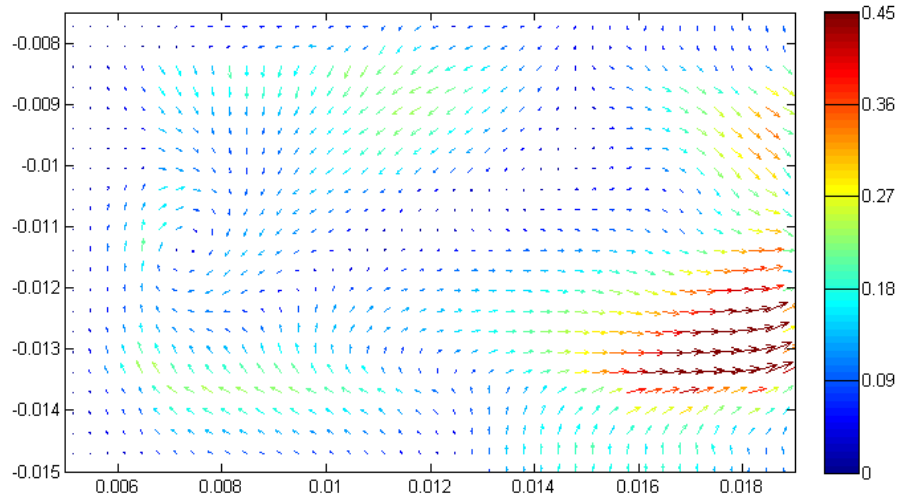
Figure 108: Face 1 direct -5° around X axis
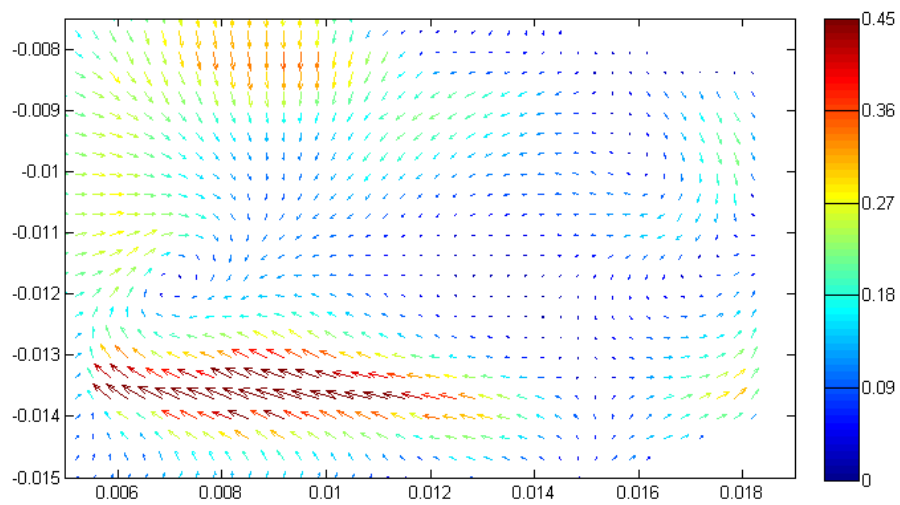
Figure 109: Face 1 direct -5° around Y axis
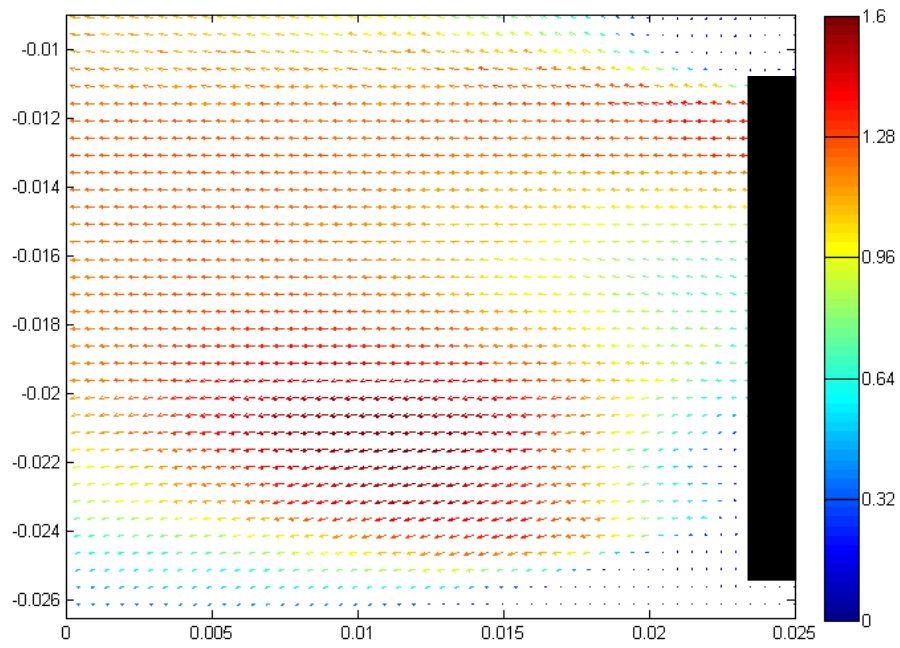
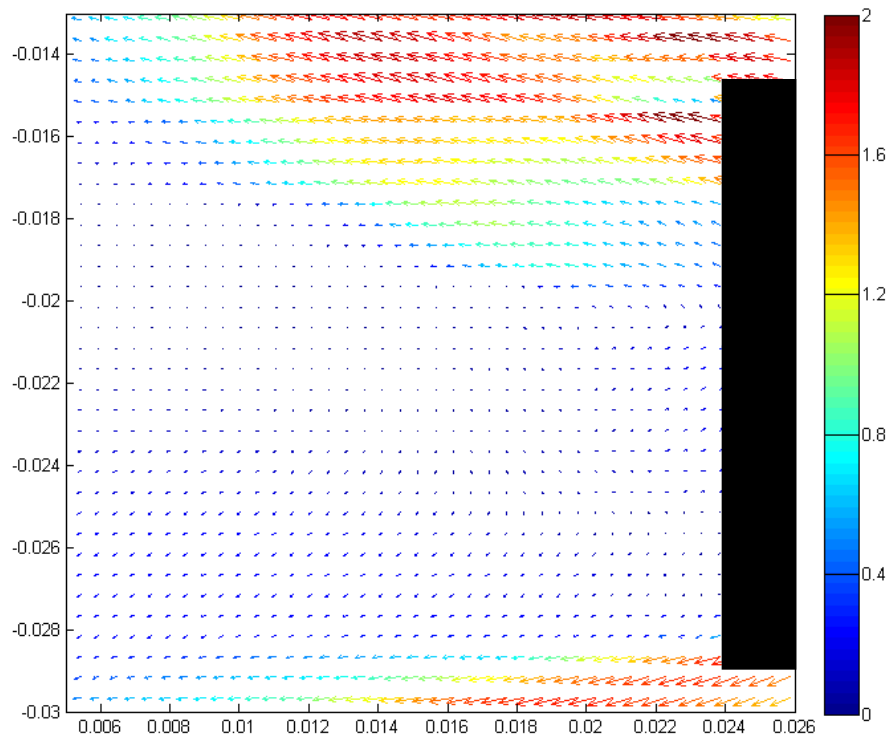**Figure 110: Face 1 horizontal -5° around x axis**
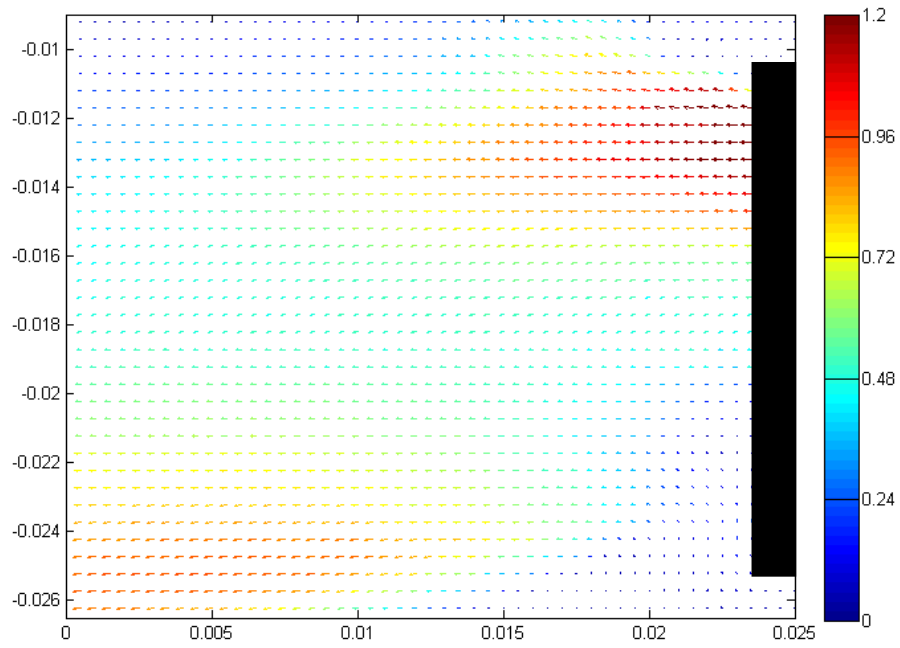
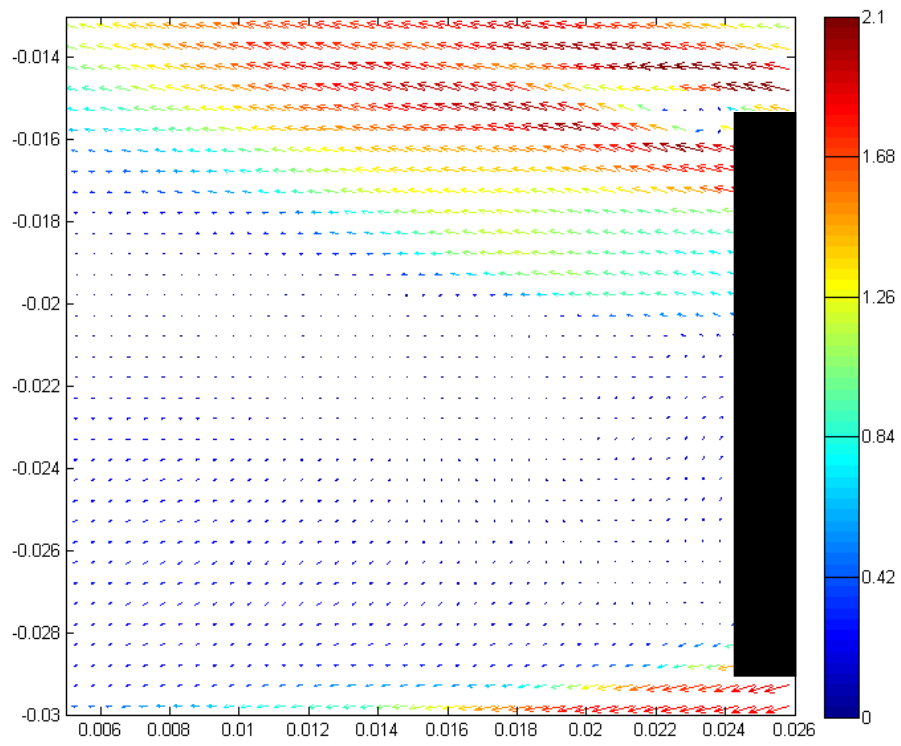**Figure 111: Face 1 horizontal -5° around x axis**
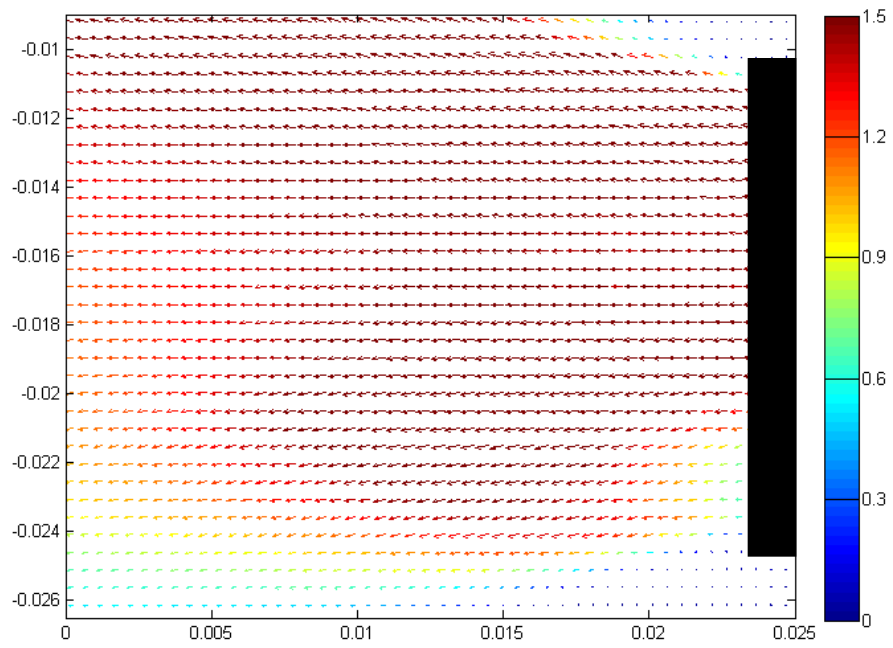
Figure 112: Face 1 horizontal 1mm down
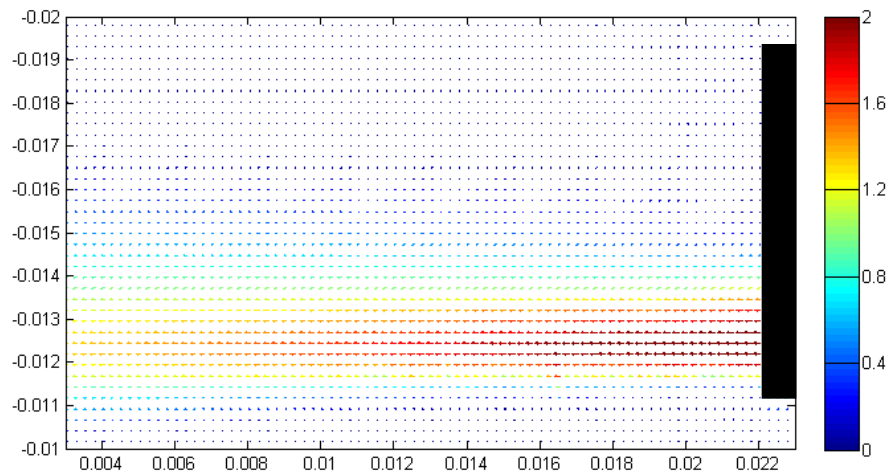
Figure 113: Face 1 mid -5° around X axis
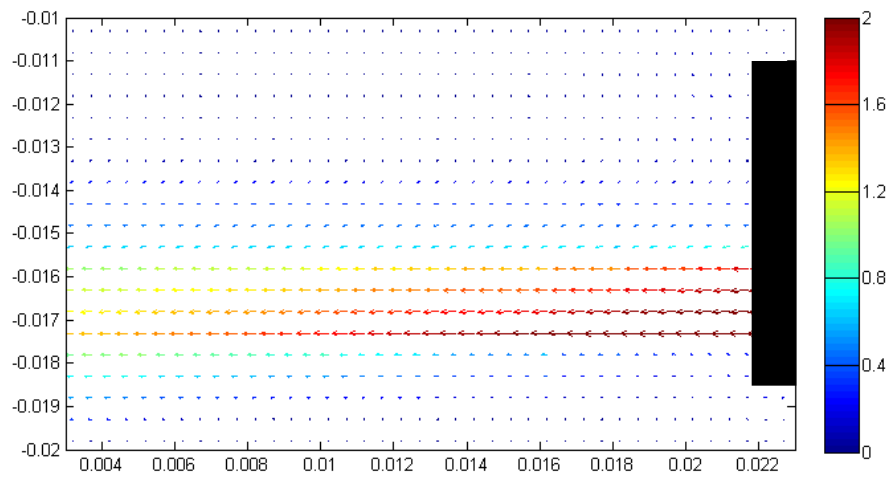
Figure 114: Face 1 mid -5° around Y axis
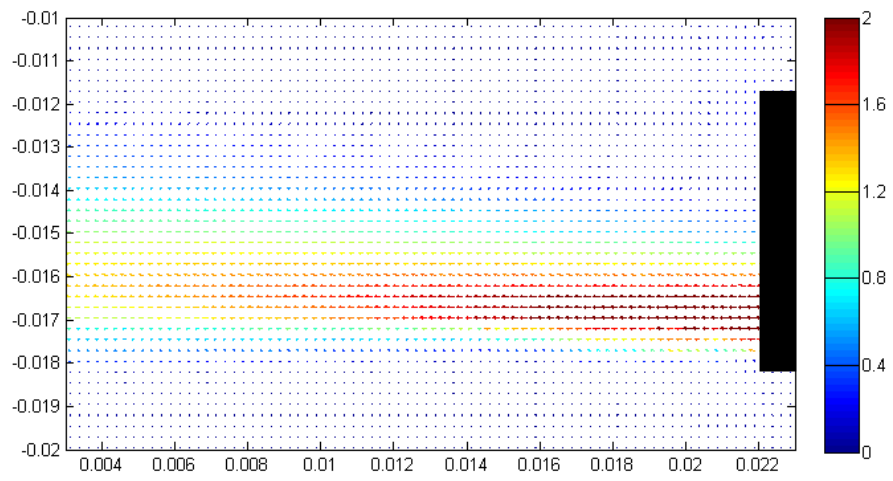
Figure 115: Face 1 1mm left
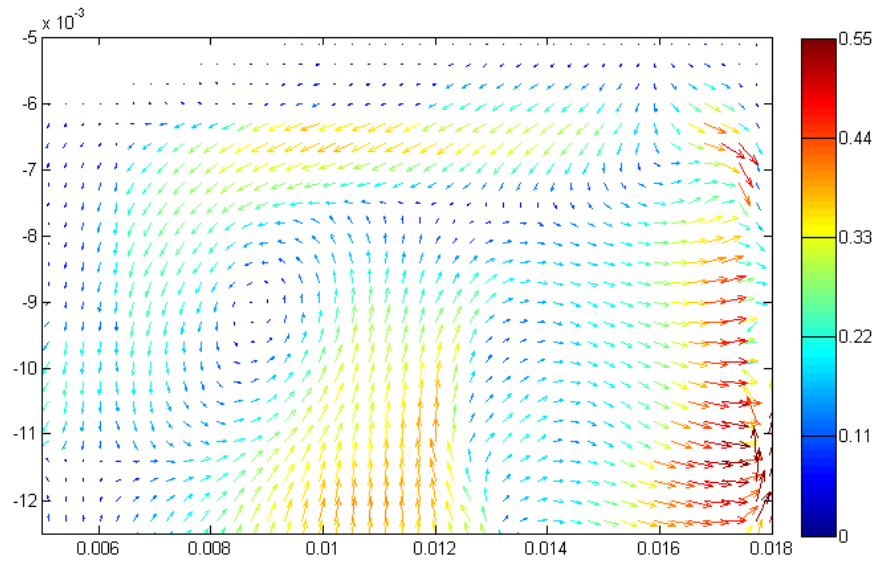
Figure 116: Face 2 direct -5° around X axis
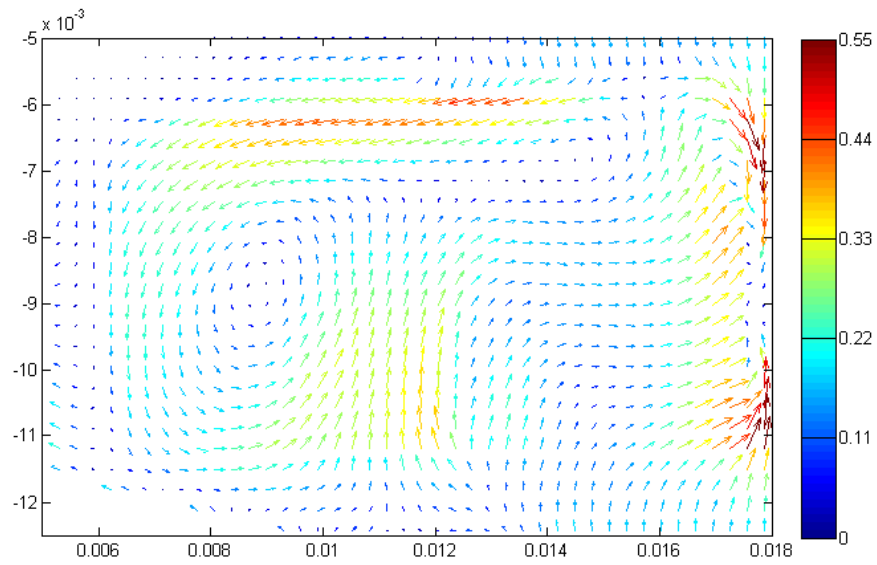
Figure 117: Face 2 direct -5° Y axis
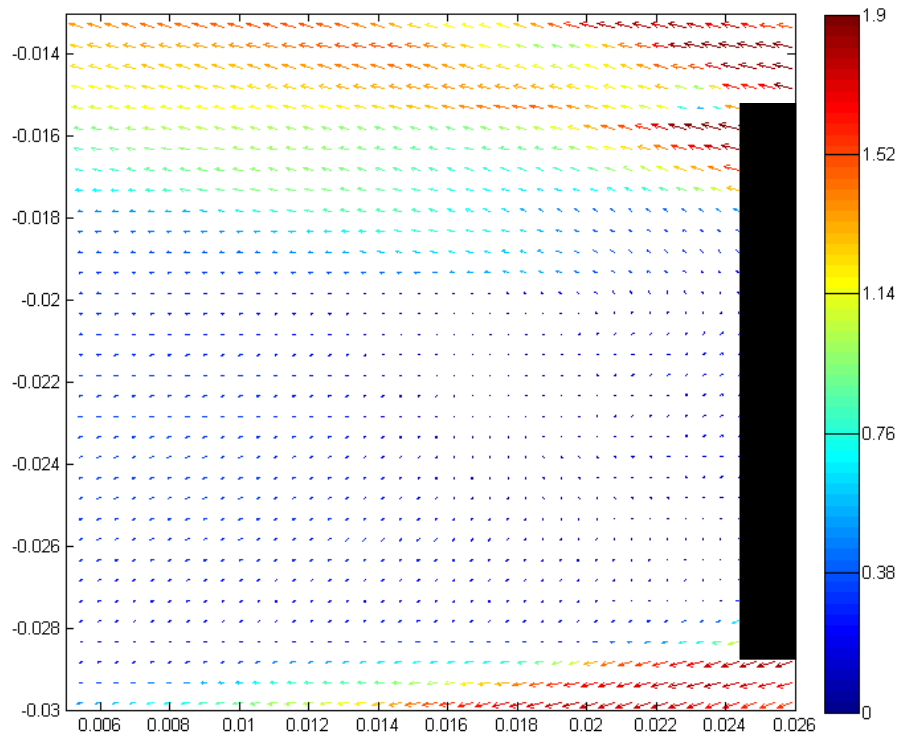
Figure 118: Face 2 horizontal -5° around X axis

Figure 119: Face 2 horizontal -5° around Y axis
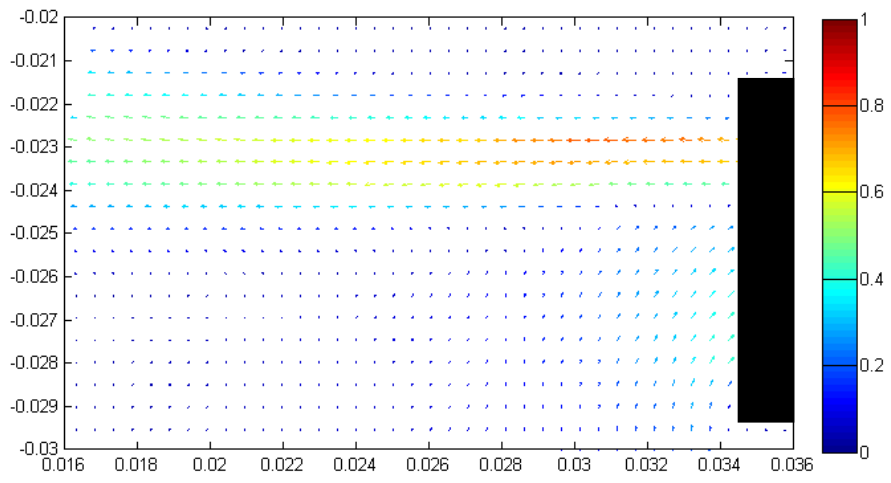
Figure 120: Face 2 horizontal 1mm down
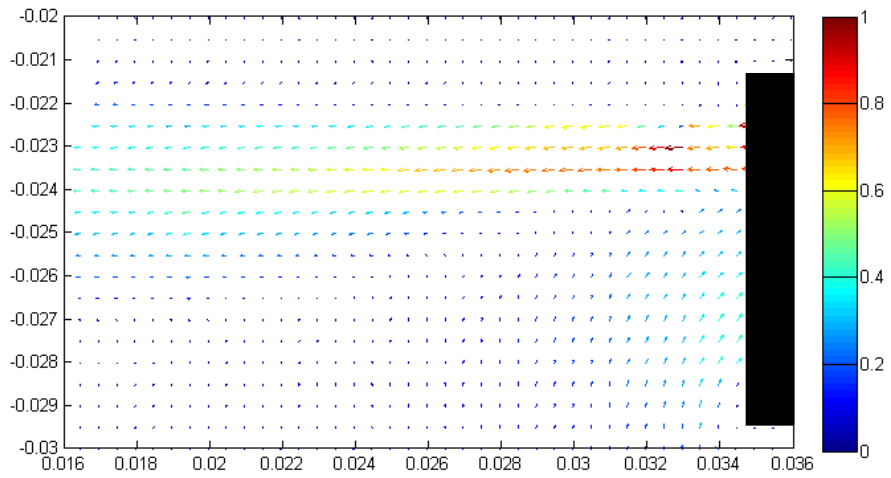
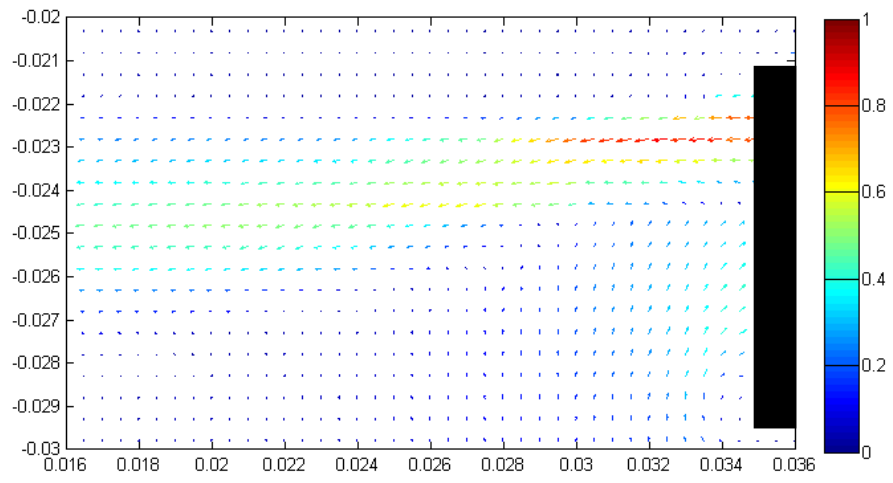**Figure 121: Face 2 mid -5° around X axis**

Figure 122: Face 2 mid -5° around Y axis

Figure 123: Face 2 middle 1mm left